

Characterization of the Solidification Behavior and Resultant Microstructures of Magnesium-Aluminum Alloys

By

Lee P. Barber

A Thesis

Submitted to the Faculty

Of

WORCESTER POLYTECHNIC INSTITUTE

In partial fulfillment of the requirements for the

Degree of Master

In

Materials Science and Engineering

By

December 6, 2004

APPROVED:

Makhlouf M. Makhlouf, Advisor, Professor of Mechanical Engineering

Richard D. Sisson Jr., Professor of Mechanical Engineering
Director of Manufacturing and Materials Engineering

ABSTRACT

Research and development of magnesium casting alloys depends largely on the metallurgist's understanding and ability to control the microstructure of the as-cast part. Currently few sources of magnesium solidification information and as-cast microstructures exist. Therefore, the goal of this research is to increase the general knowledge base of magnesium solidification behavior and to characterize the resultant microstructures. Equipment has been developed and constructed to study the solidification behavior of magnesium-aluminum casting alloys *via* non-equilibrium thermal analysis and continuous torque dendrite coherency measurements. These analyses have been performed on six magnesium-aluminum alloys, including industry dominant alloys such as AM60 and AZ91E, and experimental alloys which show commercial potential such as AXJ530. The resultant microstructures have been characterized for general microstructure trends and the various phases present were analyzed using optical and scanning electron microscopy, as well as energy dispersive x-ray spectroscopy.

The measurements were performed using a cooling rate on the order of 1-2°C/s, and results of these analyses show that in general, magnesium-aluminum casting alloys have relatively large solidification ranges, non-dendritic microstructures, and coherency points that are similar to those of aluminum casting alloys. These results should prove useful for research directed towards development of new magnesium alloys that are targeted for specific applications, as well as for optimizing casting procedures for Mg-Al alloys to obtain defect free cast structures.

Acknowledgements

First I would like to say thank you to my Advisor, Prof. Makhoul. You have been a friend, an unending resource, a source of motivation, and mentor. Without your help this would have never been possible.

I would also like to thank Yancy Riddle. You taught me everything I needed to know. I am grateful for your help, your guidance, and your patience.

To the distinguished members of my thesis committee, Prof. Apelian, Prof. Makhoul, and Prof. Sisson, I would like to thank each one of you for your time, your advice, and for the knowledge you instilled in me.

Viren Warke, Darrell Rondeau, Bob Taylor, Steve Derosier, and Matt Findon thanks for being great friends. Your help, support, and camaraderie were paramount in my growth as a person.

Lastly I thank my family. You have always been there to support me. I thank you for everything and I love you.

Table of Contents

ABSTRACT	2
Table of Contents	4
List of Figures	6
List of Tables	9
1.0 Introduction.....	10
2.0 Objective.....	13
3.0 Literature Review.....	14
3.1 Magnesium and Magnesium Alloys	14
3.1.1 Magnesium Alloys	14
3.1.2 Alloy Designation	15
3.1.3 Casting of Magnesium Alloys.....	16
3.1.4 Magnesium-Aluminum System.....	17
3.1.5 Solidification Behavior of Magnesium Alloys	18
3.2 Thermal Analysis Techniques.....	22
3.2.1 Differential Thermal Analysis and Differential Scanning Calorimetry.....	23
3.2.2 Thermogravimetric Analysis.....	24
3.2.3 The Cooling Curve Method	24
3.2.4 The Two-Thermocouple Method	26
3.2.5 Baseline for Thermal Analysis.....	28
3.3 Dendrite Coherency	30
3.3.1 Initial Work	32
3.3.2 Recent Work	34
4.0 Design of Experiments, Materials, and Procedures	40
4.1 Thermal Analysis	40
4.1.1 Design of Experiment	40
4.1.2 Procedure	43
4.2 Microstructure Characterization	44
4.2.1 Sample Preparation	44

4.2.2 Optical Microscopy.....	46
4.2.3 Scanning Electron Microscopy and Energy Dispersive Spectroscopy	47
4.3 Dendrite Coherency	48
4.3.1 Design of Experiment	49
4.3.2 Procedure	52
5.0 Results and Discussion.....	54
5.1 Compositional Analysis.....	54
5.2 Thermal Analysis Results	55
5.3 Microstructural and Phase Analysis Results.....	71
5.3.1 AM-type alloys.	71
5.3.2 AZ91E.....	80
5.3.3 AXJ530.	85
5.4 Dendrite Coherency Results.....	89
5.4.1 Dendrite Coherency Discussion.....	101
6.0 Conclusions	103
7.0 References.....	106

List of Figures

Figure 1 - Mg-Al Phase Diagram [10]	17
Figure 2 - Grain Refining Effects of Al in Pure Mg [12]	19
Figure 3 - Morphological Transition of Primary Mg [9]	21
Figure 4 - Possible Morphologies of Mg-Al Eutectic [15]	21
Figure 5 - Definition of Start of Solidification [18]	26
Figure 6 - Definition of End of Solidification [18]	26
Figure 7 - Thermal Analysis of AZ91E. Showing Importance of ΔT curve [2]	28
Figure 8 - Cooling Curve Including Curve Fit Baseline [22].	29
Figure 9 - Feeding During solidification of the Mushy Zone.	31
Figure 10 - Isothermal Shear Strength of Semi-solid Aluminum [26]	33
Figure 11 - Isothermal Shear Strength of Semi-solid Lead-Tin Alloy [26]	34
Figure 12 - Chai's Experimental Setup for Continuous Torque Measurement [24].	35
Figure 13 - Effect of Rotational Speed on Torque Measurements [25].	36
Figure 14 - Coherency Point Determined by Two-Thermocouple Technique [].	37
Figure 15 - Schematic of Direct Shear Cell [38].	38
Figure 16 - Effect of Morphology of Mushy Zone Behavior [36].	39
Figure 17 – Schematic of the Thermal Analysis and Data Collection System.	40
Figure 18 - Thermal Analysis System.	41
Figure 19 - Crucible and Thermocouple Placement.	42
Figure 20 - Interaction Volume of 15keV Electron Beam Interacting with Pure Mg	48
Figure 21 - Dendrite Coherency Apparatus.	50
Figure 22 - Vane positioned inside Crucible.	51
Figure 23 - Start of Solidification in AM60.	57
Figure 24 - Start of Eutectic Reaction in AM60.	58
Figure 25 - End of Solidification in AM60.	59
Figure 26 - Thermal Analysis Data for AM20.	60
Figure 27 - Plot of Temp vs. dT/dt Data for AM20.	60
Figure 28 - Thermal Analysis Data for AM40.	61
Figure 29 - Plot of Temp vs. dT/dt Data for AM40.	61
Figure 30 - Thermal Analysis Data for AM50.	62
Figure 31 - Plot of Temp vs. dT/dt Data for AM50.	62

Figure 32 - Thermal Analysis Data for AM60.....	63
Figure 33 - Plot of Temp vs. dT/dt Data for AM60.....	63
Figure 34 - Thermal Analysis Data for AXJ530.	64
Figure 35 - Plot of Temp vs. dT/dt Data for AXJ530.	64
Figure 36 - Thermal Analysis Data for AZ91E.....	65
Figure 37 - Plot of Temp vs. dT/dt Data for AZ91E.	65
Figure 38 - Temperature vs. Fraction Solid Data from PanDat for AM20.....	67
Figure 39 - Temperature vs. Fraction Solid Data from PanDat for AM40.....	68
Figure 40 - Temperature vs. Fraction Solid Data from PanDat for AM50.....	68
Figure 41 - Temperature vs. Fraction Solid Data from PanDat for AM60.....	69
Figure 42 - Temperature vs. Fraction Solid Data from PanDat for AXJ530.....	69
Figure 43 - Temperature vs. Fraction Solid Data from PanDat for AZ91E.	70
Figure 44 - Optical Micrograph of AM20. Etched for 2 sec with Acetic Glycol.	73
Figure 45 - Optical Micrograph of AM20, using Polarized Light. Etched for 2 sec with Acetic Glycol Etchant.	73
Figure 46 - SEM micrograph of AM20.....	74
Figure 47 - Optical Micrograph of AM40. Etch for 2sec in Acetic Glycol.	75
Figure 48 - SEM Image of AM40, Collected with Backscatter Electrons.	76
Figure 49 - SEM Images of AM60.	77
Figure 50 - High Magnification Optical Micrograph of AM60. Etched for 2sec in Acetic Glycol.	77
Figure 51 - Optical Micrograph of AM50, Using Polarized Light. Etched for 2sec in Acetic Glycol.	78
Figure 52 - Optical Micrograph of AM60, Using Polarized Light. Etched for 2sec in Acetic Glycol.	78
Figure 53 - EDS Line scan of AM50, Showing the extent of Al and Mn coring.	79
Figure 54 - EDS map of Al and Mn in AM60.	80
Figure 55 - Optical Image of AZ91E. Etched for 3sec in HF.	81
Figure 56 - SEM Image of AZ91E.	81
Figure 57 - SEM Image and EDS Map of Mg, Al, and Zn in AZ91E Eutectic.	82
Figure 58 - Optical Micrograph of AZ91E using Polarized light. Etched for 2sec in Acetic Glycol.	83
Figure 59 - EDS Spectrum of the Eutectic Phase in AZ91E.	84

Figure 60 - SEM Images of Secondary Phases in AZ91E.....	84
Figure 61 - EDS Spectrum of Secondary Phases in AZ91E.....	85
Figure 62 - Optical Micrograph of AXJ530. Etched for 3sec in Glycol Etchant.	86
Figure 63 - Optical Micrograph of AXJ530. Etched for 3sec in Glycol Etchant.	86
Figure 64 - Optical Image of AXJ530 using Polarized Light. Etched for 3sec with Glycol Etchant.	87
Figure 65 - SEM Image of AXJ50.....	88
Figure 66 - EDS map of Mg, Ca, Mn, and Al in AXJ530.....	89
Figure 67 - Determination of Coherency Point via Two Thermocouple Technique in AM60.	90
Figure 68 - Torque & dTor/dt vs. Time Data for AM20.....	92
Figure 69 - Torque vs. Fraction Solid Curve for AM20.	93
Figure 70 - Torque vs. Time Data for AM40.....	93
Figure 71 - Derivative of Torque vs. Time Data for AM40.	94
Figure 72 - Torque vs. Fraction Solid Data for AM40.....	94
Figure 73 - Torque vs. Time Data for AM50.....	95
Figure 74 - Derivative of Torque vs. Time Data for AM50.	95
Figure 75 - Torque vs. Fraction Solid Data for AM50.....	96
Figure 76 - Torque vs. Time Data for AM60.....	96
Figure 77 - Derivative of Torque Data for AM60.	97
Figure 78 - Torque vs. Fraction Solid Data for AM60.....	97
Figure 79 - Torque vs. Time Data for AXJ530.	98
Figure 80 - Derivative of Torque vs. Time Data for AXJ530.....	98
Figure 81 - Torque vs. Fraction Solid Data for AXJ530.....	99
Figure 82 - Torque vs. Time Data for AZ91E.	99
Figure 83 - Derivative of Torque vs. Time Data for AZ91E.....	100
Figure 84 - Torque vs. Fraction Solid Data for AZ91E.	100

List of Tables

Table 1 - Abbreviations for Alloy Designation.....	16
Table 2 - Etchants for use with Mg-Al alloys.....	46
Table 3 - Compositional Analysis of All Alloys.....	55
Table 4 - Averages Results from Thermal Analysis Experiments.	66
Table 5 - Solidification Simulation Results for AM-type Alloys.....	72
Table 6 - Coherency Results for Continuous Torque Measurements and.....	91

1.0 Introduction

The use of magnesium and magnesium alloys as a structural material is growing. This growth is being driven primarily by the automotive industry. Growth of magnesium use in the automotive industry has been estimated at 15% each year over the past decade. This growth is expected to continue at an annual rate of 12% over the next decade [1]. Demands for increased fuel efficiency in automobiles and cost effective manufacturing of parts have created this growth. Consumers' demands for increased luxury and safety features have caused an increase in vehicle weight translating into increased fuel consumption and ultimately increased CO₂ emissions. It is well known that CO₂ is a potent greenhouse gas. Magnesium has one major advantage over other structural materials, low density. With a density that is approximately two-thirds that of aluminum, the potential weight savings due to increased magnesium use has substantial environmental impact, including reduction of greenhouse gas emissions. Furthermore global environmental policy requires reusability and recyclability, and magnesium, unlike many polymers is a recyclable material.

Although magnesium alloys have been developed and used for the better part of the last century, research and development of magnesium alloys significantly declined after the 1960's as a result of an unfavorable price differential between magnesium and aluminum, and magnesium alloys were no longer needed to support war activities as a material in ballistic ordinance and aircraft. As a result, the metallurgical knowledge of magnesium and its alloys is immature compared to that of aluminum and its alloys leaving a significant amount of work waiting for the attention of researchers.

A gap between magnesium alloy research and industrial application exists, and is responsible in part for the arrest of magnesium alloy development. The nature of industrial research is to increase performance of existing materials and as such has focused mainly on property improvements of alloys through mechanical testing and subsequent compositional adjustments. However, a more metallurgically fundamental approach will make a large contribution towards magnesium alloy development. Fundamental knowledge of solidification characteristics and resultant microstructures provides a concrete base for alloy development and is natural precursor to mechanical property development. It is from the initial cast microstructure that all pursuant material properties must be developed. Controlling the as-solidified microstructure often affords the alloy designer the greatest influence over the final alloy performance and should be considered paramount to the intelligent, rapid design of improved alloys. Much of this knowledge is yet to be discovered and is well suited for academicians equipped with appropriate research equipment designed for studying microstructure and microstructure evolution [2].

A comprehensive reference on magnesium and its alloys is the recently released ASM's Magnesium and Magnesium Alloys handbook [3]. This reference covers fabrication, properties, and performance characteristics of existing magnesium alloys, but does not fully address fundamental metallurgical aspects of magnesium alloy solidification and microstructure development. Literature concerned with many magnesium alloy microstructures is either incomplete or totally lacking altogether. Even the alloys considered the workhorses of cast magnesium technology, e.g., AZ91, AM50, and AM60, are still to be fully understood. A comprehensive investigation into the

solidification and resultant microstructures of all magnesium casting alloys is required. The intention at the Advanced Casting Research Center (ACRC) is to create an authoritative encyclopedia tailored to the specific needs of the magnesium casting community. The purpose is to promote and facilitate sustainable research with magnesium alloys and to provide substantial input to the magnesium casting industry. Magnesium and its alloys can be divided into two major families of alloys. The magnesium-aluminum alloy family and the magnesium-zirconium-rare earth alloy family. The research presented in this thesis focus mainly on alloys that belong to the magnesium-aluminum family.

2.0 Objective

The goal of this thesis is to characterize the solidification behavior and resultant microstructures of magnesium-aluminum alloys using non-equilibrium thermal analysis and phase analysis techniques. The alloys analyzed include AM20, AM40, AM50, AM60, AZ91E, and AXJ530. The information generated will be incorporated into an authoritative book that will be published by the Advanced Casting Research Center. Specifically, the objectives of this thesis are:

1. Characterize the solidification behavior of selected magnesium alloys using thermal analysis techniques and establish for each alloy
 - (i) Solidification Time
 - (ii) Solidification Range
 - (iii) Precipitation Events
 - (iv) Fraction Solid Content
2. Characterize the resultant as-cast microstructure using optical and scanning electron microscopy and establish
 - (i) Grain Size
 - (ii) Phase Present
 - (iii) Phase Morphology
 - (iv) Phase Composition
 - (v) Inhomogeneities Due to Solidification
3. Characterize the dendrite coherency point using continuous torque measurements.

3.0 Literature Review

3.1 Magnesium and Magnesium Alloys

Magnesium is the lightest metal that can be used for structural applications [3]. The element was first discovered in 1808 by Sir Humphrey Davey. Comprising 2.7% of the earth's crust and 0.13% of the earth's ocean water, this makes Magnesium a relatively plentiful element [4]. Magnesium has been used for many different applications throughout history including pyrotechnics, chemicals, as well as a structural material.

Magnesium has one major advantage over all other structural materials, low density. The automotive industry has become highly interested in the use of magnesium and its alloys primarily for reducing curb weight of vehicles, which in turn will help improve the environmental impact of automobiles by increasing their fuel efficiency and reducing their harmful emissions [5].

3.1.1 Magnesium Alloys

Like most other metals, magnesium is rarely used in its pure form. Alloying is used to improve virtually all properties of magnesium for both wrought and cast products. Magnesium has a hexagonal lattice structure and has an atomic diameter that allows for solid solubility with a wide range of elements. Apart from cadmium, most binary alloys including magnesium form eutectic or peritectic systems [3]. The principal goal of alloying is to make specific improvements to the alloys properties. The most common alloying elements are aluminum, zinc, manganese, zirconium, silver, yttrium and rare

earth elements. Copper, nickel, and iron are considered harmful impurities that need to be controlled properly to insure the quality of magnesium alloys [3,6].

Aluminum is the most common alloying element in Mg alloys. Aluminum additions increase the hardness, strength, and freezing range of the alloy, but reduce the ductility. Manganese is used primarily to enhance corrosion resistance. Zinc has many effects on magnesium alloys. It can help in room temperature strength, corrosion resistance, and in precipitation hardenability in some alloys [3,6]. Zirconium is used in magnesium alloys for grain refinement; it is currently the only known element that has potent grain refining effects on Mg; however, zirconium cannot be used in alloys containing Al or Mn, as it forms stable compounds [3,7]. Silver additions are used to improve the age hardening of magnesium alloys, but the use of silver has been limited due to the high costs. Yttrium is used to impart high temperature creep resistance to Mg. Rare earth additions include cerium, lanthanum, neodymium, gadolinium, and praseodymium. They all have been found to increase high temperature strength, creep resistance, and to reduce casting porosity [3].

3.1.2 Alloy Designation

Although no international system exists for magnesium alloy designation, a naming method has been created and adopted by the American Society for Testing and Materials. The method includes two letters followed by two numbers. The two letters are the letter abbreviations given to the two largest alloying elements, and the numbers are the weight percent of these alloying elements rounded to the nearest whole number. A fifth digit is sometimes given and is used to distinguish between alloys that have the

same two principal alloying elements with the same concentration. Table 1 lists the one-letter abbreviations for the most commonly used alloying elements [3,4,6].

Table 1 - Abbreviations for Alloy Designation.

Letter	Alloying Element
A	Aluminum
C	Copper
E	Rare Earth Metals
H	Thorium
J	Strontium
K	Zirconium
L	Lithium
M	Manganese
Q	Silver
S	Silicon
W	Yttrium
X	Calcium
Z	Zinc

3.1.3 Casting of Magnesium Alloys

Although magnesium can be fabricated by virtually all manufacturing techniques [3], this research focuses on casting and the alloys specifically designed for casting. Magnesium casting processes may be divided into three groups, sand casting, permanent mold casting, and high-pressure die-casting. Selection of casting processes is determined by the size, required tolerance, and production quantity; similar to other commonly cast materials. High-pressure die-casting is currently the most commonly used method for magnesium alloys.

Since casting is a net shape or near-net shape forming process, work-hardening is not applicable in order to improve the properties of magnesium casting alloys. Therefore, other techniques, such as solid-solution strengthening, precipitation hardening, grain

refinement, and specially designed heat treatments are used in order to enhance the properties of magnesium alloy castings [8].

3.1.4 Magnesium-Aluminum System

The Mg-Al binary system is origin of some of the oldest and most commonly used casting alloys. Alloys such as AZ91, AM50, and AM60 still comprise a large portion of all magnesium alloy casting [9]. Figure 1 shows the Mg-Al phase diagram [10]. The maximum solubility of Al in Mg ranges from about 2.1wt% at 25°C to 12.6wt% at the eutectic temperature of 437°C. The eutectic composition is 32.3wt% and the eutectic is between α -Mg and the β -phase, which is $Mg_{17}Al_{12}$ [11].

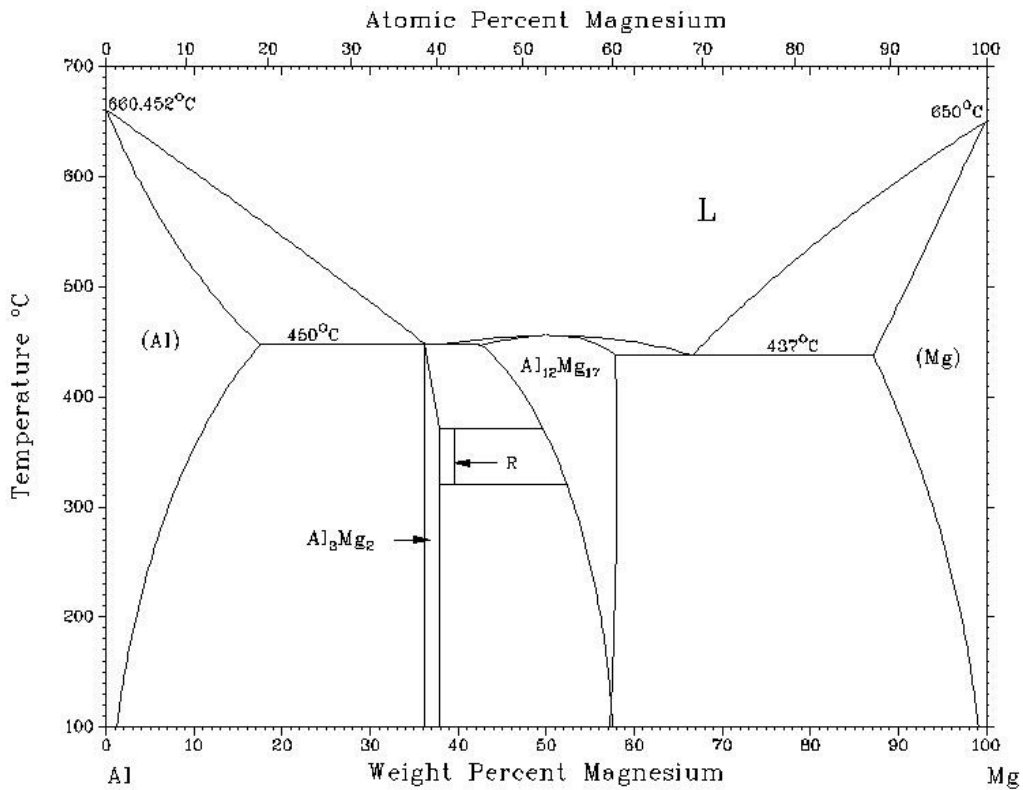


Figure 1 - Mg-Al Phase Diagram [10]

As expected from the phase diagram, Mg-Al alloys are precipitation heat treatable, although solutionizing and aging of Mg-Al alloys do not have the effectiveness seen in many Al-Si alloys as the β - $\text{Mg}_{17}\text{Al}_{12}$ precipitate forms in an incoherent manner [4,11].

Mg-Al binary alloys are generally highly castable and typically have good mechanical properties. However, commercial alloys are rarely binary alloys; they are mostly ternary and quaternary alloys with additions of zinc, manganese, rare earth metals, and silicon. These additions improve specific properties as was discussed earlier and make the alloys more suitable for casting; however, they also complicate the solidification behavior of the alloy [3,9].

3.1.5 Solidification Behavior of Magnesium Alloys

The final microstructure of Mg-Al alloys will be dependent on the nucleation and growth characteristics, of both the primary grains and the eutectic [7]. Therefore, alloying elements, grain refiners, and cooling rate during solidification will all have a major effect on the final microstructure and properties of the cast alloy. Nucleation is typically controlled by the use of grain refiners. Grain refinement in magnesium casting alloys is not as well understood as in aluminum casting alloys [12,13]. The growth morphologies of both the primary dendrites and the eutectic in the Mg-Al system are highly dependant on the aluminum content and cooling rate [14].

A reliable grain refiner for the Mg-Al system is lacking. Zirconium has been found to be a satisfactory grain refiner for some magnesium alloys, but Zr is not used in

the aluminum containing alloys. Nevertheless, most Mg-Al alloys are used for high-pressure die-casting, and this process has very high cooling rates, which introduces a high driving force for nucleation. This causes increased nucleation and therefore creates a large number of primary grains thus reducing the need for a potent grain refiner. Alloys based on the Mg-Zn and the Mg-RE (rare earth addition) have been found to form very fine grains when Zr is added. The mechanism of Zr grain refinement is poorly understood, but is believed to be caused by the crystal structure and lattice parameter similarity of Mg and Zr [12].

Recent research has been done in order to determine a better method of grain refining aluminum based magnesium alloys. Work by Lee et al [12,13] has shown the effects of aluminum and strontium (Sr) additions on grain size of magnesium alloys. It was found that grain size decreases dramatically when increasing the Al content of the alloy from 0wt% to 5wt%, but further additions have no effect. Figure 2 shows the grain refining effects of Al in pure Mg.

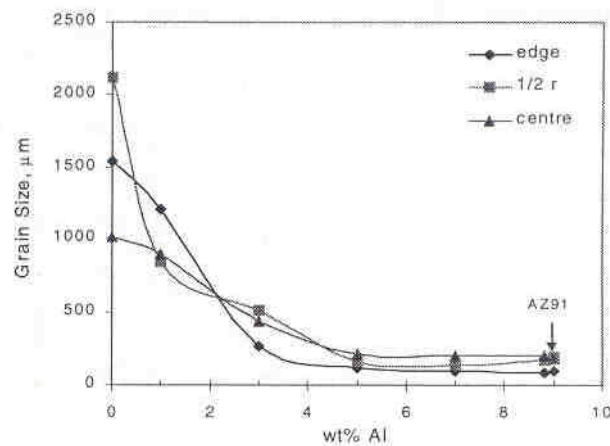


Figure 2 - Grain Refining Effects of Al in Pure Mg [12]

Lee et al [12,13] also investigated the effects of Sr addition on Mg-Al alloys for both Mg-3wt%Al and Mg-9wt%Al alloys. The results show that a 0.01-0.1wt%Sr addition has a very strong grain refining effect on the 3wt%Al alloys as it decreases the average grain size by about 100 μm . The results for the 9wt%Al alloy show a narrower range of grain refining effect and in most cases no difference was observed.

Primary grain morphology and eutectic formation have been found to be highly related [14]. The size and shape of the primary phase affects the size of the eutectic pockets that form upon solidification, and this will change the morphology of the eutectic, which has been found to have four different morphological transitions depending on the alloy composition and cooling rate.

Changes in microstructure of the primary phase can be attributed to both increasing the Al content and increasing the cooling rate. The microstructure of α -Mg with 1wt% Al addition is globular and with increasing the Al content to 9wt% the globular structure goes through a transition to a highly dendritic structure [9,14]. The critical concentration for the transition from globular to dendritic is in the range of 4 to 7wt% Al, depending on the cooling rate. Figure 3 shows this transition; notice the six-fold symmetry of the dendrites. The effects of cooling rate on the primary phase are similar in nature, although they cause the morphological transition to occur at lower Al concentrations [14].

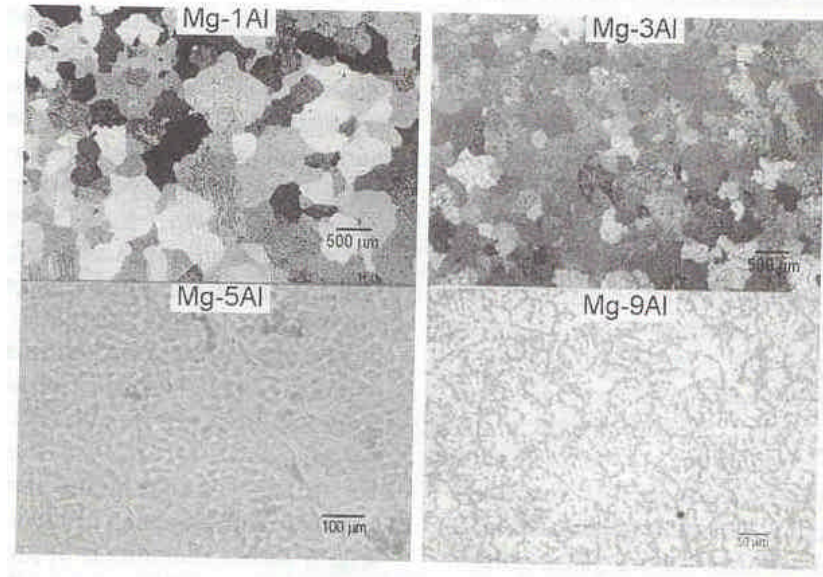


Figure 3 - Morphological Transition of Primary Mg [9]

The eutectic in the Mg-Al system is β -Mg₁₇Al₁₂. This eutectic forms in virtually all Mg-Al alloys with as little as 2wt% Al. Although in most commercial alloys the eutectic is a fully or partially divorced eutectic, it has been found to form lamellar, fibrous, and granular morphologies as well. Figure 4 shows the different morphologies of the β -Mg₁₇Al₁₂ eutectic [15].

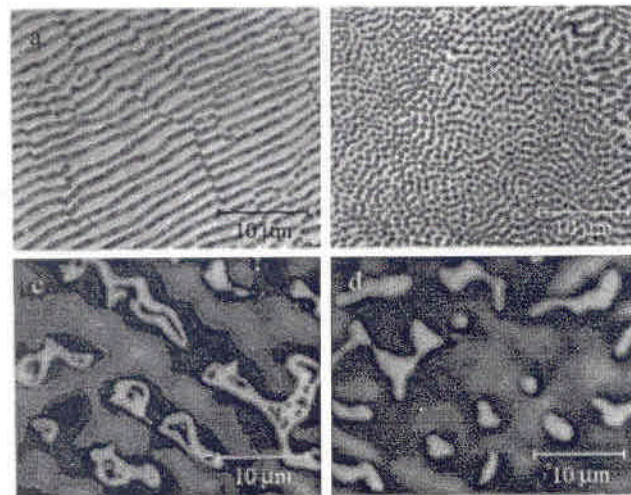


Figure 4 - Possible Morphologies of Mg-Al Eutectic [15]

The lamellar and fibrous eutectic morphologies form in alloys with more than 12wt% Al. Therefore these morphologies are not likely to form in commercial alloys.

The eutectic structure has been related to the primary phase morphology. The dendritic and highly dendritic structures are accompanied by the partially and fully divorced eutectic, while the globular and rosette-like primary grains are accompanied by granular eutectic [14]. This can be attributed to the size and shape of the eutectic pockets formed. A dendritic structure creates smaller pockets of entrapped liquid with high local Al concentration. Globular structures inherently leave large eutectic channels. Smaller pockets of entrapped liquid require lower undercooling for eutectic nucleation and growth, therefore divorced eutectics are favored and commonly found in Mg-Al alloys [7].

3.2 Thermal Analysis Techniques

There are many techniques available for investigating the solidification of metals and alloys. There are standardized techniques such as differential thermal analysis (DTA), differential scanning calorimetry (DSC), and thermogravimetric analysis (TGA). These techniques, although well documented and very accurate, prove to be inadequate for investigating solidification of metal alloys. The solidification of commercial alloys is complex and under normal conditions, does not occur under equilibrium conditions. The techniques mentioned were designed for determining equilibrium properties. These techniques also require the use of extremely small samples. For accurate characterization of the solidification of metal alloys, a much larger sample size is necessary for several reasons. Enough material must be sampled in order to: (1) accurately measure the alloy

composition by spark transmission spectrometry, (2) perform both optical and scanning electron microscopy, and (3) ensure solidification occur over a wide enough time scale that can be accurately measured [2]. Therefore non-equilibrium thermal analysis techniques must be employed. Several non-equilibrium techniques exist for investigating solidification of metals and alloys. These techniques are the cooling curve method and the two-thermocouple method [21]. Both these techniques are based on understanding and interpreting the temperature versus time data collected during the solidification of the alloy.

3.2.1 Differential Thermal Analysis and Differential Scanning Calorimetry

The differential thermal analyzer (DTA) is a device, which is designed to measure the difference in temperature between two samples which are subject to the same heating/cooling regimen [16]. One of the two samples is a reference sample, commonly an inert material over the range of temperature being investigated. The sample material and reference materials are not required to have any similarities, although it can be advantageous to select reference materials with thermal similarities, such as thermal conductivity and heat capacity. The differential scanning calorimeter (DSC) is a device based on many of the principles of the DTA [16,17]. The difference between the DTA and DSC is that the DSC measures the heat input or heat removal required to keep the sample and reference at the same temperature. These devices are well documented and used throughout the world for calculating material properties such as latent heat and specific heat.

Both the DTA and DSC techniques require the use of very small samples. The sample size is on the order of one milligram to one gram [17]. This small sample size allows for the approximation of a uniform temperature over the entire sample, and for very rapid heating and cooling, which is required for accurate DSC work. This small sample size is also the primary reason why these techniques cannot be applied to solidification of metal alloys. Solidification thermal analysis focuses on the nucleation and growth of crystals and grains. A sample size of this magnitude does not allow for an appropriate number of grains for investigation [18].

3.2.2 Thermogravimetric Analysis

Thermogravimetric Analysis (TGA) is a method by which the weight of a sample is measured during a heating/cooling regimen. The device is a highly sensitive balance placed inside a furnace. The primary use of the TGA is for investigating gaseous releases during transformations [16]. This technique is commonly used in parallel with calorimetry measurements. The reference state for TGA is typically an open system [17]. Since the primary goal of investigations into solidification of metals and alloys is usually precipitation events, both beginning and ending, TGA does not have any advantages for this work.

3.2.3 The Cooling Curve Method

The cooling curve method is the most widely used method for investigating solidification of metals and alloys. The application and setup is the most simplistic and therefore can be widely used by both academic and industry researchers. The setup

involves placing a thermocouple in the melt and allowing the melt to solidify while temperature is recorded as a function of time [18]. The cooling rate can be controlled in a variety of ways, such as furnace cooling, forced cooling via gas or water, or natural room temperature air cooling. The ability to control the cooling rate allows different casting techniques to be simulated with ease.

The foremost use of cooling curves has been the determination of arrest points during solidification. Arrest points on cooling curves are related to the precipitation events, as the latent heat of formation is released the cooling is arrested temporally. This method was introduced in 1954 with the work of Morrogn-Williams [19] and Hultgren et al. [20] on cast irons.

A 1969 paper by L. Bäckerud and B. Chalmers, introduced a technique that improves the understanding of the cooling curve method through the use of the time dependant derivative of the cooling curve [21]. The derivative of the cooling curve improves the sensitivity of the measurements and allows for better precision in determining the exact points of primary and eutectic solidification events. The starting point of the reaction occurs at the time when the derivative curve first varies [18,22]. Figure 5 shows the definition of the start of solidification.

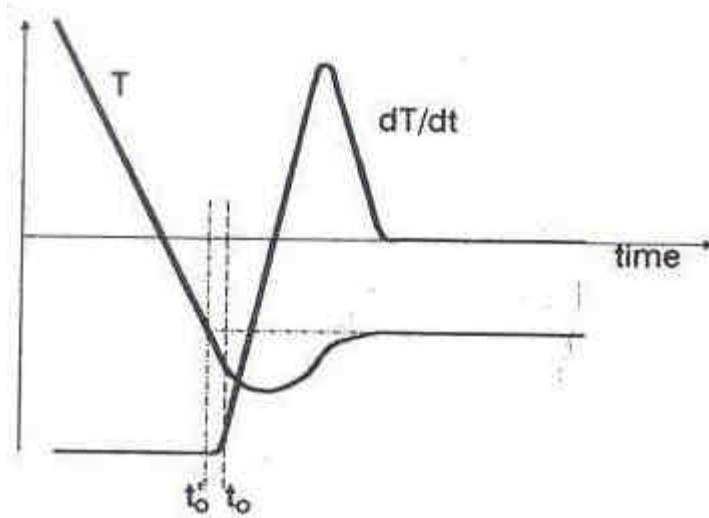


Figure 5 - Definition of Start of Solidification [18]

The end of solidifications is defined by the extension of the final derivative after it has stabilized. Figure 6 shows the method of determining the end of solidification.

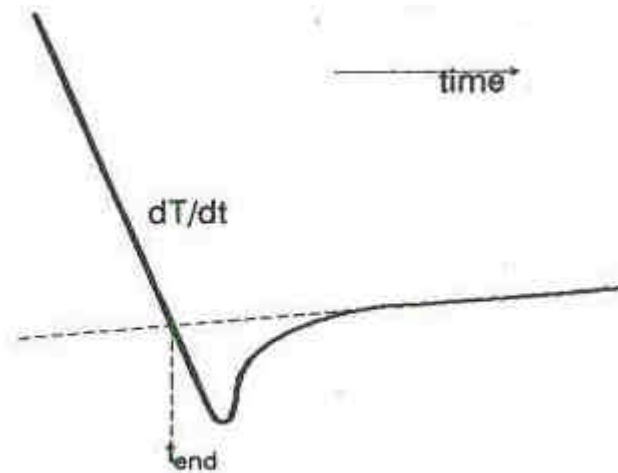


Figure 6 - Definition of End of Solidification [18]

3.2.4 The Two-Thermocouple Method

The two-thermocouple technique was first used by Bäckerud and Chalmers [21] and further developed and used by Bäckerud et al. in their work on aluminum alloys

[22,23]. This method uses two thermocouples placed at different locations in the melt. The cooling curves can be analyzed in a similar manner as described earlier. The two-thermocouple method also introduces another method of analyzing the solidification curve; this is through the use of the ΔT vs. time curve. Where ΔT is the difference between the two thermocouples. The thermocouples are placed in precise locations, one at the center of the crucible and the other inside the side wall of the crucible. ΔT is defined as:

$$\Delta T = T_E - T_C \quad (3-1)$$

The use of the ΔT curve allows identification of minor precipitation events that evolve only a small amount of latent heat and are therefore otherwise difficult to see on the derivative curve.

The advantage of the two-thermocouple method can be seen in this example, which is adapted from work by Y. Riddle [2].

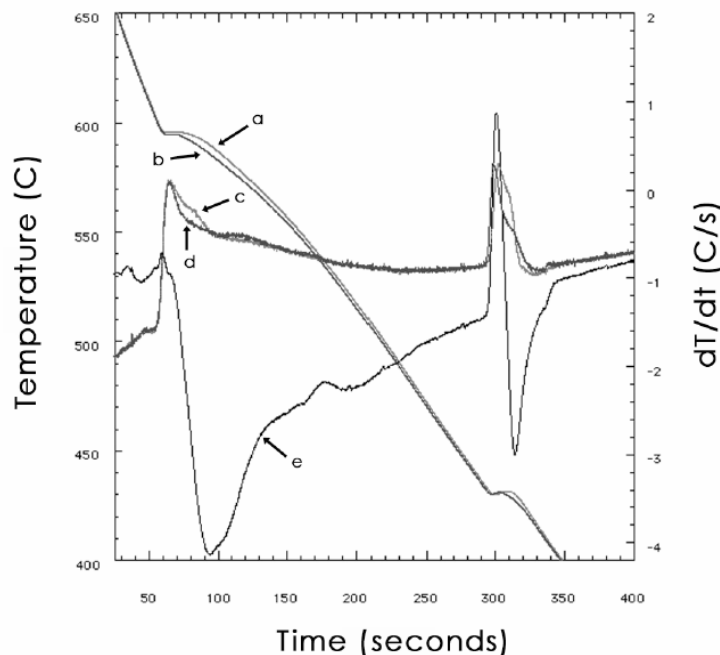


Figure 7 - Thermal Analysis of AZ91E. Showing Importance of ΔT curve [2]

The curves in Figure 7 are: (a) T_c (i.e., temperature of the center thermocouple), (b) T_w (i.e., temperature of the wall thermocouple), (c) dT_c/dt , (d) dT_w/dt , and (e) ΔT . There is a visible change in the ΔT curve between 150 and 200 seconds. The other curves show no significant change over this time range. This change corresponds with the precipitation of an Al-Mn phase. Reactions similar in nature to this reaction are precisely the reason for the use of the two-thermocouple method.

3.2.5 Baseline for Thermal Analysis

All thermal analysis techniques have one thing in common. They all are measures from a standard or reference state. Similar to the DTA and DSC techniques where there is a reference material, all thermal analysis techniques use a comparison method of some sort. The reference state or point of comparison is commonly called the baseline for

thermal analysis. In many types of thermal analysis the baseline is related to heat capacity effects during a transformation. In order to accurately measure thermal properties using thermal analysis techniques these effects of heat capacity or the baseline must be removed from the calculation [16,17].

Bäckerud and Tamminen developed a technique for determining fraction solid versus temperature data during solidification [18,22]. This technique requires the definition of a reference state or a baseline. As discussed previously, the baseline will contain only the thermal effects of changing from the initial temperature to the final temperature. Therefore the variation from this baseline can be used to determine the effects of the transformation, or fraction solid data.

Their technique involves curve fitting the cooling rate of the liquid phase with the cooling rate of the solid phase. This gives a baseline cooling rate applicable throughout the two phase region. This curve fit baseline is shown in the Figure 8.

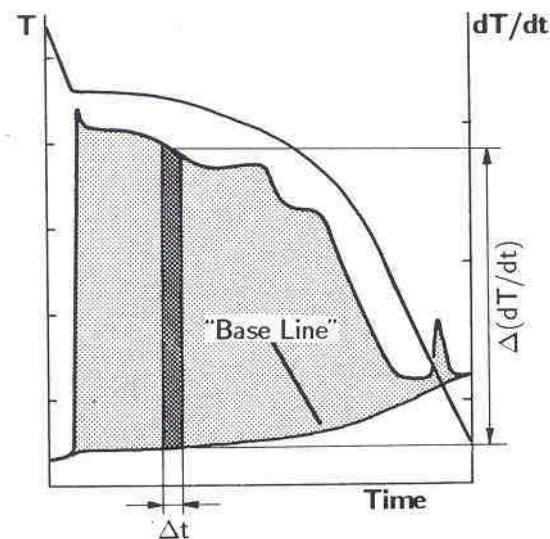


Figure 8 - Cooling Curve Including Curve Fit Baseline [22].

Using this baseline, equation 3.2 can be applied in an incremental fashion to determine fraction solid as a function of time.

$$f_s = \frac{1}{\Delta H} \sum_{t=0}^t \left(C_p \Delta \left(\frac{dT(t)}{dt} \right) \right) \quad (3.2)$$

In their calculations, Bäckerud and Tamminen used the values of latent heat and heat capacity for a simple Al-Si binary. The error involved with the assumption of a pure Al-Si binary has not been evaluated.

3.3 Dendrite Coherency

Dendrite coherency is defined by Arnberg, Bäckerud, and Chai as the point where dendrites begin to impinge upon one another causing the formation of a continuous solid network through the sample. At this point there is a sudden increase in strength of the material, and therefore in the force required to shear the materials [24]. After this point is reached, the strength of the material continues to increase until the material has fully transformed from liquid to solid.

Solidification of metal alloys commonly begins with the formation of the primary phase. This primary phase can take on several different morphologies, although the dendritic and globular morphologies are the most common ones. When the first fraction solid of the primary phase forms, dendrites nucleate and grow. The dendrites are initially separate and can move freely in the melt, this is shown in Figure 9a. Movement of the solid particles at this stage is termed mass feeding [25].

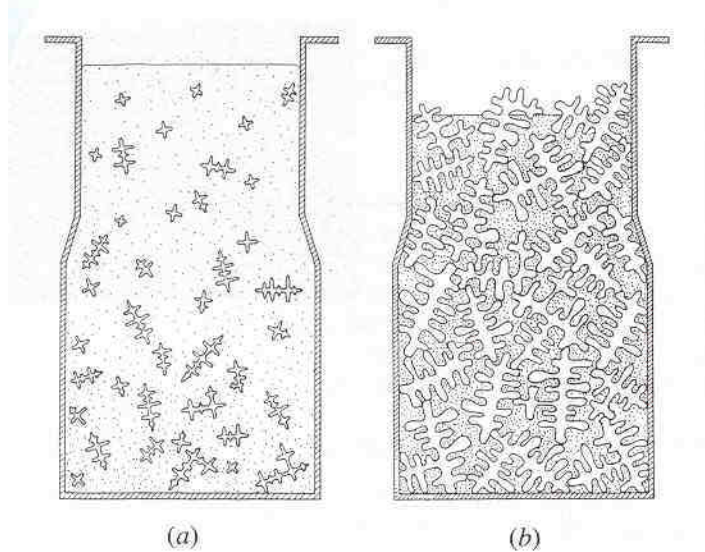


**Figure 9 - Feeding During solidification of the Mushy Zone.
 (a) Mass Feeding and (b) Interdendritic Feeding [26].**

When the dendrites begin to impinge upon one another forming a solid network, the coherency point is reached. At the coherency point, a transition in the behavior of the metal occurs. The metal begins to develop properties such as shear strength and the thermal conductivity of the metal begins to change. The feeding properties of the melt also change. Once a solid network has formed, feeding can only proceed within the interdendritic region. The solid network and interdendritic region is shown by the gray areas in Figure 9b. As solidification progresses the feeding of the melt is restricted, the coherency point is first transition in the feeding behavior. Therefore understanding of the coherency behavior and the coherency point will help determine proper casting conditions, in order to produce defect free casting [25].

3.3.1 Initial Work

The earliest work on the change of properties of alloys in the semi-solid state was performed by Verö in 1935 [27]. His work included tensile and bend tests of materials that were heated to temperatures near their solidus temperature and into the semi-solid regime. His two main findings were that strength decreases as the material's temperature approaches the solidus temperature, and that strength decreases to zero as the material's temperature approaches the liquidus temperature. Work that is similar in nature to Verö's work was performed by Singer and Cottrell [28]. They found that Al-Si alloys retained little strength at the midpoint temperature between their liquidus and solidus temperatures.

The concept of investigating the deformation behavior and shear strength of semi-solid materials was developed by Metz and Flemings [29,30]. They isothermally sheared blocks of Al-4%Si and Al-4%Cu alloys and found that below a fraction solid of 0.2, the alloys exhibited virtually no strength. Once the fraction solid was above 0.2, strength developed exponentially with increasing fraction solid. They also found that shear strength increased with increasing strain rate and with increasing grain size. Grain refined alloys did not develop strength until a fraction solid of 0.4 was reached. Figure 10 shows the results of Metz and Flemings experiments as well as a schematic of the sample geometry [26].

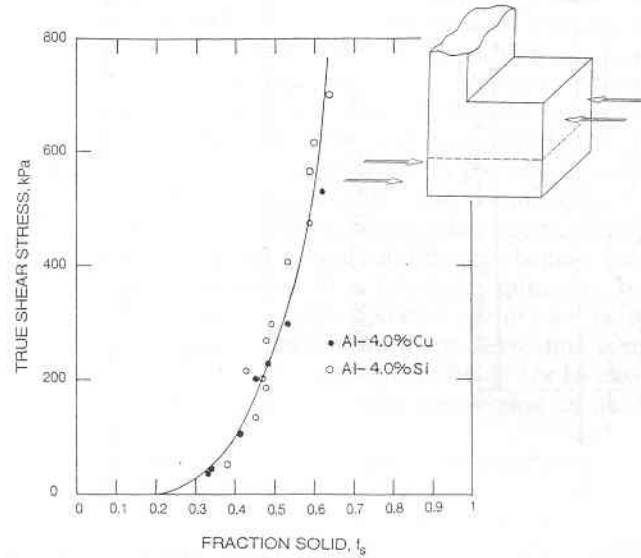


Figure 10 - Isothermal Shear Strength of Semi-solid Aluminum [26].

Following the work of Metz and Flemings was Spencer et al. [31] who developed a method for shearing the semi-solid metal. Their method involved two concentric grooved cylinders, between which was located a semi-solid lead-tin alloy. One of the cylinders was coupled to a viscometer and rotated, thus shearing the alloy. The results of their experiments, shown in Figure 11, were very similar to those of Metz and Flemings. Spencer et al. [31] found that in their Sn-15%Pb alloy strength developed at a fraction solid of 0.15. Spencer was also the first to relate shifts in the coherency point to the morphology of the dendrites. He found that extensive shearing caused the dendrites to transform to globules. The coherency point of the globular alloys was shifted from a fraction solid 0.15 to a fraction solid of 0.4.

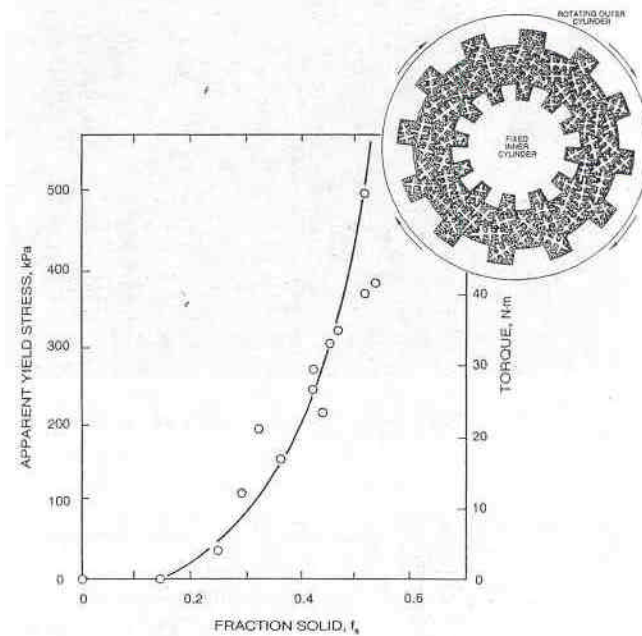


Figure 11 - Isothermal Shear Strength of Semi-solid Lead-Tin Alloy [26].

Claxton was the first to use continuous torque measurements during the solidification of a melt to characterize the melt's solidification characteristics [32]. Claxton rotated a graphite disk in a slowly solidifying melt, generating torque-temperature curves for wrought Al alloys. His experiments determined the force needed to break the dendrites, not specifically the dendrite coherency point. Claxton's work helped develop the current rheological technique used by Arnberg, Bäckerud, and Chai [24,25].

3.3.2 Recent Work

Within the past ten years, much research has been performed in the field of dendrite coherency and the development of strength during solidification. The concept of a rigidity point or maximum packing factor has been developed. The rigidity point is

defined as the point where interdendritic feeding becomes restricted [24]. Three methods of evaluating the coherency point and/or rigidity point have been developed, namely, (1) the continuous torque measurement technique, (2) the thermal analysis temperature difference method, and (3) the direct shear cell method.

The most widely used technique for determining the dendrite coherency point of alloys is the continuous torque measurement method. This method was developed and extensively used by Arnberg, Bäckerud, and Chai [24,25] and involves rotating a vane or blade in the solidifying melt. The vane is connected to a rheometer and the torque resisting rotation is measured as a function of time and temperature. The measurement apparatus developed by Chai is shown in Figure 12 [25].

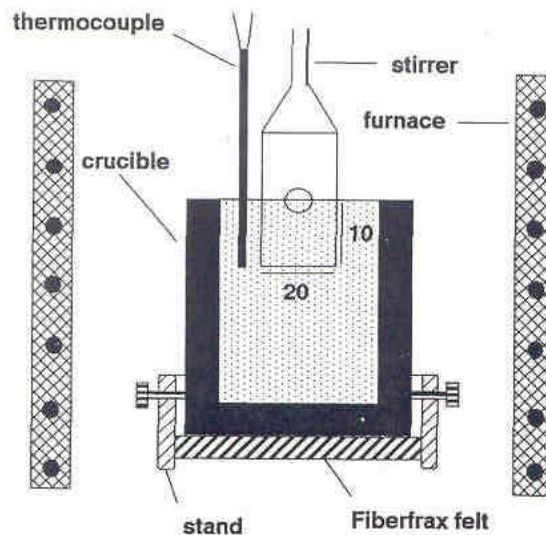


Figure 12 - Chai's Experimental Setup for Continuous Torque Measurement [24].

Chai investigated the effect of rotational speed on the coherency point and found that although the coherency point did not change with the experimental parameters, the rigidity point did. Since a slower rotational speed would have the least effect on structure

formation, the rotational speed of 0.05rpm was used. Figure 15 shows the effects of rotational speed on the torque vs. fraction solid data [25].

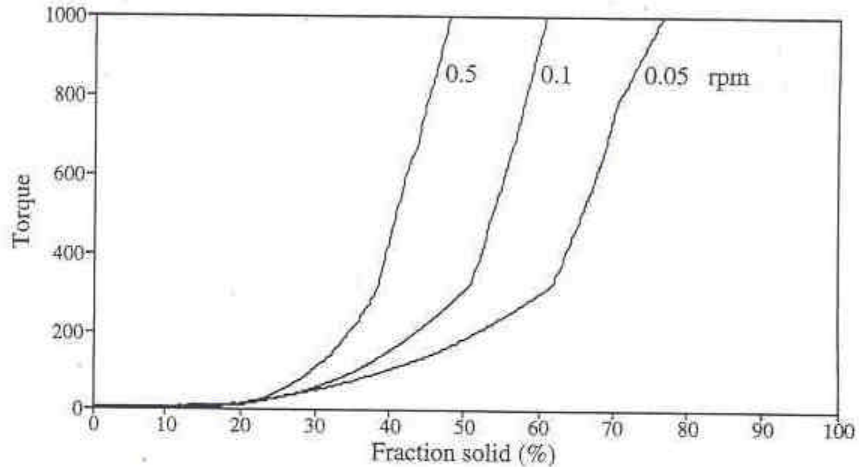


Figure 13 - Effect of Rotational Speed on Torque Measurements [25].

The technique Chai used for locating the coherency and rigidity points was to take the derivative of the torque vs. fraction solid curve. The two distinct break points on this curve are defined as the coherency point and the rigidity points. The rigidity point has been found to be dependant of the experimental method used as can be seen in Figure 13. Chai concluded that composition, cooling rate, grain refining, and eutectic modification all affect the coherency point of an alloy. Veldman et al [33] measured the coherency points of Al-Si-Cu alloys containing different primary phase morphologies. Their results were given in terms of coherency fraction solid (f_s) and spherical grains showed a coherency point at f_s of 0.48, rosette-like grains showed a coherency point at f_s of 0.35, and dendrites showed a coherency point at f_s between 0.15-0.2.

The thermal analysis method of determining the dendrite coherency point was first introduced by Chai [25]. This method requires the use of the two-thermocouple

technique developed and used by L. Bäckerud [21,22,23]. The temperature difference between the two thermocouples, $\Delta T = T_e - T_c$, rises due to release of latent heat at the wall first. As nucleation and growth of the solid phase continues towards the center of the crucible, latent heat is released at the center. This movement of the latent heat release causes the temperature difference curve to decrease. This continues until the dendrites have become coherent. Once a coherent network of solid has formed, the thermal conductivity of the system increases causing the temperature difference to stabilize [25]. The coherency point as determined by this method is shown in Figure 16.

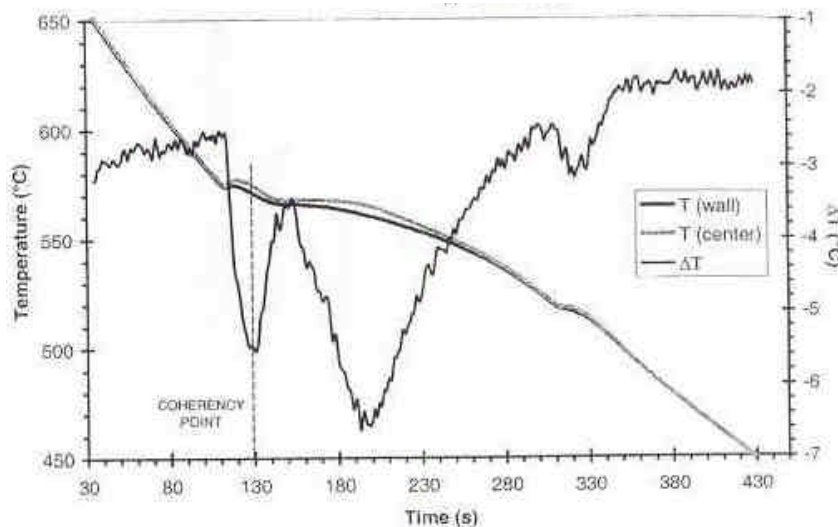


Figure 14 - Coherency Point Determined by Two-Thermocouple Technique [33].

Chai states that this technique is accurate for all grain refined Al alloys and for non-grain refined Al alloys containing total solute concentrations higher than 5wt%. Since most commercially used alloys fit this criterion, this technique could potentially be an easy method for determining coherency point. However, a recent paper by Veldman

[33] shows that the thermal analysis technique produces results that differ from those produced by the other methods of determining coherency point.

The direct shear cell technique was developed by Nabulsi et al [34] and involves a shear cell which shears a sample of semi-solid material that is maintained at an isothermal condition. A thermocouple placed at the shear plane measures the sample's temperature during the experiment. Nabulsi et al used this technique to compare coarse dendritic structures to small rosette-like structures. This technique, although it takes a comparatively long time to perform, seems to be very accurate in measuring the dendrite coherency point.

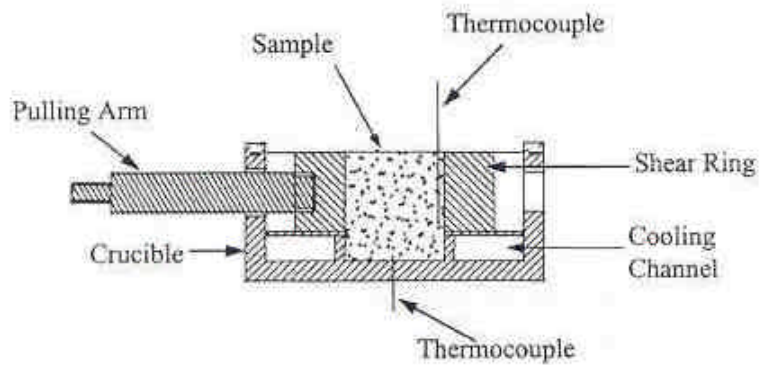


Figure 15 - Schematic of Direct Shear Cell [38].

Several researchers have used the direct shear cell technique [35,36,37], and several interesting findings have been made. For example, the rigidity point found in some measurement made with the continuous torque method has been confirmed using the direct shear cell technique [35]. Also, the effect of the morphology of the primary phase on dendrite coherency was further investigated, and it was found that the smaller globular structures reach coherency and rigidity at a higher fraction solid than the larger

ones. Figure 16 shows the strength of an alloy in the semi-solid range as a function of fraction solid and morphology [34,36]. Tensile strength of a material doesn't develop until the rigidity point has been reached [37].

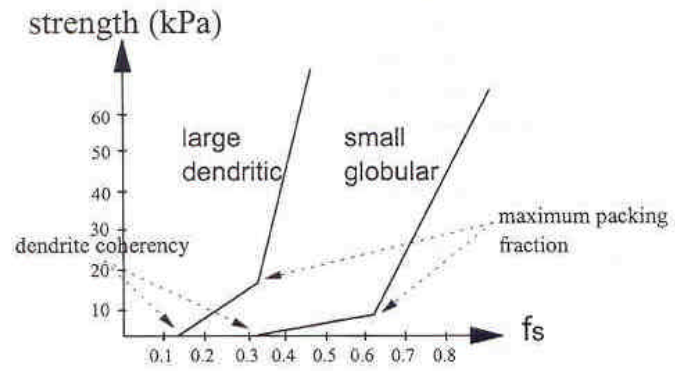


Figure 16 - Effect of Morphology of Mushy Zone Behavior [36].

4.0 Design of Experiments, Materials, and Procedures

4.1 Thermal Analysis

After a thorough evaluation of the available thermal analysis techniques for investigating the solidification behavior of metal alloys, the two-thermocouple cooling curve method developed by Bäckerud et al [22,23] appears to be the most robust and technically advanced method. Therefore this method was selected for this research.

4.1.1 Design of Experiment

A customized thermal analysis unit was fabricated based on the two-thermocouple thermal analysis technique. The system was designed specifically for use with magnesium and magnesium alloys. Figure 17 is a schematic representation of the system.

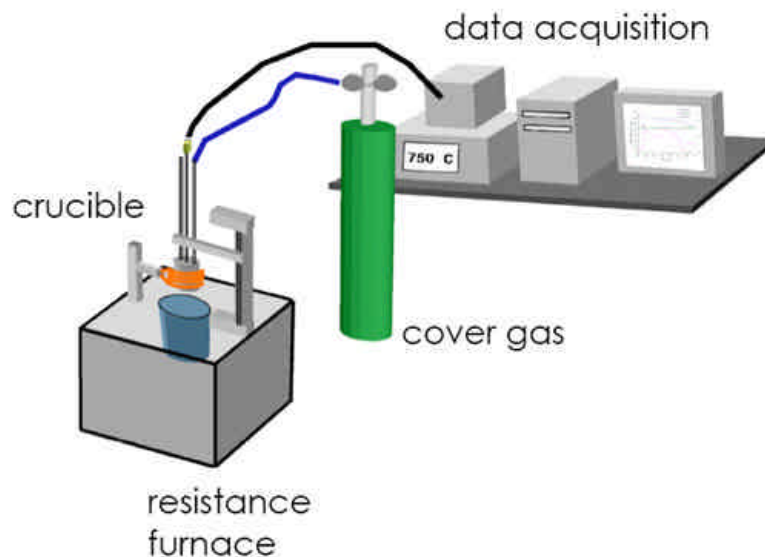


Figure 17 – Schematic of the Thermal Analysis and Data Collection System.

This apparatus allows the users to melt approximately 70-100 grams of Mg under a cover gas. The cover gas used is 50% CO₂ + 0.2% SF₆ + 49.8% air. A cover gas is required to eliminate the reaction of Mg with the moisture in the air, causing a fire. A mild, low alloy steel crucible is used for melting the alloys as recommended by the ASM handbook [3], the crucible is coated with boron nitride to reduce the diffusion of iron from the crucible into the Mg alloy. Once loaded with the Mg alloy sample, the crucible is attached to the vertical loading arm and lowered into the furnace. This attachment point is also the top of the enclosed cover gas environment. Figure 18 show the crucible/furnace loading mechanism. Notice that the gas inlet and outlet tubes serve as structural members.

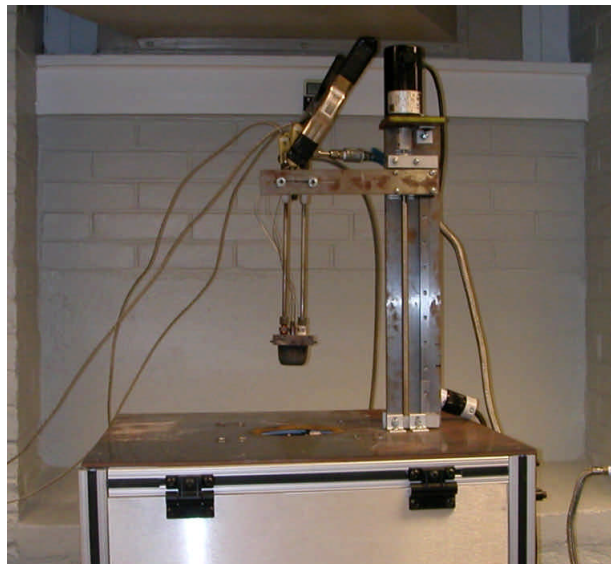


Figure 18 - Thermal Analysis System.

Industrial grade Mg alloys were used in all measurements. Compositional analysis was performed on each ingot to ensure that the ingots had a composition within

the specified limits of the alloy. Cylindrical samples were machined from the ingots to be approximately 44mm in diameter and 32mm in height. Two 3mm holes were drilled in each sample to accommodate the thermocouples. The thermocouples used are 1/32 inch diameter K-type shielded and grounded thermocouples in order to minimize noise. They were calibrated prior to use by a five point calibration system. The calibration points were freezing and boiling water, pure tin, pure zinc, and pure aluminum. Calibration was performed in order ensure that each thermocouple used was properly calibrated to the same scale by identical methods. The thermocouples used had a limit of error of +/- 0.2°C. The thermocouples are positioned at the center of the sample (T_c) and 8mm from the crucible's edge (T_e). The thermocouple positioning system is built into the cover of the crucible. Figure 19 shows the crucible containing a sample with the two thermocouples.

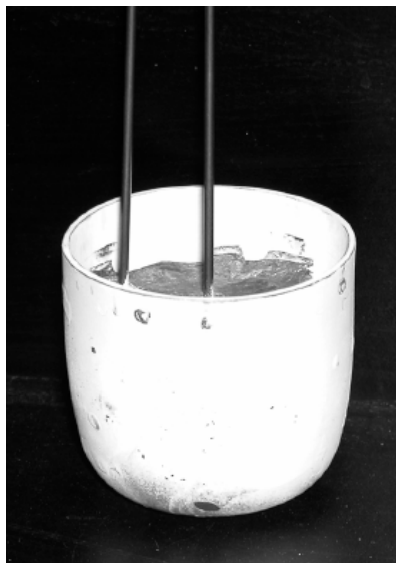


Figure 19 - Crucible and Thermocouple Placement.

A data collection unit^I connected to a computer, running monitors and records the temperatures measured by the thermocouples. Temperature is collected at 60 kHz in order to reduce noise. The data acquisition system reported averaged data to a file every 0.1sec. No two consecutive temperature data points varied by more than 0.1°C. Reduction of noise during data collection is critical to produce noise-free derivatives of the data [2].

The thermal analysis apparatus was tested using an AA356.2 aluminum casting alloy and comparing the results with established data [23].

4.1.2 Procedure

Prior to experimentation, each ingot from which the Mg alloy samples were prepared was measured for composition. Compositional analysis measurements were made using a spark transmission spectrometer^{II}. An average of ten measurements and the standard deviation was recorded [38].

The experiment begins with loading the Mg alloy sample into the boron nitride coated crucible. The thermocouples are introduced into the sample sheathed with a stainless steel thermocouple sleeve coated with boron nitride; this allows for easy removal of the thermocouple after the melt has solidified. Thermocouples are located at the midpoint of the vertical axis of the cylinder by eye, as the radial direction is fixed by the apparatus. The crucible is then loaded into the vertical loading arm as shown in

I. National Instruments Corporation, SCXI Data Collection Unit and DasyLab Software, 11500 N. Mopac Expwy, Austin, TX 78759-3504.

II. Spectro Analytical Instruments, Spectromax Spark Spectrometer LMXM3, Boschstr. 10, 47533 Kleve, Germany.

Figure 18. Once the crucible is loaded, the cover gas system is tested prior to melting in order to ensure that the cover gas is flowing into the crucible over the melt surface.

The furnace is preheated to 750°C and then the data collection system is started and configured to record the data to a text file. The sample is then lowered into the furnace using the linear actuator. The furnace opening is then covered with insulating material to retain heat. When the sample's temperature reaches 450°C, the cover gas is required for melt protection. The pressure release gauge on the cover gas cylinder is always set to 2psi to ensure consistent cooling conditions for all measurements. The sample is equilibrated to a temperature of approximately 700°C. Once the sample has reached temperature, the crucible is removed from the furnace using the linear actuator and allowed to cool in room temperature air with the cover gas flowing until the temperature has dropped below 450°C. Temperature data is collected throughout solidification.

Once the sample has completely solidified, the procedure is repeated twice making a total of three measurements per sample. Three samples were prepared for each alloy making a total of nine measurements per alloy. After the measurements were completed, compositional analysis was again performed using spark emission spectroscopy for each sample.

4.2 Microstructure Characterization

4.2.1 Sample Preparation

Sample preparation and metallography of Mg and Mg alloys can be a daunting task. Achieving quality metallographic results with Mg alloys is not trivial. Most

problems in preparation of Mg alloys are due to the soft nature of the Mg matrix and the substantially harder intermetallic phases. Magnesium alloys also readily react with water, thus restricting the use of many polishing media and suspensions. This leads to difficulty in eliminating scratches, controlling relief between phases, and creates potential for matrix deformation [39]. Each alloy must be treaded differently and the procedure presented here is an overview of the practices that worked best for Mg-Al alloys.

The samples were first cut on an abrasive cut-off wheel, and then mounted in bakelite. Grinding was performed using silicon carbide (SiC) grinding papers up to 4000 grit. Tap water was used since it does not seem to have any bearing on the final polish. Samples were rinsed thoroughly before moving to a smaller grit SiC. Commercial dishwashing soap was used to dress the higher grit SiC papers when smearing occurred. Prior to polishing, the sample was rinsed with ethanol and cleaned for several minutes using an ultra-sonic cleaner.

Samples were hand polished with a suspension of 1 μ m alumina in a solution of ethanol and ethylene glycol. It was found that a ratio of 1:1 for the ethanol-ethylene glycol solution worked best. Water of any purity was found to etch the surface. The polishing cloths used for this suspension were either Struers OP-NAP or OP-CHEM, depending on the alloy, at a speed of 120rpm. Higher speeds tend to cause excessive pullout of the intermetallic phases resulting in scratches that can only be removed by the more abrasive grinding wheels. The samples were polished until scratches appear as uniform as possible. The samples were then thoroughly cleaned in ethanol and placed in an ultra-sonic cleaner for several minutes. For some alloys particularly those with larger fraction of intermetallic phases, an additional step was needed. The samples were dipped

into a concentrated nitric acid solution for 1-3 seconds. Then the polishing procedure was repeated with the 1 μm size alumina suspension. After ultra-sonic cleaning, a final polish was performed with a 0.05 μm alumina suspended in a solution of ethanol and ethylene glycol in a 1:1 ratio on a Struers OP-CHEM cloth at a speed of 120rpm.

Several etchants were used to help in the microstructure characterization. Table 2 shows some of the etchants used.

Table 2 - Etchants for use with Mg-Al alloys

Name	Composition	Comment
Glycol	1ml HNO ₃ 24ml Distilled Water 75ml Ethylene Glycol	General Purpose Immerse 3-5sec.
Acetic Glycol	20ml Acetic Acid 1ml HNO ₃ 60ml Ethylene Glycol 20ml Distilled Water	General Purpose Immerse 1-3sec.
Hydrofluoric	5ml Hydrofluoric Acid 95ml Distilled Water	Immerse 1-2sec. Darkens Mg ₁₇ Al ₁₂
Acetic-Picric	5ml Acetic Acid 6 g Picric Acid 10ml Distilled Water 100ml Ethanol	Immerse until brown film forms. Rinse. Reveals Grain Boundaries
Picric	5 g Picric Acid 50ml Distilled Water 50 ml Ethanol	Immerse 3-5sec.

4.2.2 Optical Microscopy

A Nikon Epiphot inverted metallograph was used for all optical microscopy. The metallograph was fitted with a Nikon Coolpix 5000 digital camera. All micrographs were taken in full color. Polarized light was used in cases where it was advantageous. These color digital micrographs portray a more accurate representation of the true

microstructure. Even without polarized light microstructural features of Mg alloys, such as different phases, develop specific colorations when etched properly [38].

4.2.3 Scanning Electron Microscopy and Energy Dispersive Spectroscopy

A JEOL 840 scanning electron microscope (SEM) equipped with a KeveX energy dispersive spectroscope (EDS) operating at an accelerating voltage of 15keV using a LaB₆ electron source was used for all SEM and EDS work. Most SEM images were taken using secondary electrons (SE) although some images have been acquired from backscatter electrons (BSE). Images were taken in the magnification range of 150-550X.

The working distance for all EDS work was 15mm and the probe current was adjusted so that all spectra collected have a dead time of between approximately 8-12%. This ensured a high signal-to-noise ratio in the EDS signal; greatly reducing peak overlap and reducing Mg double peak artifacts. Peak overlap hinders element identification and increases uncertainty in quantitative analysis. Double peaks of Mg are due to the pulse processor's inability to parse the high counts of Mg received at the detector. Figure 20 is a calculation demonstrating the resolution of EDS in the SEM used in this research. It shows that EDS resolution is restricted to about 4.5 μ m. EDS compositional analyses of phases smaller than 4.5 μ m can therefore show what elements are present but determining relative proportions of each element is not accurate. The compositions of phases larger than the x-ray resolution, such as eutectic phases, are more reliable. An average of ten EDS measurements is used to approximate the composition of eutectic phases.

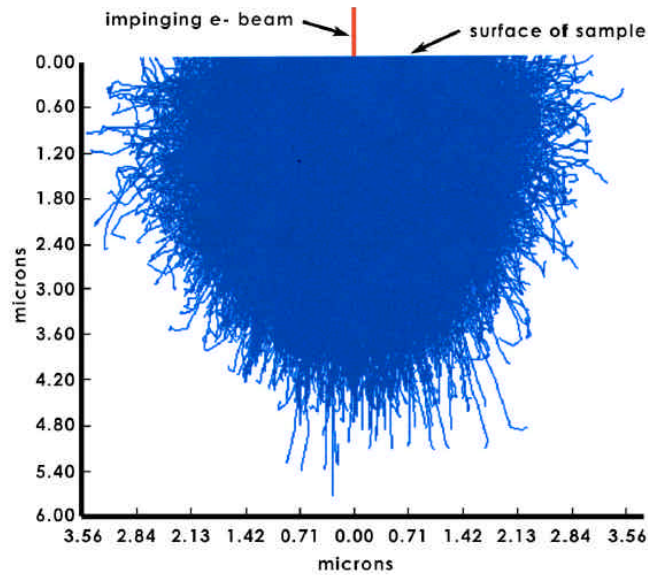


Figure 20 - Interaction Volume of 15keV Electron Beam Interacting with Pure Mg

EDS maps were collected for each alloy in representative locations in the microstructure at approximately 200-300X magnification. Each scan was collected over a 5 hr period ensuring good separation of signal and noise for good resolution. The EDS maps for Mg have a slight variation in intensity that is an artifact of the instrument. EDS line scans were also used to give an indication of coring within the matrix. The line scans were taken at a slight higher magnification 300-500X.

4.3 Dendrite Coherency

After an extensive literature review into the experimental methods of previous dendrite coherency work, it was decided that the continuous torque measurement technique was best suited to be applied to Mg alloy research. Therefore, an apparatus was designed similar to the apparatus used by G. Chai [24,25]. Materials used for dendrite coherency measurements were obtained from the same ingots used to machine

the thermal analyses samples. Compositional analysis of the samples was performed prior to each measurement, but only if the samples came from a different ingot from the one used for thermal analysis.

4.3.1 Design of Experiment

A customized unit was fabricated for dendrite coherency analysis. Similar to our thermal analysis system, the dendrite coherency system was designed to vertically lower and raise a sealed crucible into a resistance furnace. The system is suitable for use with Mg alloys due to its sealed nature and cover gas system. For these experiments the same cover gas was used.

The apparatus was designed to solidify 150-175 grams of Mg while a vane attached to a rheometer is rotated at a constant velocity. The effects of rotational velocity on the coherency point have already been discussed. In this work, a rotational speed of 0.05rpm was used in order to reduce any shear applied to the formation of the solid network. The rheometer used is a Brookfield DV-III Pro-5HB. A software package Rheolab v2.4 coupled with the rheometer is used to output torque versus time data. Rheometers collect data from a fluid by the torque resisting rotation of a spindle or vane. The torque range of the Brookfield DV-III Pro-5HB is 0-28.7mNm. This range was selected because of its similar nature to the rheometer used by Chai [24,25]. Figure 21 shows the dendrite coherency apparatus.



Figure 21 - Dendrite Coherency Apparatus.

One of the most important parameters when performing any rheological experiment is the selection of the spindle or vane. For our application, a variation of the concentric cylinder experiment was used. This involves the rotation of a four blade vane within the sample, the vane rotation is considered to act as a rotating cylinder. The selection of the technique and design of the vane was performed with the help of Dr. N. Tonmukayakul, research scientist with expertise in rheology [40]. The vane was designed followed standard rheological procedure in which the vane dimensions are exactly $\frac{1}{2}$ the dimension of the sample in both the radial and vertical directions. The vane dimensions were 0.875in diameter and 1.25in height. A drawing of vane inside the crucible is show in Figure 22.

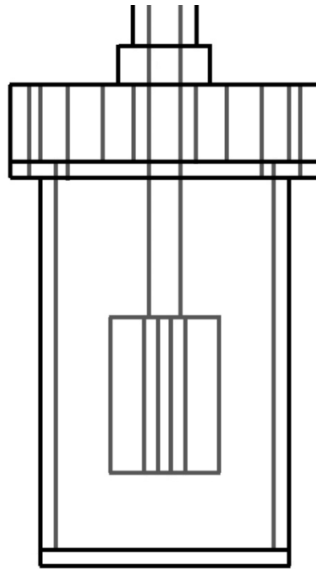


Figure 22 - Vane positioned inside Crucible.

This design required the Mg sample to be placed into the crucible, containing the vane, in solid form. Therefore the cylinder sample was machined into four equal sized wedges, which could then be placed into the crucible along with the vane. A single thermocouple was also introduced into the melt. The thermocouple was positioned vertically at the center of the vane and radially half way between vane edge and crucible wall. The thermocouple was calibrated in the same manner as for thermal analysis experiments. The thermocouple was required in order to have temperature and cooling rate profiles for the dendrite coherency experiments. This will allow the determination of the approximately fraction solid formed at the coherency point.

The dendrite coherency apparatus was tested and calibrated against the published values using Al alloy AA356.2. The results for the coherency points were in good agreement. Prior to use the Brookfield DV-III Pro-5HB was fully serviced and calibrated by the technicians at Brookfield Engineering.

4.3.2 Procedure

The preparation for the dendrite coherency experiments begins with loading the vane onto the rheometer and booting the rheometer. A simple procedure of zeroing the rheometer is required before each use. At this point the Rheolab software is started and configured to record data to a text file. The thermocouple is then vertically placed at the center of the vane, the radial position is fixed by the apparatus. The crucible, loaded with the wedge shaped samples, is then loaded and attached to the vertical loading arm.

The furnace is preheated to a temperature 750°C. Once the furnace is preheating the data collection system can be started and configured to record the data to a text file. After the furnace has reached temperature the sample can be lowered into the furnace vertically using the linear actuator. When the melt temperature rises upon 450°C the cover gas is required for melt protection. The pressure release gauge on the cover gas cylinder is always set to 2psi to ensure the same cooling condition between melts. The melt is equilibrated to a temperature of approximately 700°C. Once the melt has reached temperature the crucible was removed from the furnace using the linear actuator and allowed to cool in room temperature air with the cover gas flowing. As soon as the crucible has stopped its motion, the rheometer is started and the vane begins to rotate at 0.05rpm. Temperature, torque, and time data is collected throughout solidification.

Once the sample has completed the transformation, the procedure is repeated twice making a total of three solidification experiments per sample. Two samples were prepared for each alloy making a total of six dendrite coherency solidification experiments per alloy. After the experiments were completed the Mg sample was removed with the vane remaining embedded in the sample. The sample material below

the vane was removed using an abrasive cut-off wheel. This material used for compositional analysis follow the experimentation. The vane was removed from the sample by remelting the remaining Mg.

5.0 Results and Discussion

This chapter is dedicated to the results and a discussion of the results of the experimental procedures explained in Chapter 4.

5.1 Compositional Analysis

Composition of each alloy was measured in the as-received condition and then following our experimentation was performed again. This was to ensure that the techniques used did not create significant shifts in the compositions. Minor changes in composition of Fe and Ni are known to greatly affect the mechanical and corrosion properties of Mg alloys. Although the microstructural effects of these impurities are unknown, for this research the goal is to investigate the microstructure of the commercially specified alloy compositions. Table 3 compares the as-received and as-cast compositions of the alloys used in this Research. The compositional analysis performed on alloy AXJ530 was performed by Massachusetts Materials Research, Inc. This was necessary due to the alloy additions of calcium and strontium, the Spectromax LMXM3 was not calibrated for these elements.

All the compositional results did fall within the specifications of the alloys. Several of the alloys, including AXJ530, are experimental or not widely used alloys. Therefore the ASTM specifications are lacking. The results for alloys AM50, AM60, and AZ91 are well within the compositional requirements set forth.

Table 3 - Compositional Analysis of All Alloys

	Al	Mn	Si	Zn	Fe	Cu	Ni	Ca	Sr	Other (each)	Mg
AM20											
as-received	1.86	0.4452	0.0189	0.0072	<0.0006	0.0008	<0.0020			each <0.02	bal.
<i>std. dev.</i>	<i>0.0392</i>	<i>0.0044</i>	<i>0.0014</i>	<i>0.0003</i>	<i>0.0009</i>	<i>0.0002</i>	<i>0.0006</i>				
as-cast	1.87	0.4142	0.0186	0.0074	<0.0006	0.001	<0.0020			each <0.02	bal.
<i>std. dev.</i>	<i>0.0508</i>	<i>0.0155</i>	<i>0.0029</i>	<i>0.0004</i>	<i>0.0008</i>	<i>0.0004</i>	<i>0.0014</i>				
AM40											
as-received	3.8	0.3857	0.0092	0.0267	<0.0006	<0.0005	<0.0020			each <0.02	bal.
<i>std. dev.</i>	<i>0.0853</i>	<i>0.0219</i>	<i>0.0011</i>	<i>0.0007</i>	<i>0.0008</i>	<i>0.0002</i>	<i>0.0005</i>				
as-cast	3.58	0.3249	0.0076	0.025	<0.0006	<0.0005	<0.0020			each <0.02	bal.
<i>std. dev.</i>	<i>0.1578</i>	<i>0.0421</i>	<i>0.002</i>	<i>0.0025</i>	<i>0.0009</i>	<i>0.0004</i>	<i>0.0011</i>				
AM50A											
as-received	4.34	0.3077	<0.0024	0.0155	<0.0006	<0.0005	<0.0020			each <0.02	bal.
<i>std. dev.</i>	<i>0.1061</i>	<i>0.0159</i>	<i>0.0011</i>	<i>0.0005</i>	<i>0.0007</i>	<i>0.0002</i>	<i>0.0012</i>				
as-cast	4.39	0.3058	0.0033	0.0152	<0.0006	<0.0005	<0.0020			each <0.02	bal.
<i>std. dev.</i>	<i>0.1821</i>	<i>0.055</i>	<i>0.0009</i>	<i>0.0011</i>	<i>0.0004</i>	<i>0.0002</i>	<i>0.0007</i>				
ASTM	4.4-5.4	0.26-0.60	0.10 max	0.22 max	0.004 max	0.010 max	0.002 max			0.02 max	bal.
AM60B											
as-received	5.24	0.3056	0.0044	0.0474	<0.0006	<0.0005	<0.0020			each <0.02	bal.
<i>std. dev.</i>	<i>0.0558</i>	<i>0.0116</i>	<i>0.0011</i>	<i>0.0006</i>	<i>0.0014</i>	<i>0.0002</i>	<i>0.0008</i>				
as-cast	5.29	0.2301	0.0038	0.0467	<0.0006	<0.0005	<0.0020			each <0.02	bal.
<i>std. dev.</i>	<i>0.1438</i>	<i>0.0467</i>	<i>0.0005</i>	<i>0.0022</i>	<i>0.0006</i>	<i>0.0005</i>	<i>0.0006</i>				
ASTM	5.5-6.5	0.25-0.60	0.10 max	0.22 max	0.004 max	0.010 max	0.002 max			0.02 max	bal.
AXJ530											
as-received	4.97	0.35	0.02	<0.01	<0.01	<0.01	0.03	3.01	0.15	each <0.02	bal.
as-cast	3.67	0.26	0.01	<0.01	<0.01	<0.01	0.03	2.6	0.11	each <0.02	bal.
AZ91E											
as-received	8.5	0.2337	0.0331	0.73	<0.0006	<0.0005	<0.0020			each <0.02	bal.
<i>std. dev.</i>	<i>0.1336</i>	<i>0.0432</i>	<i>0.0031</i>	<i>0.0453</i>	<i>0.0015</i>	<i>0.001</i>	<i>0.0014</i>				
as-cast	8.62	0.2	0.007	0.53	<0.0006	<0.0005	<0.0020			each <0.02	bal.
<i>std. dev.</i>	<i>0.28</i>	<i>0.05</i>	<i>0.001</i>	<i>0.02</i>	<i>0.001</i>	<i>0.0003</i>	<i>0.001</i>				
ASTM	8.1-9.3	0.17-0.35	0.20 max	0.4-1.0	0.005 max	0.015 max	0.001 max			each <0.01	bal.

5.2 Thermal Analysis Results

The non-equilibrium thermal analysis solidification experiment was performed nine times for each alloy in this research. The data output from each experiment was time and temperature data for each of the two thermocouples used as part of the two thermocouple technique. The data was then manipulated to form three subsequent curves, a derivative with respect to time for each thermocouple, and a temperature difference curve which was defined by equation 3.1.

$$\Delta T = T_E - T_C \quad (3-1)$$

These five curves represent the results of the two thermocouple thermal analysis technique. Each experiment will have its respective set of five curves. These curves were then analyzed to determine solidification events. The major solidification events that occurred in all the Mg-Al alloys were: start of solidification, end of solidification, solidification temperature range, solidification time range, start of eutectic reaction, liquidus cooling rate, and solidus cooling rate. These features were determined for each experiment and then averaged to determine the values reported.

The start of solidification and the start of the eutectic reaction were determined using the technique shown in Figure 5. The figure below shows the determination of the start of solidification of an AM60 experiment, the red curve represents the temperature of the edge thermocouple and the blue curve represents the derivative of temperature with respect to time. The edge thermocouple was used as it will solidify before the center thermocouple. This same curve was used to determine the liquid cooling rate, which was determined by the value of the derivative of temperature curve right before the start of solidification.

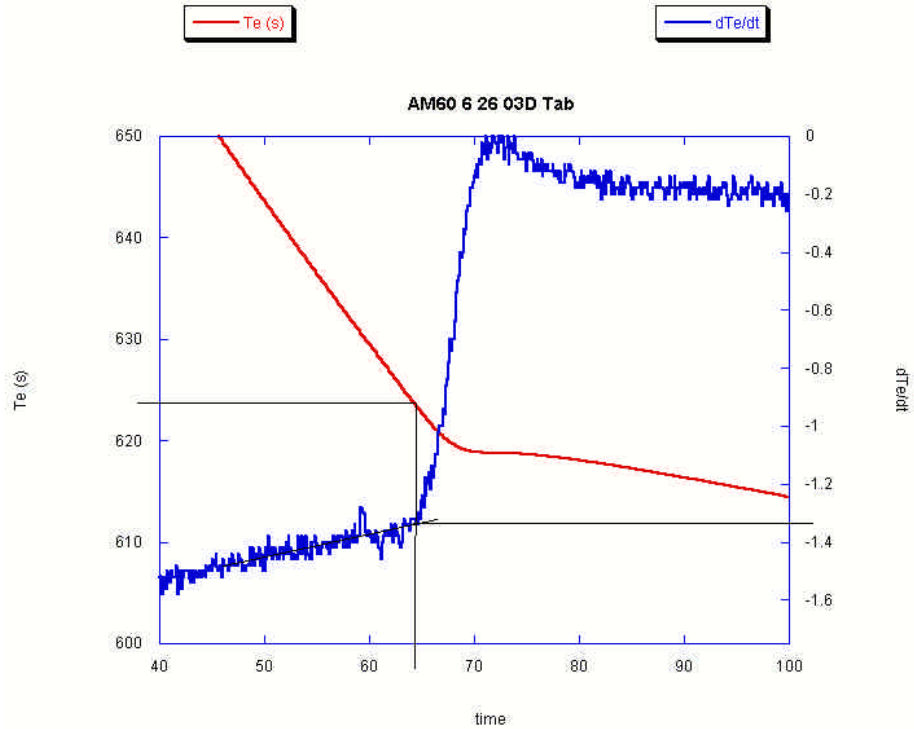


Figure 23 - Start of Solidification in AM60.

A similar curve was constructed to evaluate the start of the eutectic reaction. Once again the edge thermocouple will be used to determine the initiation of the reaction. The figure again represents an actual experiment performed with alloy AM60. The procedure of using the drastic change in the derivative curve was used to determine the time and temperature of the solidification event. The eutectic reaction temperature (T_{eutectic}) is given as 434.7°C for the experiment shown in Figure 24.

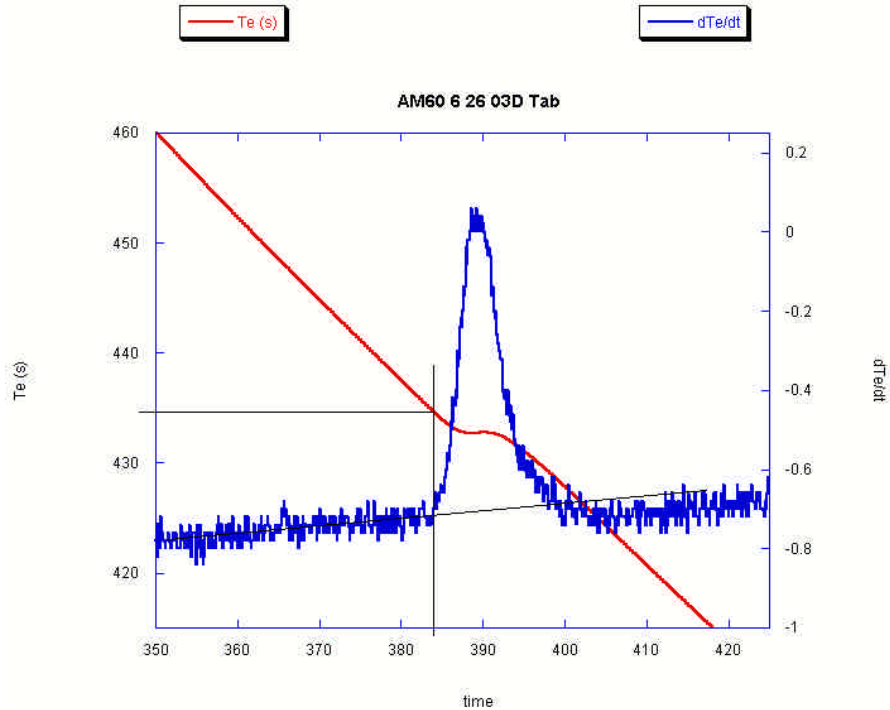


Figure 24 - Start of Eutectic Reaction in AM60.

The end of solidification was determined via the method set forth by Backerud and Tamminen [18,22], shown in Figure 6. The center thermocouple was used for the end of reactions, as it will be the last part of the sample to solidify. Once again the method involves the use of the derivative curve. A line tangent to the solid cooling rate was drawn; the point at which this tangent line reached the down slope of the peak to the eutectic solidification is defined as the time and temperature of the end of solidification. The solid cooling rate was given by the value at which the tangent line was drawn from. In the figure below the end of solidification (T_{end} , t_{end}) is given as 431.5°C at 403.5s. The solid cooling rate is shown as 0.63°C/s.

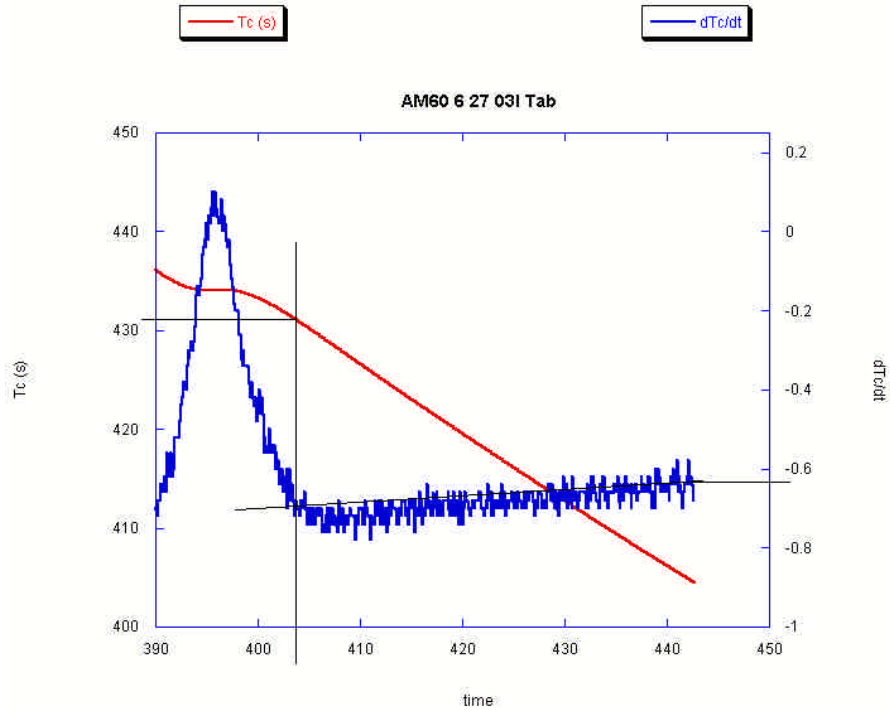


Figure 25 - End of Solidification in AM60.

The following figures are representative cases of the thermal analysis results for each of the alloys tested. These graphs show all five of the important curves, T_c , T_e , dT_c/dt , dT_e/dt , and ΔT ($T_e - T_c$). A second graph for each alloy shows the derivative of the temperature plotted versus the temperature. This curve is also useful for determining the important solidification information.

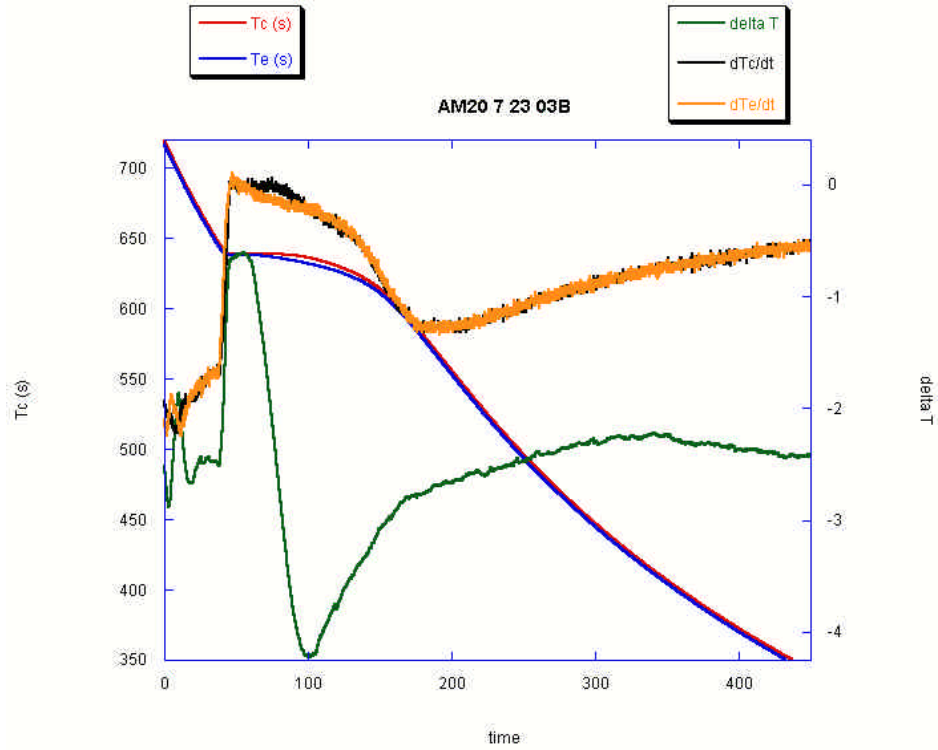


Figure 26 - Thermal Analysis Data for AM20.

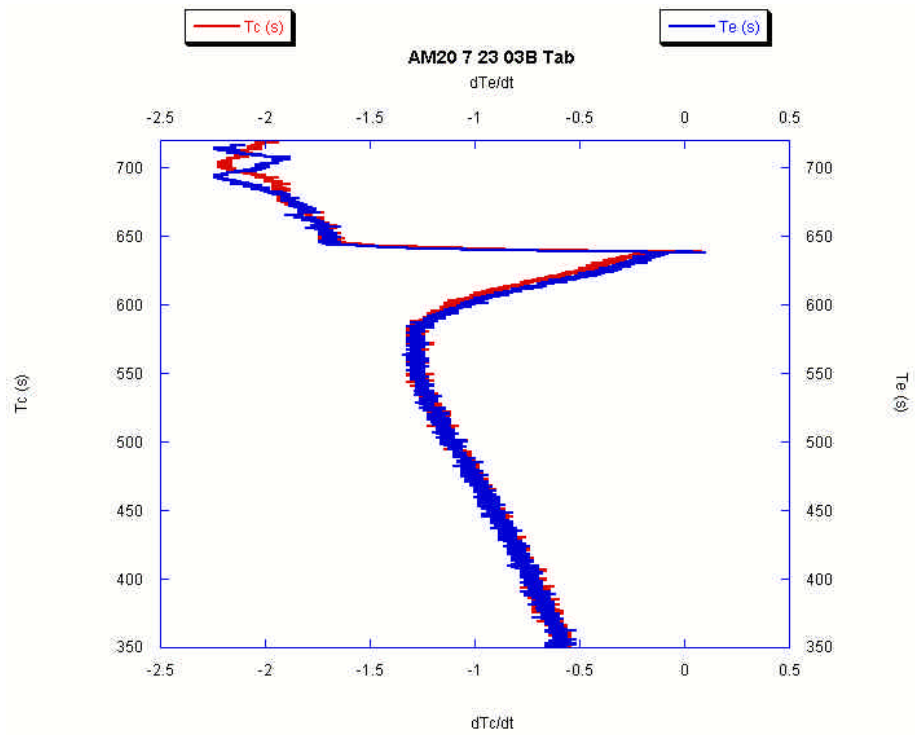


Figure 27 - Plot of Temp vs. dT/dt Data for AM20.

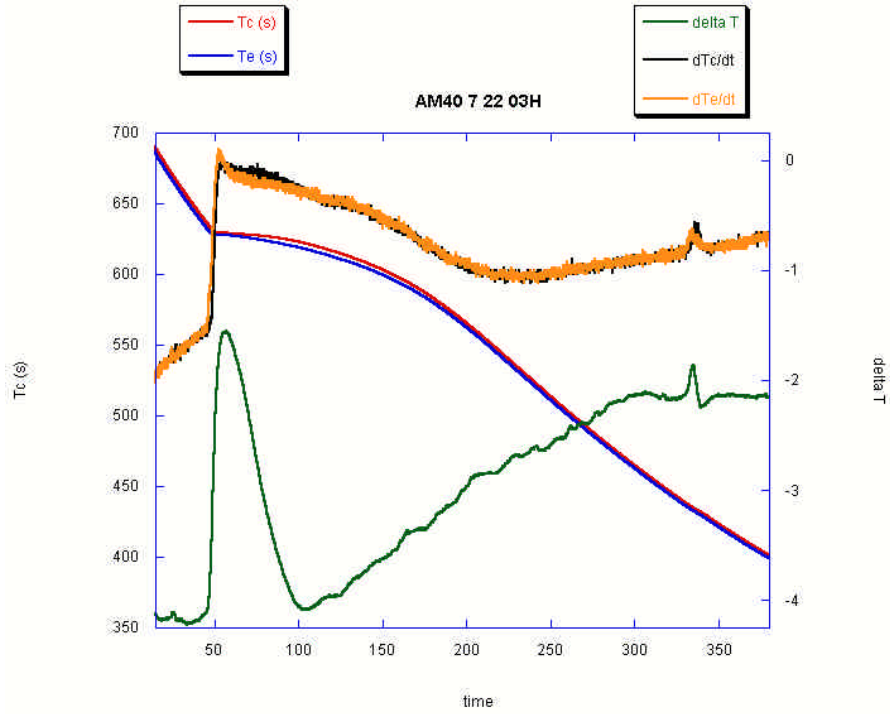


Figure 28 - Thermal Analysis Data for AM40.

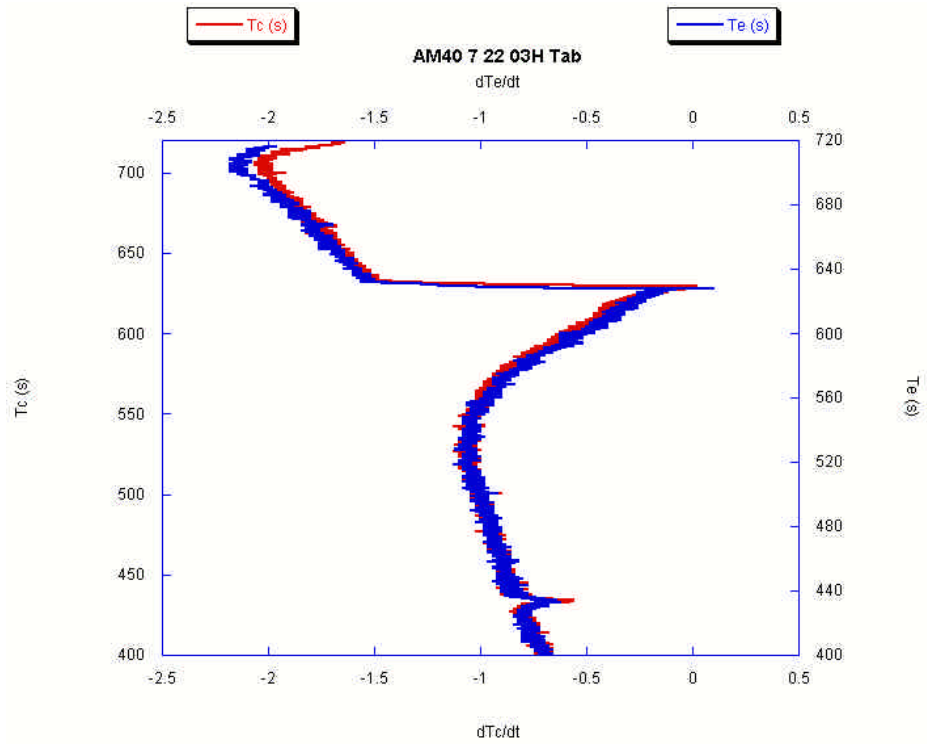


Figure 29 - Plot of Temp vs. dT/dt Data for AM40.

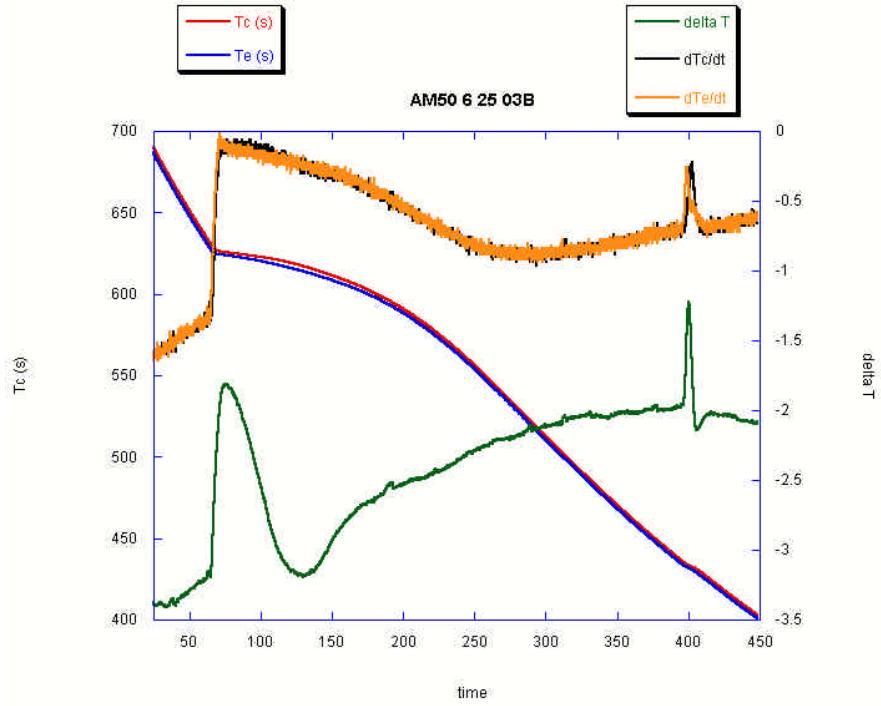


Figure 30 - Thermal Analysis Data for AM50.

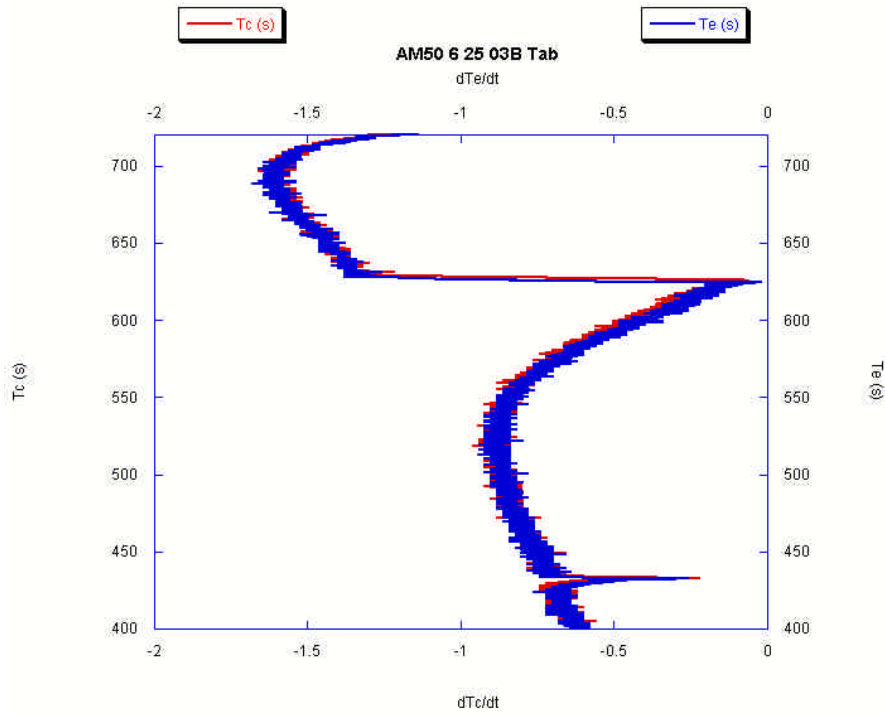


Figure 31 - Plot of Temp vs. dT/dt Data for AM50.

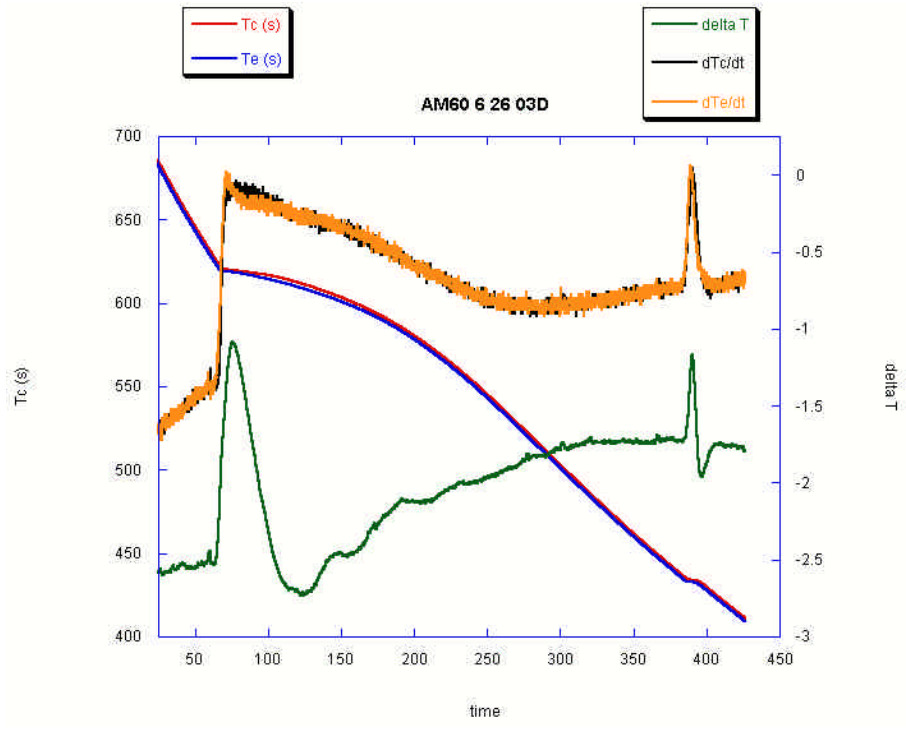


Figure 32 - Thermal Analysis Data for AM60.

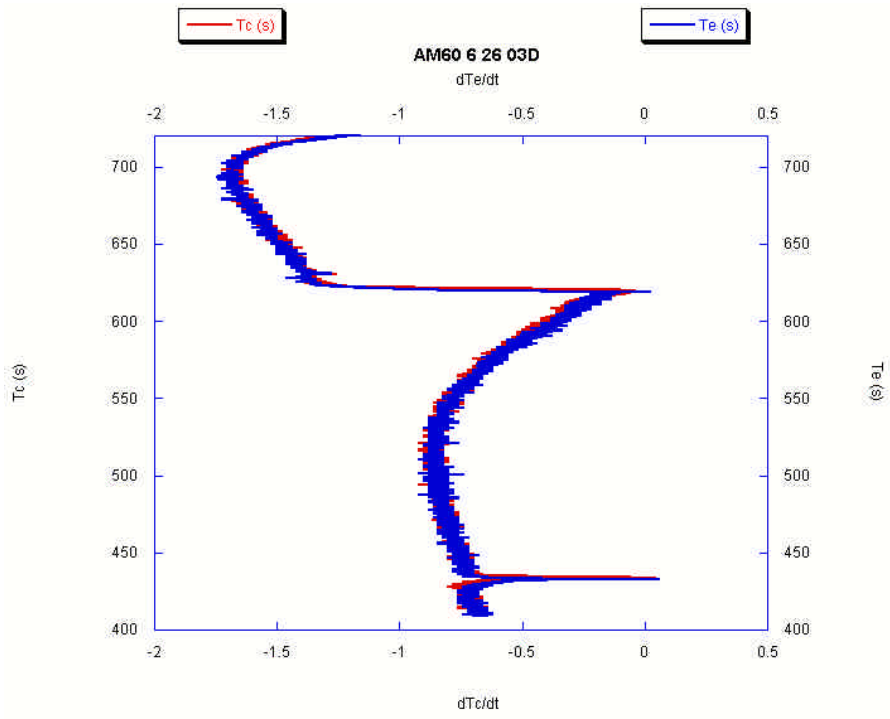


Figure 33 - Plot of Temp vs. dT/dt Data for AM60.

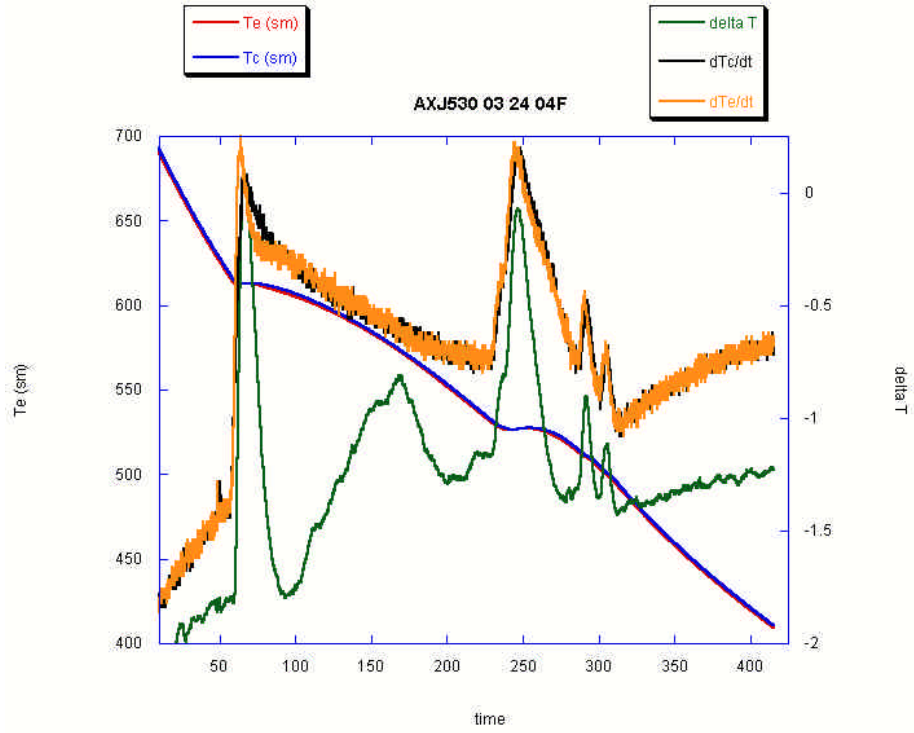


Figure 34 - Thermal Analysis Data for AXJ530.

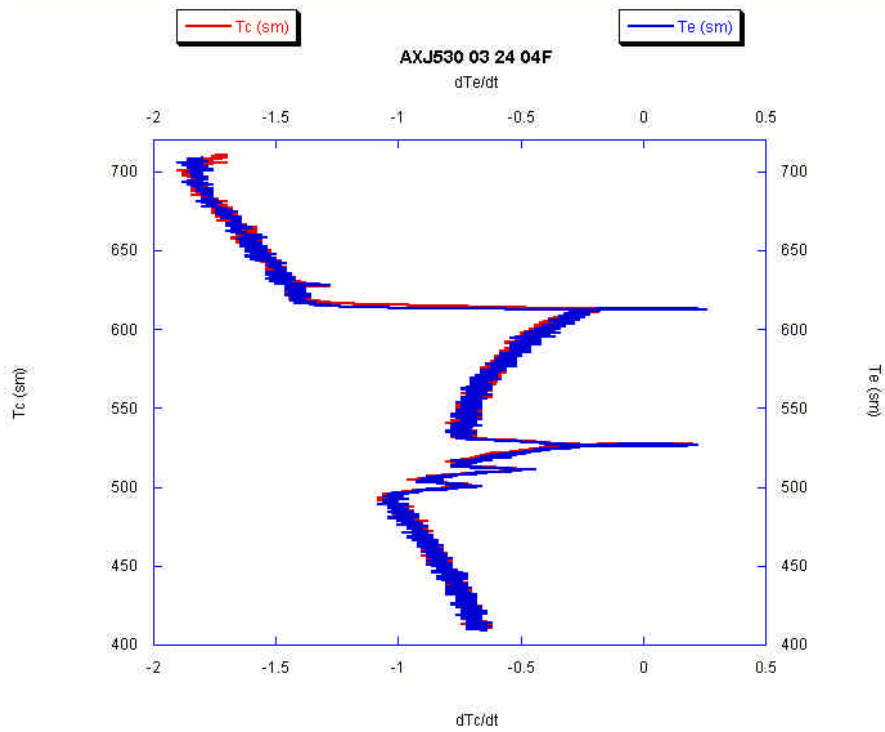


Figure 35 - Plot of Temp vs. dT/dt Data for AXJ530.

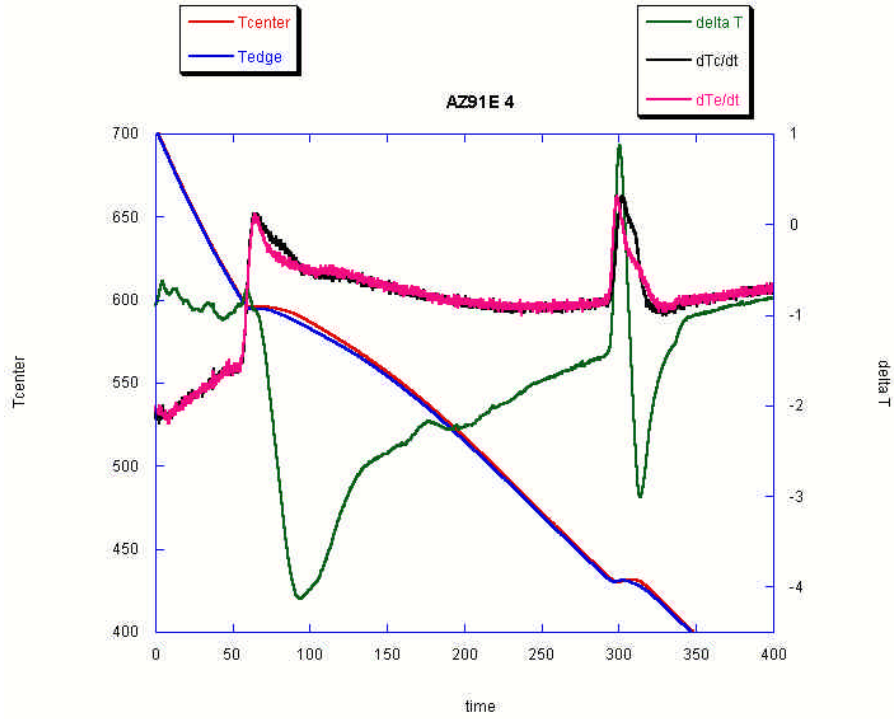


Figure 36 - Thermal Analysis Data for AZ91E.

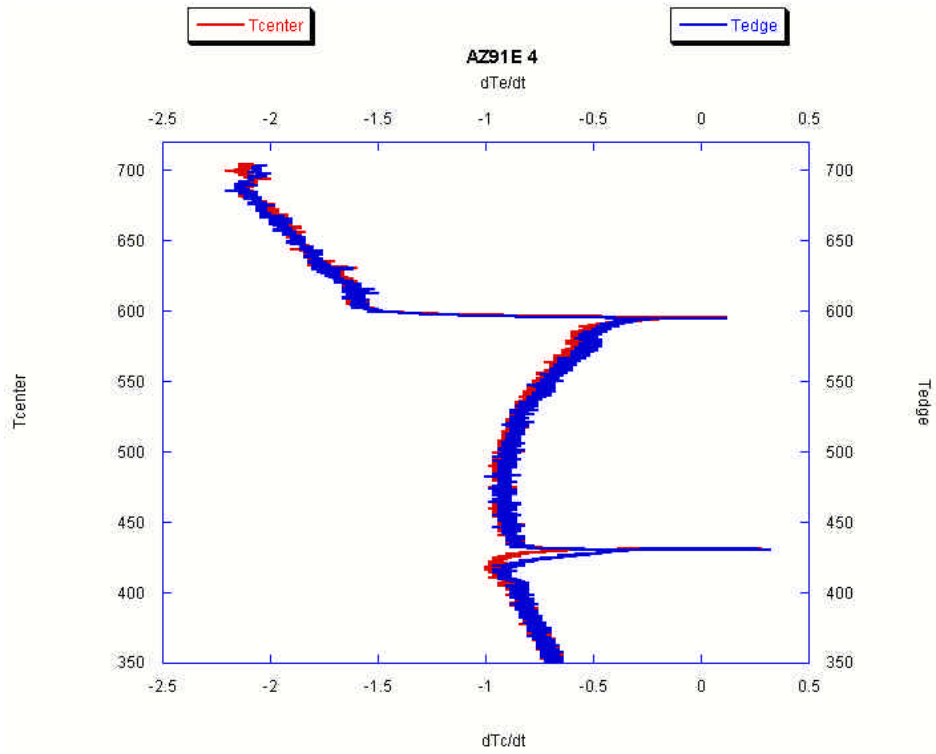


Figure 37 - Plot of Temp vs. dT/dt Data for AZ91E.

Each of the previous plots shows very similar trends. AM20 exhibits no visual eutectic reaction and no apparent end of solidification, probably due to AM20's low concentration of Al. This theory will be further investigated during the microscopy and phase analysis section. The AXJ530 plots are much different from the others. This can be attributed to either a complex eutectic reaction, or more likely a series of subsequent reaction leading to the final microstructure. These post-eutectic reactions occur at 512.9°C and 503.5°C respectively. Also the hump in the ΔT curve occurring at approximately 175sec in AXJ530 and AZ91E are probably due to the precipitation of a phase.

The data from each the nine experiments for each of the six alloys were determined and the values were averages. Table 4 shows the averaged results for each alloy.

Table 4 - Averages Results from Thermal Analysis Experiments.

	T-start (°C)	T- eutectic (°C)	T-end (°C)	T-range (°C)	time (s)	Liquid Cooling Rate (°C/s)	Soliding Cooling Rate (°C/s)
experimental values							
AM20	643.7					1.6	0.59
AM40	632.1	436	432.7	199.4	317.1	1.42	0.63
AM50A	627.6	433.8	430.2	197.4	332	1.35	0.65
AM60B	622.8	435.1	431.4	191.4	338	1.35	0.65
AXJ530	615.6	529.4	498	117.6	248.8	1.31	0.74
AZ91E	603.5	432.2	422.2	181.3	294.7	1.45	0.68
ASM published values							
AM50A	620		435	185			
AM60B	615		435	180			
AZ91E	598		468	130			

It was decided that Backerud and Tamminen's method of determining temperature versus fraction solid data for Al-Si alloys was not the correct method for

these Mg alloys. They assumed that the commercial Al alloys acted like binary Al-Si alloys. For these commercial Mg alloys, the assumption that they behave like Mg-Al binary alloys would only be an accurate assumption for several alloys, not the entire range of alloys. Therefore the fraction solid versus temperature data was calculated using a thermodynamic software package PanDat. This software package has the ability to calculate fraction solid versus temperature data during solidification using both the equilibrium and Schiel models and the ability to perform these calculations for actual alloy compositions, not simple binaries. Since the equilibrium and Schiel models are extreme they bound the results into a range of values. The following figures are the results of the solidification simulations performed using PanDat.

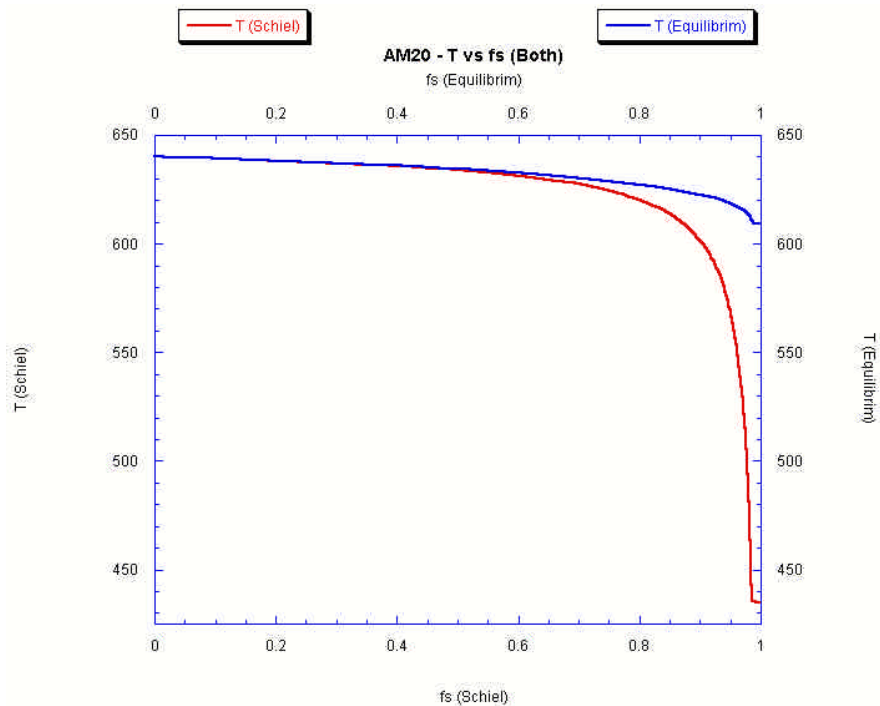


Figure 38 - Temperature vs. Fraction Solid Data from PanDat for AM20.

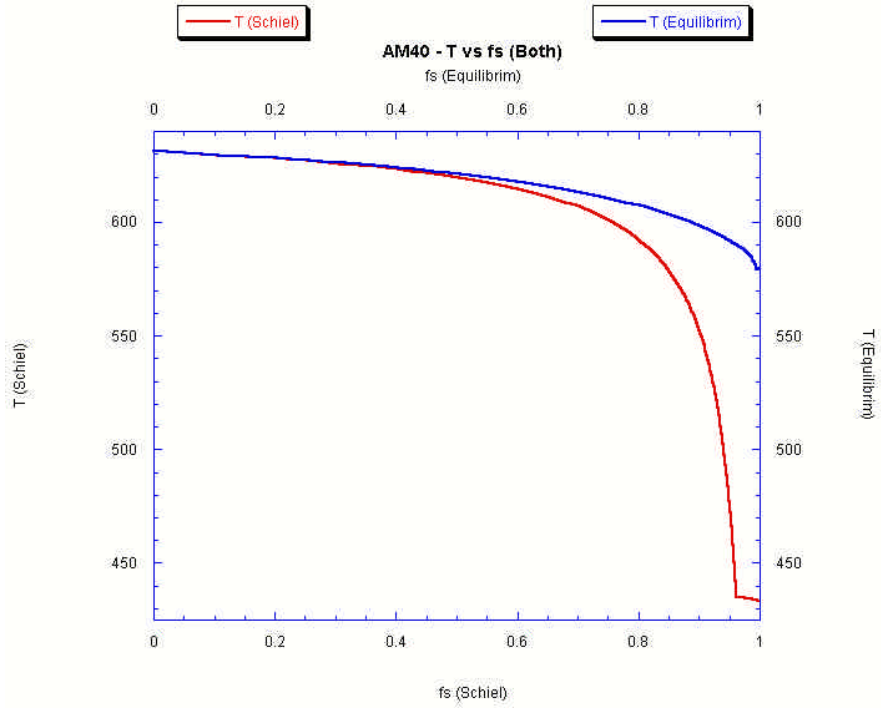


Figure 39 - Temperature vs. Fraction Solid Data from PanDat for AM40.

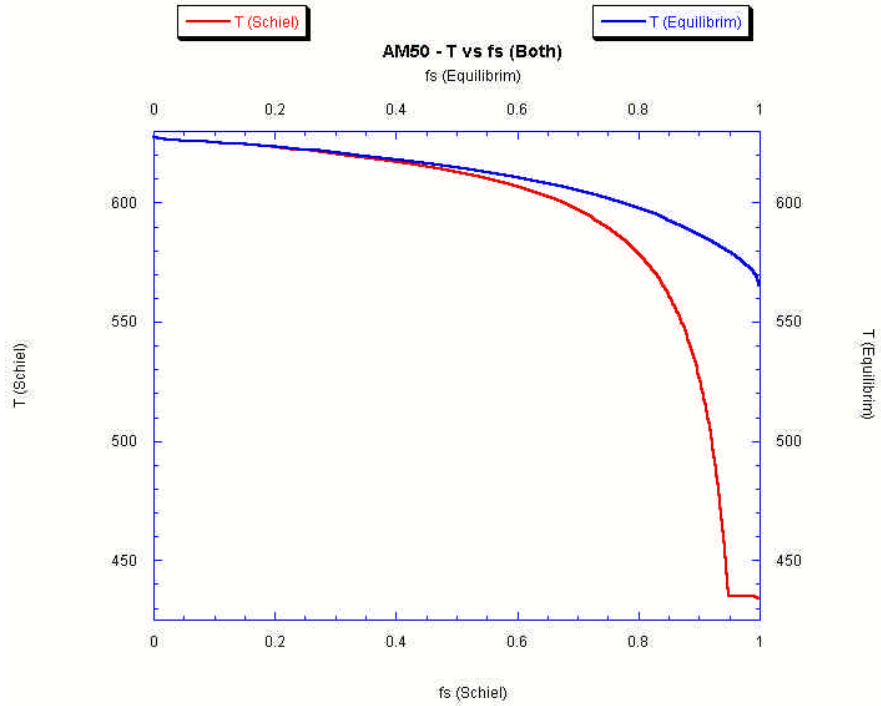


Figure 40 - Temperature vs. Fraction Solid Data from PanDat for AM50.

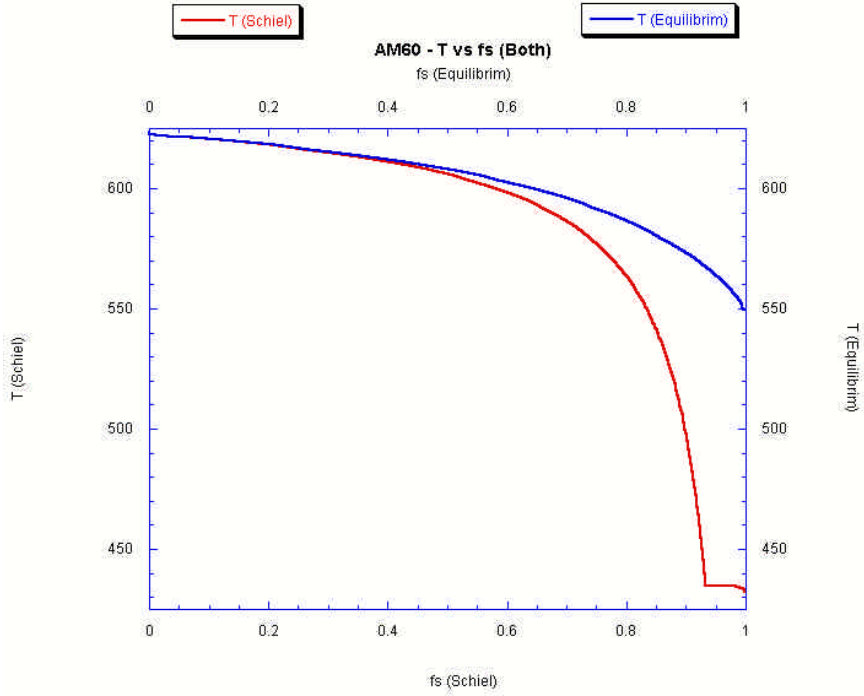


Figure 41 - Temperature vs. Fraction Solid Data from PanDat for AM60.

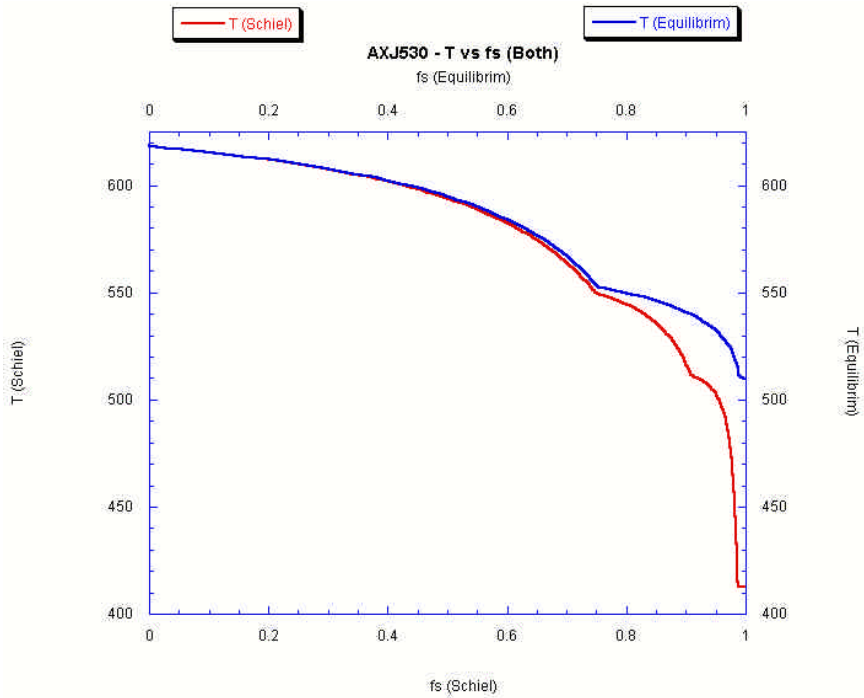


Figure 42 - Temperature vs. Fraction Solid Data from PanDat for AXJ530.

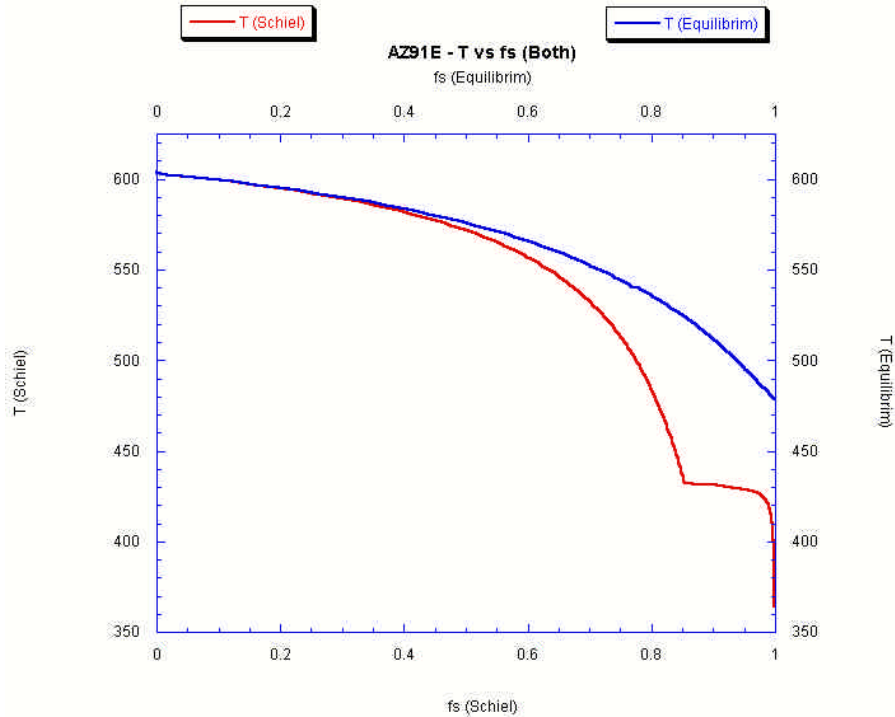


Figure 43 - Temperature vs. Fraction Solid Data from PanDat for AZ91E.

Upon inspection of these temperature versus fraction solid curves, it was apparent that the Schiel model and the equilibrium model are very similar for values up until approximately 50% solidified. For most of the alloys the end of solidification predicted from the Schiel model was dramatically closer to our actual data from our thermal analysis experiment.

The solidification simulations from PanDat also include a thermodynamic calculation of the sequence of solidified phases. This also includes the phases which thermodynamically are possible in the final microstructure. This information was very useful in determining the relative compositions of the phases found in the microstructural characterization section to follow.

5.3 Microstructural and Phase Analysis Results.

The microstructural characterization and phase analysis section will be broken down into three sections. These sections are the AM-type alloys, AZ91E, and AXJ530. The reason behind this was that the AM-type alloys, differ only in aluminum content, and therefore their microstructures are similar, only differences are the fractions of the phase present.

5.3.1 AM-type alloys.

The AM-type alloys include AM20, AM40, AM50, and AM60. The microstructures of these alloys differ only slightly. All the alloys form a primary phase of α -Mg, secondary phases contain Al and Mn, and a β -Mg₁₇Al₁₂ eutectic. PanDat solidification simulations were used to predict what phases would be present. These predictions were compared to the resultant microstructures and were found to be quite accurate. The phases predicted to be present in the as-cast microstructure for these alloys are: α -Mg, Al₁₁Mn₄, Al₈Mn₅, and β -Mg₁₇Al₁₂. Table 5 shows the results of the simulations and the proposed volume fraction of phase for the four AM-type alloys. All results appear to be confirmed from the microstructure characterization, except for the volume fraction of eutectic found in alloy AM20. The microstructure of AM20 shows larger quantities of Al-Mn phases than eutectic.

Table 5 - Solidification Simulation Results for AM-type Alloys.

	Volume Fraction of a-Mg	Volume Fraction of Al ₁₁ Mn ₈	Volume Fraction of Al ₈ Mn ₅	Volume Fraction of Eutectic Mg ₁₇ Al ₁₂
PanDat Solidification Simulations				
AM20	98.77	0.05	0.04	1.14
AM40	96.09	0.01	0.09	3.78
AM50A	94.76	0.02	0.13	5.01
AM60B	93.14	0.02	0.1	6.74

The general microstructure of these alloys can be seen in the following optical micrographs. Figure 44, is a low magnification optical image of alloy AM20. This alloy appears to have three phases present, the Mg matrix, as well as two phases which are bluish-brownish in appearance one in the shape of needles the other smaller more spherical in nature. The eutectic phase was very difficult to decipher using optical micrographs. The compositions of the phases will be analyzed later using energy dispersive spectroscopy (EDS). The optical image shown in Figure 45 used polarized light. In this image the phases are identified using arrows. Polarized light has the advantage of showing phases in different crystallographic orientations in different colors. The polarized light image also enhanced the coring effects of Al to the grain boundaries.

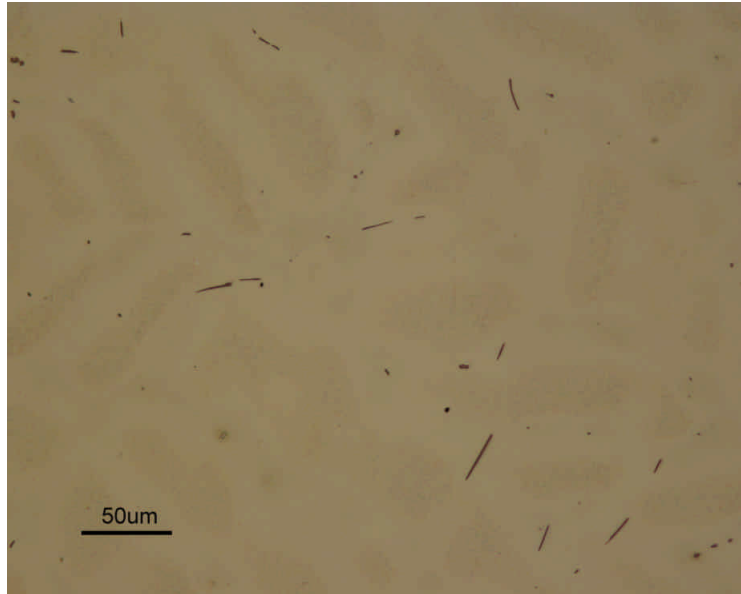


Figure 44 - Optical Micrograph of AM20. Etched for 2 sec with Acetic Glycol.

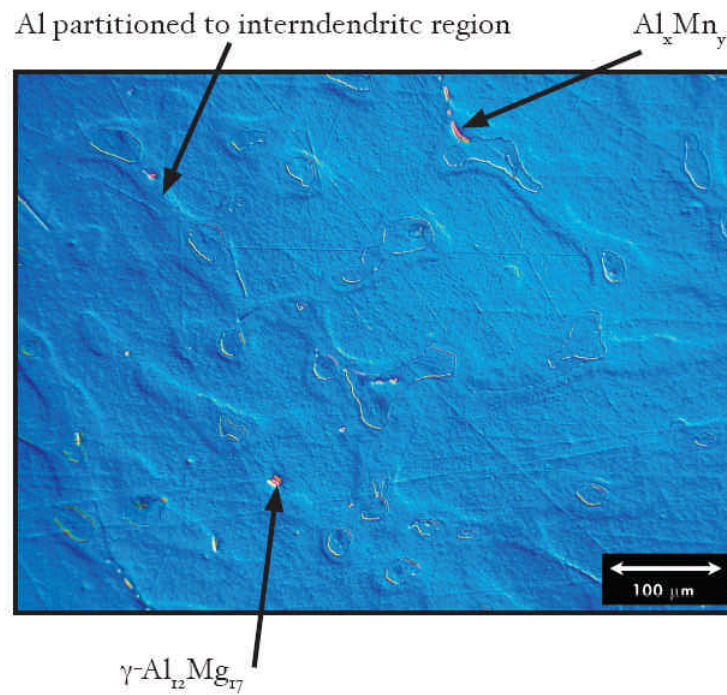


Figure 45 - Optical Micrograph of AM20, using Polarized Light. Etched for 2 sec with Acetic Glycol Etchant.

Figure 46 is a scanning electron microscopy (SEM) image of AM20. This micrograph clearly shows the same general microstructure. Both the needle-like and

spherical shaped phases present in the optical image are found, although the spherical phase appears to be more hexagonal at the higher magnification of the SEM. The eutectic phase is visually present in this SEM image, directly above the micron marker. EDS point scan were performed on several phases of each geometry. Both the needle-like and small hexagonal phases were found to contain Al-Mn, as well as impurities, such as Fe, in minute quantities. EDS phase analysis of these phases cannot be used to determine the exact composition; this is due to the three dimensional size restrictions of the electron beam interaction volume shown in Figure 20. Although the exact compositions cannot be determined, the EDS results agree with the PanDat phase predictions, of Al-Mn phases and the β -Mg₁₇Al₁₂ eutectic present.

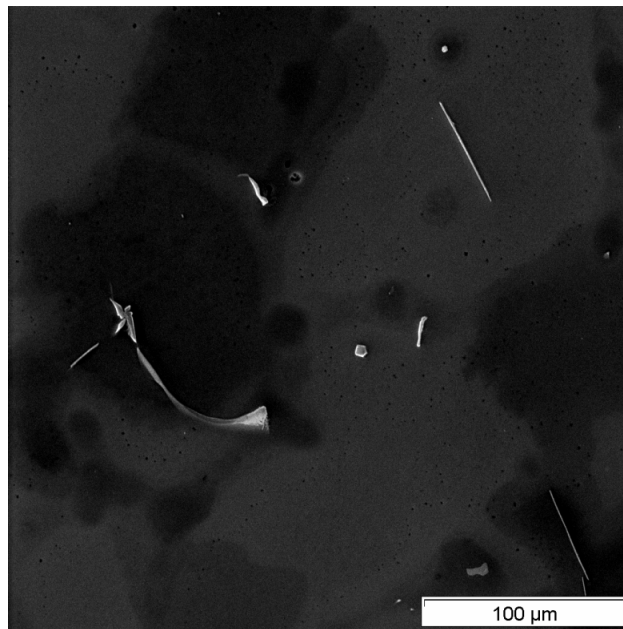


Figure 46 - SEM micrograph of AM20.

The general microstructure of AM40 shown in Figure 47 contains the same needle and small hexagonal phases, but in this alloy eutectic β -Mg₁₇Al₁₂ is visually significant.

Figure 48 is an SEM image, collected via the backscatter electron detector. This method of collecting images is highly sensitive to the atomic weight of the phases present. Therefore the bright phases have a combined atomic weight higher than the darker phase. This image clearly shows the matrix phase as black. The grayish phase is the eutectic phase; since Al and Mg have combined atomic weight greater than just Mg alone the phase appears brighter. The needle and small hexagonal phases which contain Al-Mn appear much brighter. Once again the PanDat simulation accurately predicted the present phases.

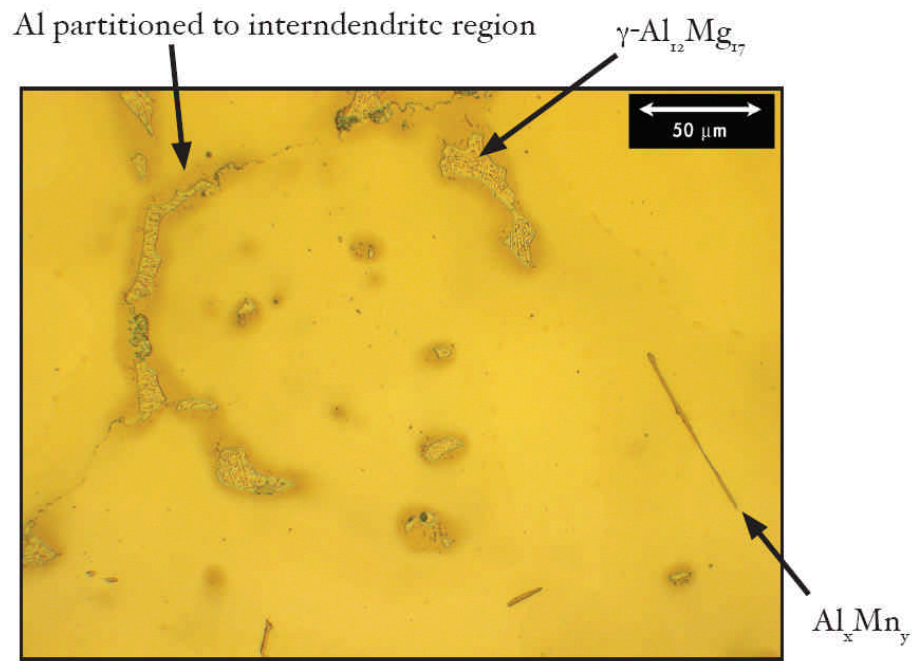


Figure 47 - Optical Micrograph of AM40. Etch for 2sec in Acetic Glycol.

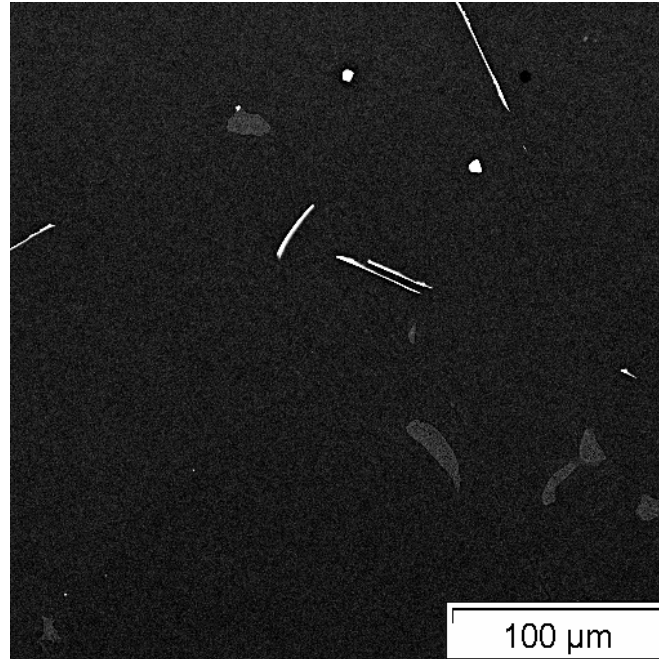


Figure 48 - SEM Image of AM40, Collected with Backscatter Electrons.

The microstructural analysis of AM50 and AM60 proves to be more of the same phases in slightly greater portions. With the greater amount of eutectic phase the eutectic phase was investigated to a higher detail than in the previous two alloys. The primary Mg phase solidifies with Al cored to the interdendritic regions. The interdendritic regions form primary β -Mg₁₇Al₁₂, during ingot cool down the Al rich interdendritic region transforms discontinuously. This creates “pearlitic” like colonies of the eutectic, also called a divorced eutectic. The difference between the primary and discontinuously precipitated can be seen with higher magnification or through the use of polarized light. Figure 49 shows an SEM image of AM60. The eutectic has a sponge-like appearance with darker islands of eutectic within the total larger mass of eutectic. The polarized lights images clearly show the discontinuous subgrains of the eutectic phase.

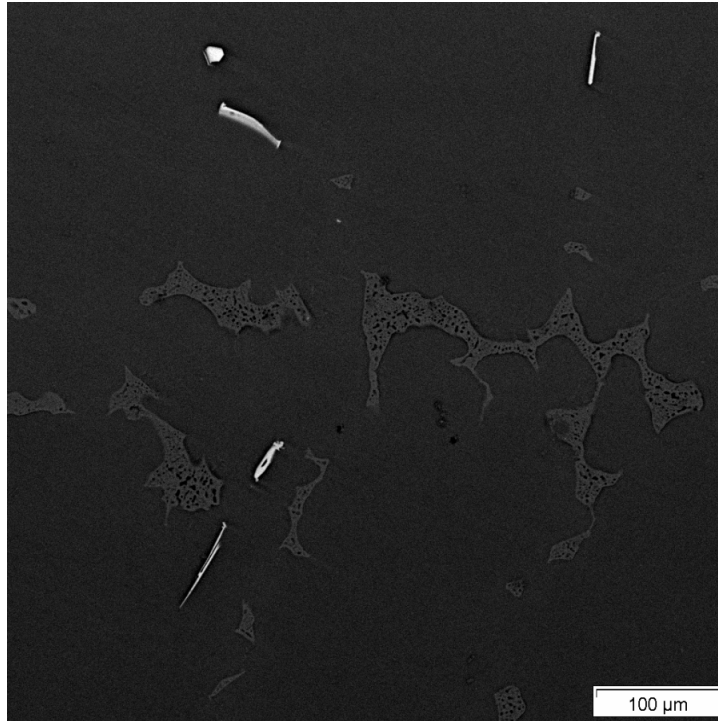


Figure 49 - SEM Images of AM60.

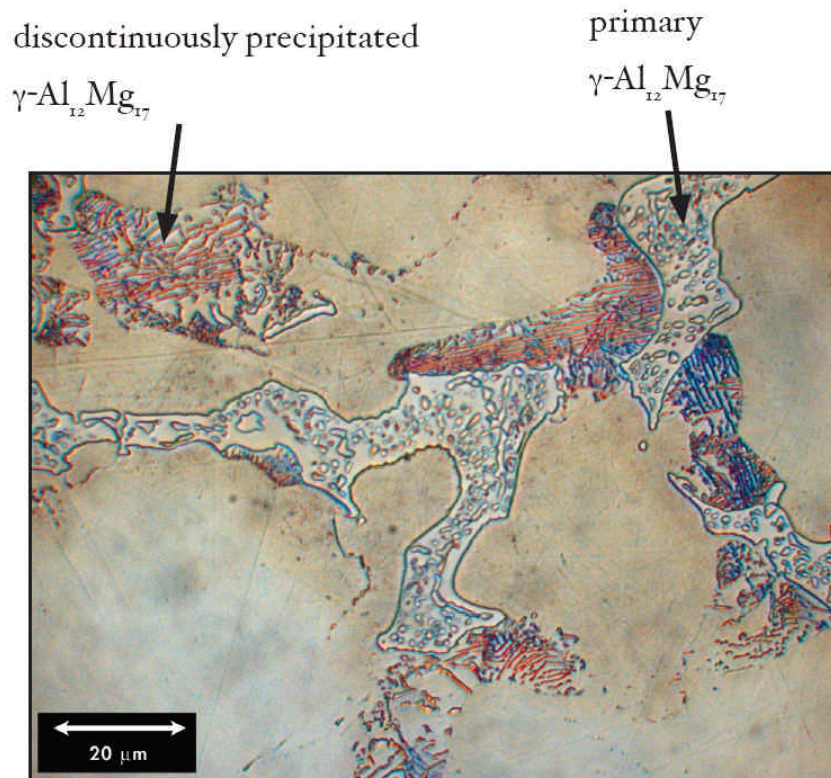


Figure 50 - High Magnification Optical Micrograph of AM60. Etched for 2sec in Acetic Glycol.

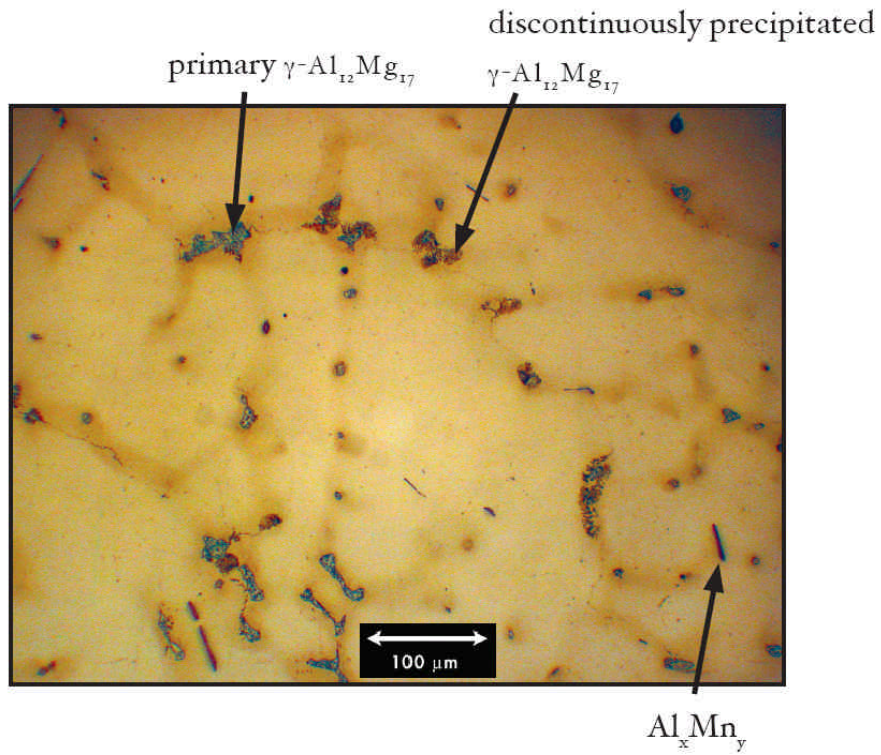


Figure 51 - Optical Micrograph of AM50, Using Polarized Light. Etched for 2sec in Acetic Glycol.

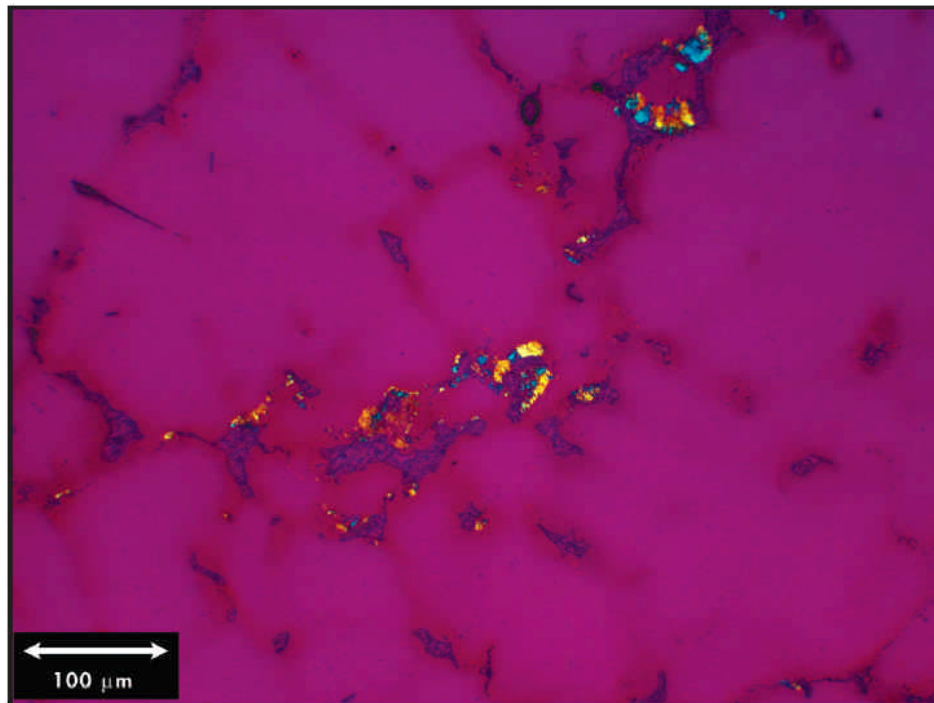


Figure 52 - Optical Micrograph of AM60, Using Polarized Light. Etched for 2sec in Acetic Glycol.

The extent of the coring of the primary α -Mg can be seen by performing an EDS line scan through the phase. Figure 53 shows the extent of the coring of Al and Mn. The line scan progresses through a eutectic colony, then through two primary Mg grains, then through another eutectic colony, and at the end it passes through an Al-Mn needle. The present of Al is highly segregated to the grain boundaries and the secondary and eutectic phases. Mn is only present in the Al-Mn needle phase.

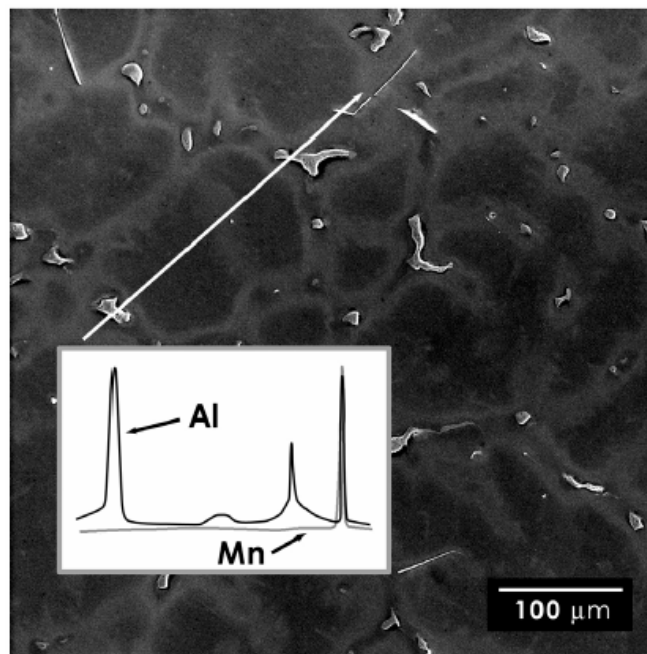


Figure 53 - EDS Line scan of AM50, Showing the extent of Al and Mn coring.

Further investigation of the Al coring and the presences of Mn only in the Al-Mn phase can be see in Figure 54. This represents an EDS map of the Al and Mn concentrations, performed on the same area as shown in Figure 49. When looking at the map images the brighter the area is the higher the percentage of the element.

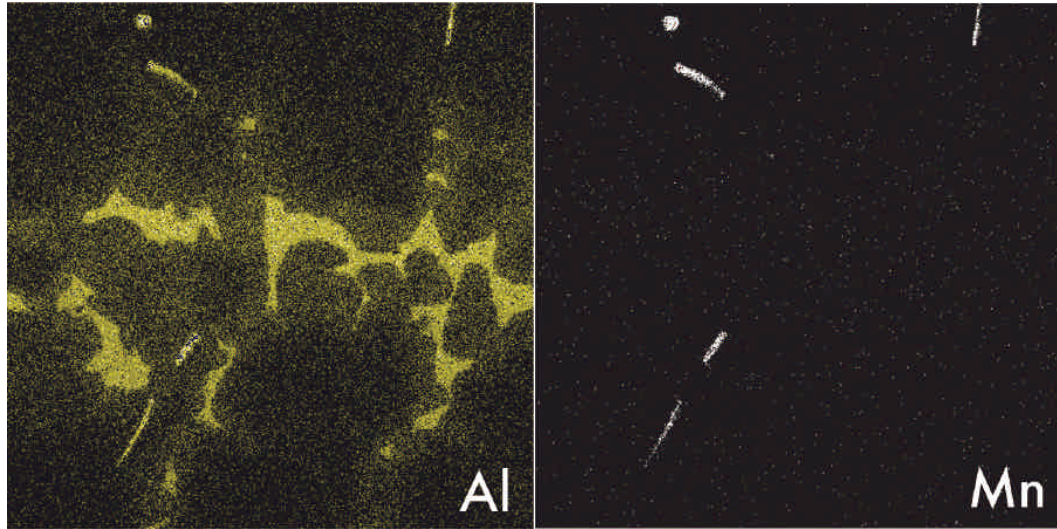


Figure 54 - EDS map of Al and Mn in AM60.

5.3.2 AZ91E.

The microstructural analysis of AZ91E was performed with a slightly more rigorous procedure. The reasons for this is that AZ91E is the dominant alloy used in industry today, and due to the higher concentration of alloy additions the microstructure is visually more interesting. The general microstructure of AZ91E is very similar to the AM-type alloys. The figures below are a bright field optical and SEM micrographs showing the general microstructure. The fraction of non-Mg phases is clearly greater, as would be expected due to the increased Al content. They phases present appear very similar after first inspection.

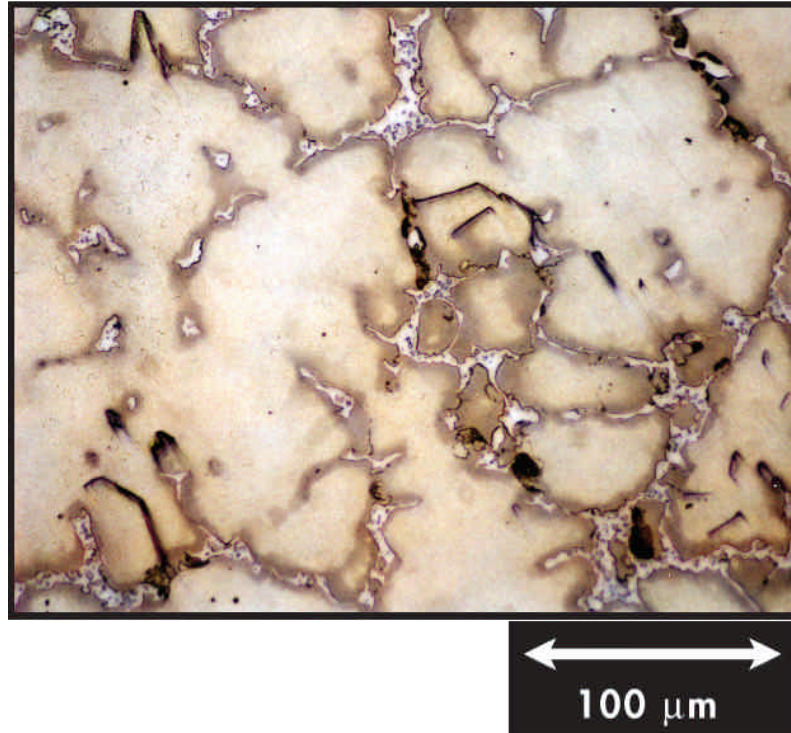


Figure 55 - Optical Image of AZ91E. Etched for 3sec in HF.

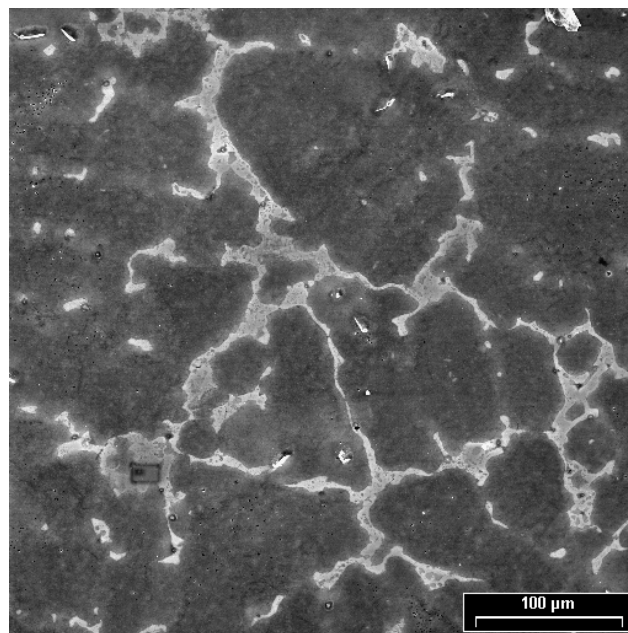


Figure 56 - SEM Image of AZ91E.

This alloy appears to have four phases present, primary Mg, a needle like phase, a spherical phase, and the eutectic. With a closer inspection of the eutectic it was found to be highly discontinuous, or divorced. Figure 57 contains a high magnification SEM image and EDS maps of Mg, Al, and Zn throughout the eutectic region. When looking at the map images the brighter the area is the higher the percentage of the element exists there. For example the Mg is brighter in the matrix than the eutectic phase.

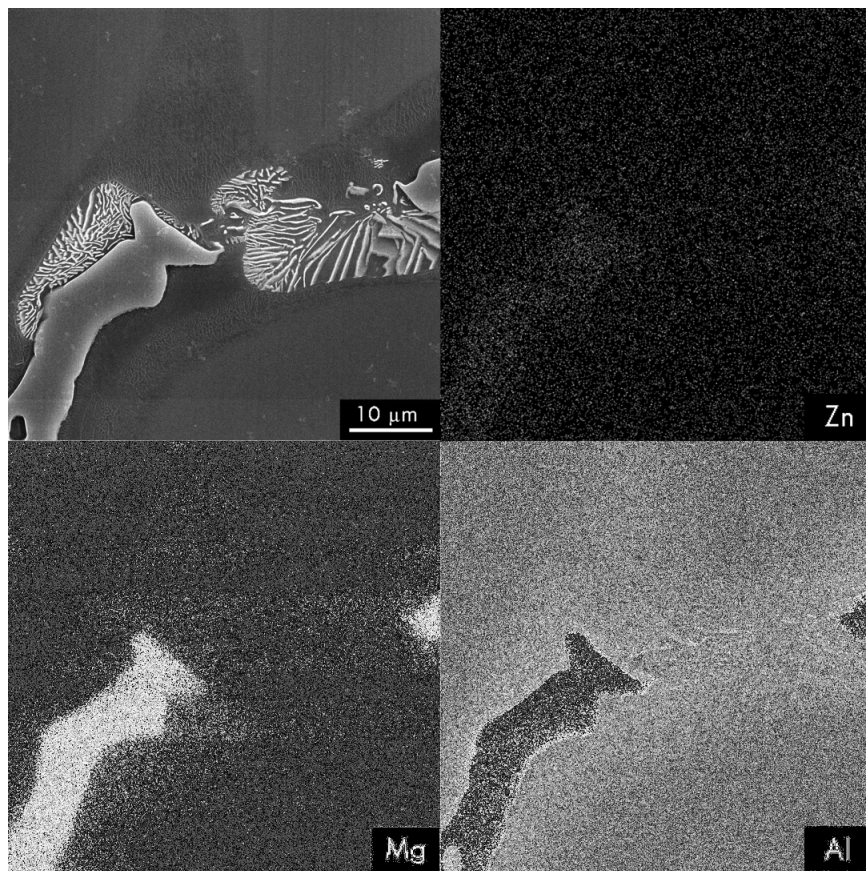


Figure 57 - SEM Image and EDS Map of Mg, Al, and Zn in AZ91E Eutectic.

Once again polarized light can be used to visualize the completely divorced eutectic found in the microstructure of AZ91E under these casting conditions.

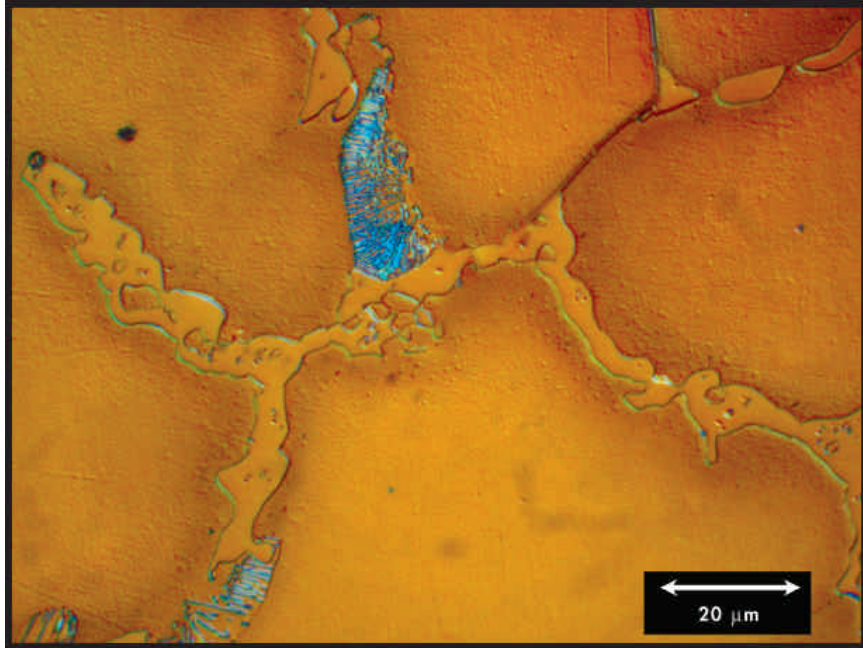


Figure 58 - Optical Micrograph of AZ91E using Polarized light. Etched for 2sec in Acetic Glycol.

The increased volume fraction of eutectic phase present allowed for quantitative EDS to be performed. Figure 59 below show the EDS spectrum collected from 200 seconds with a dead time of approximately 10%. Although the phase appears to be around the 4.5 μm required for accurate quantitative EDS, this 4.5 μm is also needed in the vertical direction into the sample. As the results show it appears that some Mg matrix was included in the collected spectrum. This is known since the calculated percentage of Mg was greater than would be expected in the $\beta\text{-Mg}_{17}\text{Al}_{12}$ eutectic. Both the EDS point scan and the map agree that most of the Zn in this alloy is segregated to the eutectic.

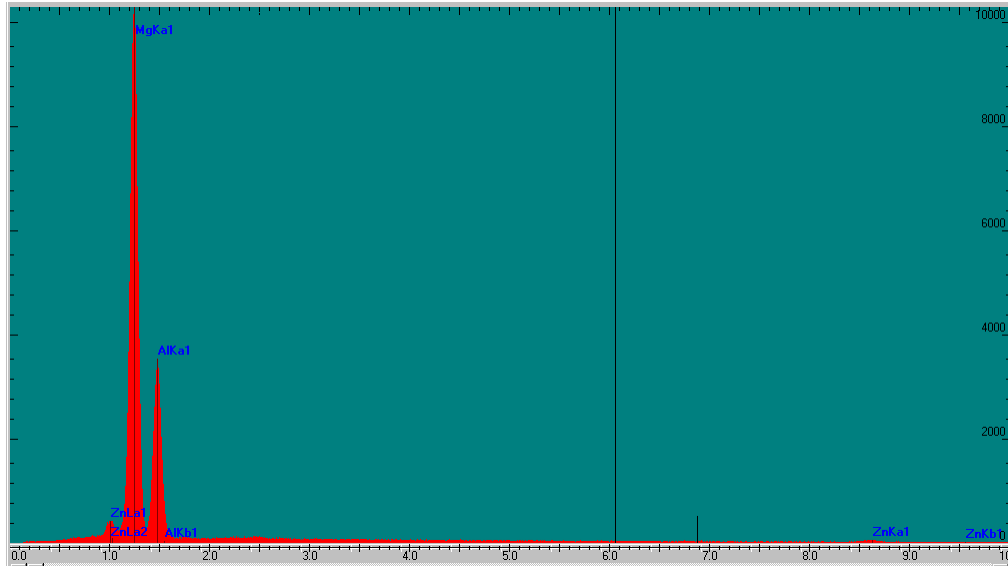


Figure 59 - EDS Spectrum of the Eutectic Phase in AZ91E.

The secondary phases have also been characterized using SEM images and EDS point scans. There are two different shaped secondary phases, a needle like shape and a hexagonal like shape.

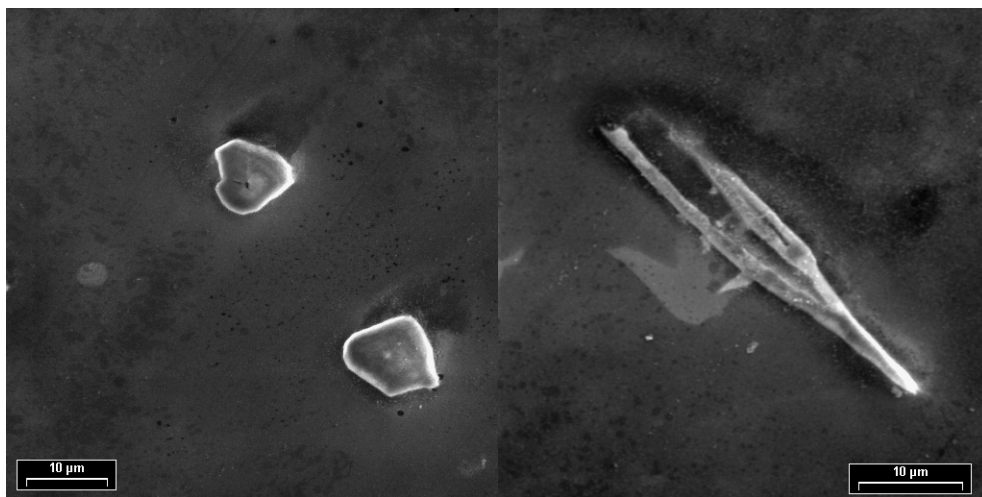


Figure 60 - SEM Images of Secondary Phases in AZ91E.

The EDS point scans prove that the two different shaped particles shown in Figure 60 are of the same composition. The phases appear to be the same phases found

in the AM-type alloys. Although the particles are smaller than the required $4.5\mu\text{m}$ for quantitative EDS analysis, the spectrum shows only trace amounts of Mg. The composition is very close to what would be expected with the knowledge that $\text{Al}_{11}\text{Mn}_4$ and Al_8Mn_5 could be present.

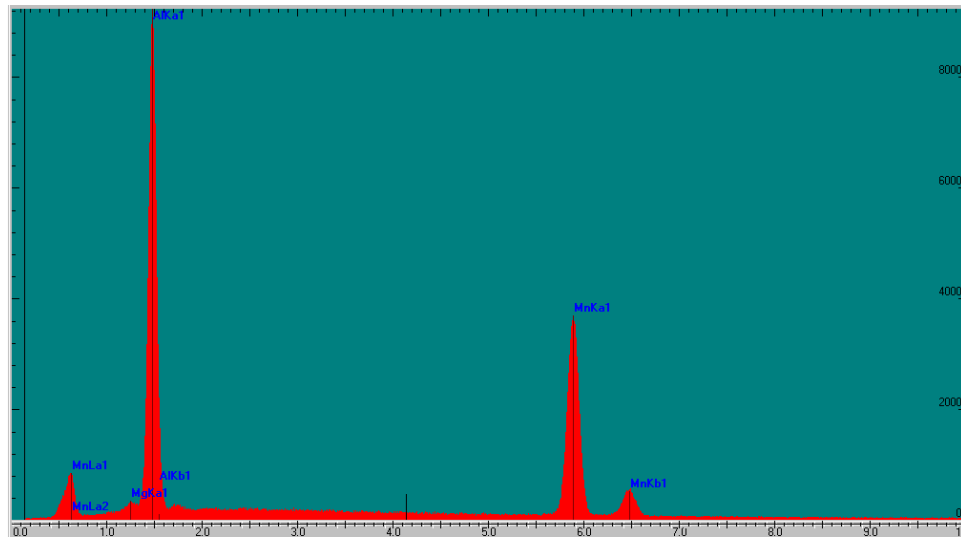


Figure 61 - EDS Spectrum of Secondary Phases in AZ91E.

5.3.3 AXJ530.

AXJ530 is an experimental alloy with alloying additions of Ca and Sr. These changes in alloy composition could have a substantial impact on the phases present and the phase composition. The PanDat solidification simulation predicted the presence of five distinct phases, α -Mg, Al_2Ca phase, $\text{Al}_{11}\text{Mn}_4$ phase, $\text{Mg}_{17}\text{Sr}_2$ phase, and β - $\text{Mg}_{17}\text{Al}_{12}(\text{Ca})$ eutectic. The microstructure characterization work and phase analysis work performed in this research did not find either the Al-Ca phase or the Mg-Sr phase. The Al-Ca phase although not found with the magnifications used in the work, are likely to be found on or within the eutectic structure is which found to contain like majority of

the Al and Ca in this alloy. For the Mg-Sr phase, this is likely do to the low quantity of Sr and high ratio of Mg to Sr of the proposed phase.

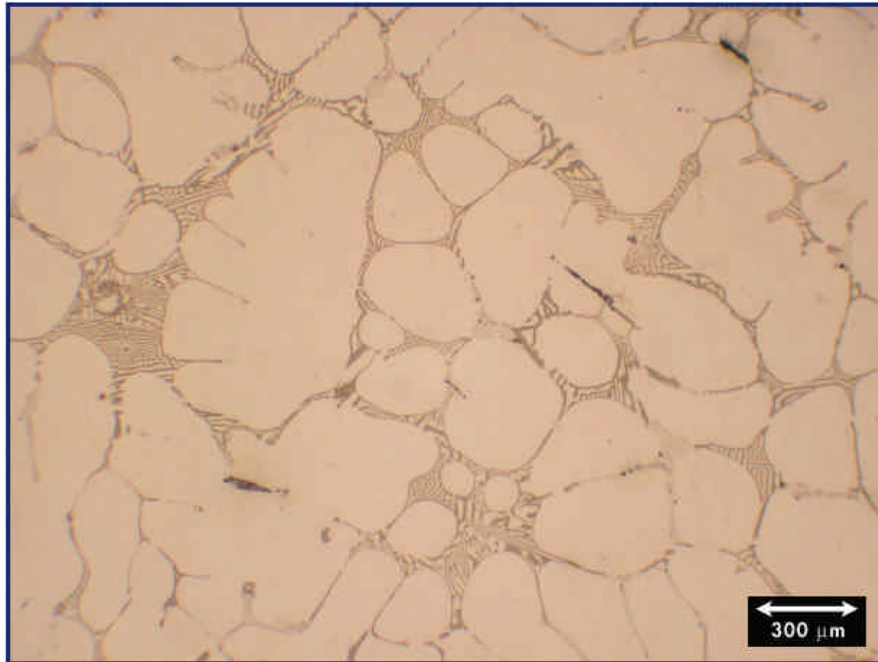


Figure 62 - Optical Micrograph of AXJ530. Etched for 3sec in Glycol Etchant.

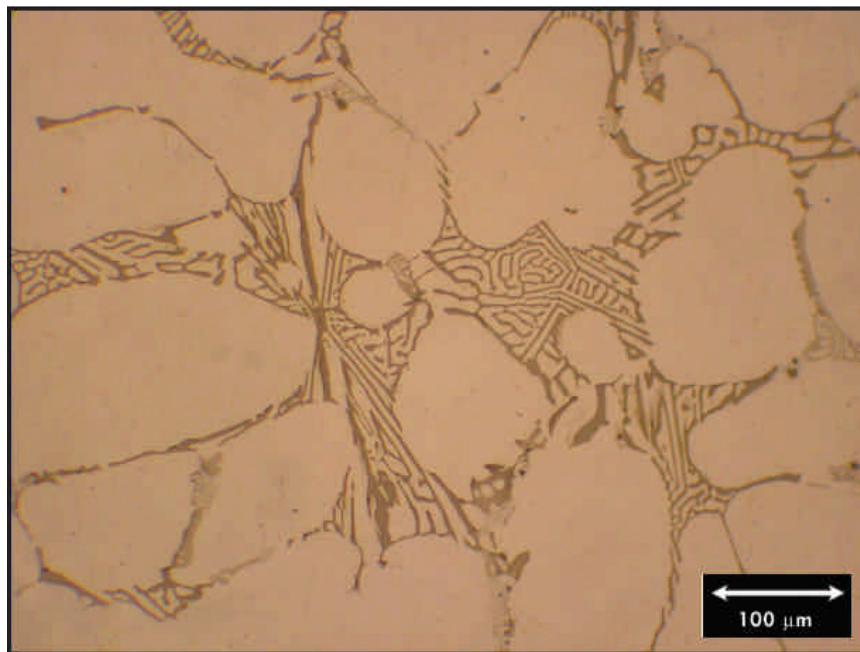


Figure 63 - Optical Micrograph of AXJ530. Etched for 3sec in Glycol Etchant.

The previous two figures show the general microstructure trend of alloy AXJ530. Needle-like phases similar to the Al-Mn particles of the other alloys are shown in Figure 62, while the discontinuous eutectic structure is clearly shown in Figure 63. The morphology of the primary Mg is again cellular or globular in nature, with the eutectic forming at the grain boundaries. The eutectic structure appears to be completely discontinuously precipitated; this is observed by the flakey almost lamellar structure. This probably accounts for the unusual behavior during the thermal analysis experiment, where there were several reactions happening after the eutectic structure initially formed. This alloy did not have the positive reaction to polarized light as some of the other alloys, although Figure 64 clearly shows the nature of the eutectic very clearly.

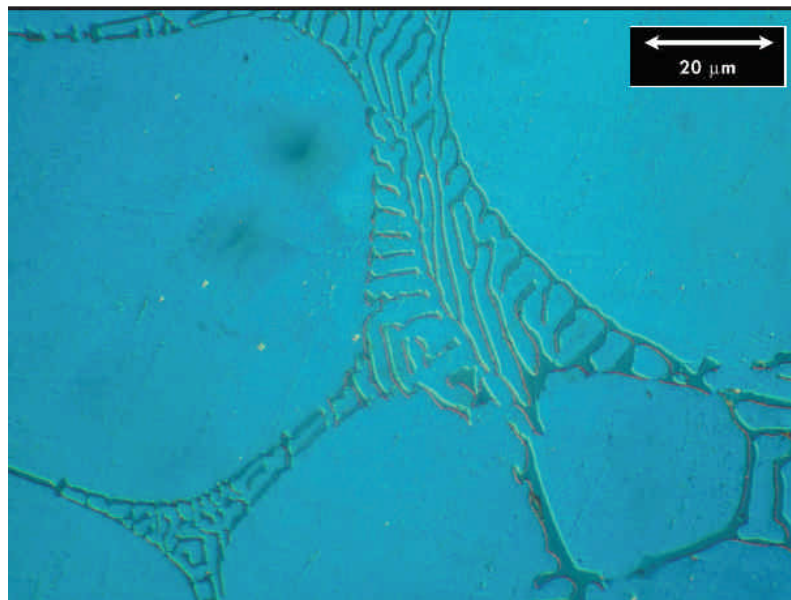


Figure 64 - Optical Image of AXJ530 using Polarized Light. Etched for 3sec with Glycol Etchant.

The presences of the other phases predicted by the solidification simulation were not found. EDS phase analysis was again performed. The needle shaped structure was again found to be Al-Mn particles, though in this alloy these particles contain about 4.5wt% Ca as well. The SEM was also used for imaging and EDS mapping of the elemental concentrations throughout this alloy. The figures below show the results of this analysis. It is clear that the Mn is completely segregated to the needle-like phase which has been determined to be an Al-Mn-(Ca) phase. The extent of Al coring also appears to be less severe than in the AM-type alloys and AZ91E. The EDS map images of Mg, Ca, and Al in Figure 66, show regions which have lower percentage of Mg. These areas could potential be regions with compositions closer to the predicted Al-Ca phase, although EDS points scan failed to prove this theory.

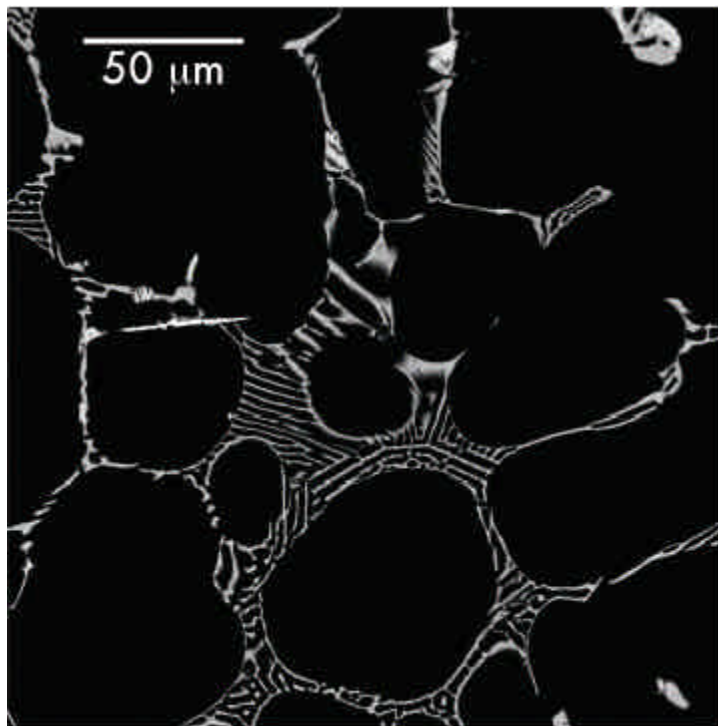


Figure 65 - SEM Image of AXJ50.

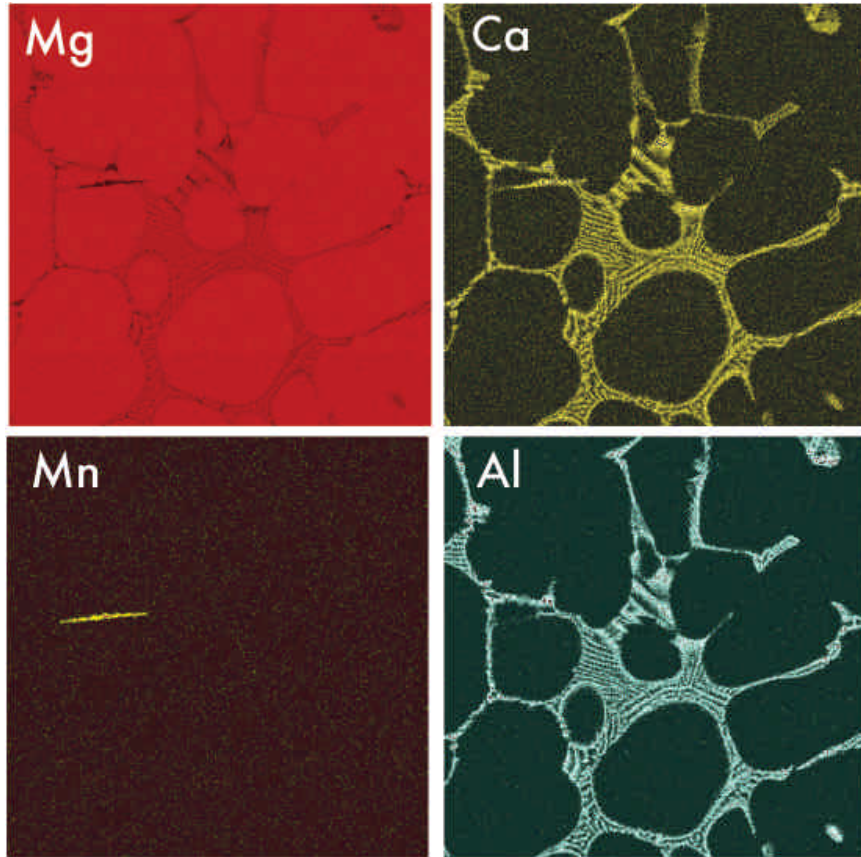


Figure 66 - EDS map of Mg, Ca, Mn, and Al in AXJ530.

5.4 Dendrite Coherency Results.

The dendrite coherency point was measured using two methods, the two thermocouple thermal analysis method and the continuous torque measurement method. The two thermal thermocouple analysis method as explained earlier was found by Veldman et al [33] to output results which are very different from the continuous torque method. Each of the nine thermal analysis experiments was analyzed to determine the proposed coherency point. Figure 67 shows the technique employed. The coherency temperature is correlated to the absolute minimum in the ΔT curve. The averaged results

for all nine experiments for each alloy are shown below in Table 6. These results confirm the conclusions of Veldman et al [33] that this method results in coherency points which do not agree with the continuous torque measurements. The nature of the continuous torque measurement is a direct experimental method; the two thermocouple method is an indirect method, and therefore an inferior method of determining coherency data.

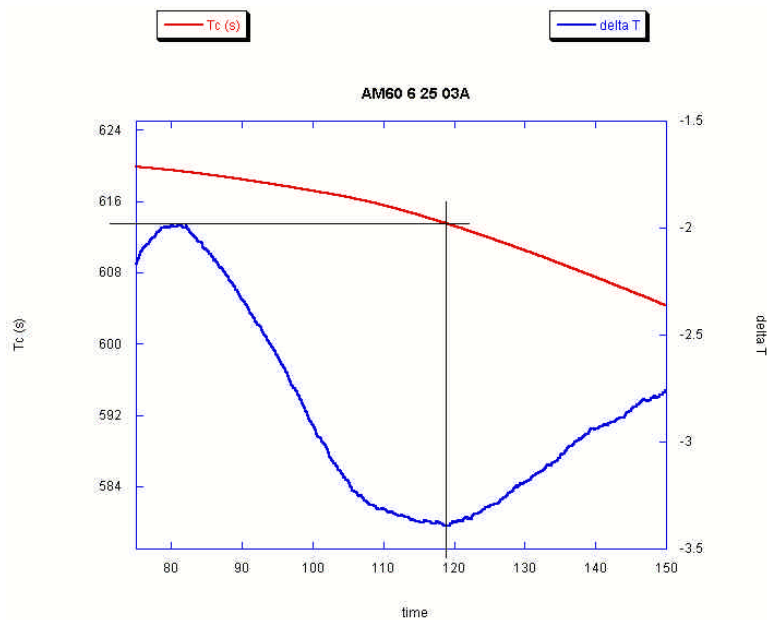


Figure 67 - Determination of Coherency Point via Two Thermocouple Technique in AM60.

The continuous torque measurement experiment was performed six times for each alloy. The output of the experiments was a set of torque versus time data and a temperature versus time data. Since both of these data sets share a common time access they can be plotted on the same graph. The torque versus time data captured for all six Mg alloys show very good resolution in determining the coherency point, but no clear rigidity point is seen. Similar to Arnberg and Chai [24,25] a secondary curve was created, torque versus fraction solid. This curve enhanced the distinction of both

coherency and rigidity points in their work. With respect to this work, the torque versus fraction solid curve appears to qualitatively show a trend that might be considered the rigidity point. The rigidity point is not reported as a distinct value, although the curve for each alloy will be reported. An example of this curve is shown in Figure 69.

Table 6 - Coherency Results for Continuous Torque Measurements and Two Thermocouple Thermal Analysis Techniques.

	Upper Coherency Temp (°C)	Lower Coherency Temp (°C)	Coherency Fs Range (Schiel)	Coherency Fs Range (Equilibrim)
continuous torque measurements				
AM20	639	637	0.095-0.331	0.096-0.344
AM40	630	628	0.052-0.241	0.052-0.243
AM50A	624	621	0.172-0.288	0.175-0.304
AM60B	619	616	0.173-0.284	0.177-0.295
AXJ530	610	604.5	0.239-0.355	0.241-0.359
AZ91E	597.5	590.5	0.140-0.280	0.143-0.290
two thermocouple thermal analysis				
AM20	636	632	0.404-0.587	0.428-0.649
AM40	626	621	0.308-0.471	0.321-0.514
AM50A	619	615	0.360-0.461	0.385-0.503
AM60B	614	608	0.336-0.467	0.351-0.503
AXJ530	610	605	0.253-0.352	0.255-0.356
AZ91E	584	580	0.375-0.42	0.385-0.455

The determination of the coherency point used in this work slightly differed from previous work as well. The method used for determining the coherency point was to take the derivative of the torque data with respect to time. This derivative data ($d\text{Tor}/dt$) was then plotted versus time, Figure 68. The derivative curve showed a distinct change over a range of times and temperatures. It was decided that this range of values would be reported as the coherency range. The coherency point was previously defined as a distinct point at which strength is first developed. This research is proposing that the transition to a coherent network occurs during a range of values. Therefore a range of

temperature and fraction solid values are reported in Table 6. The lower limit of this range can be considered the coherency point as defined by previous work.

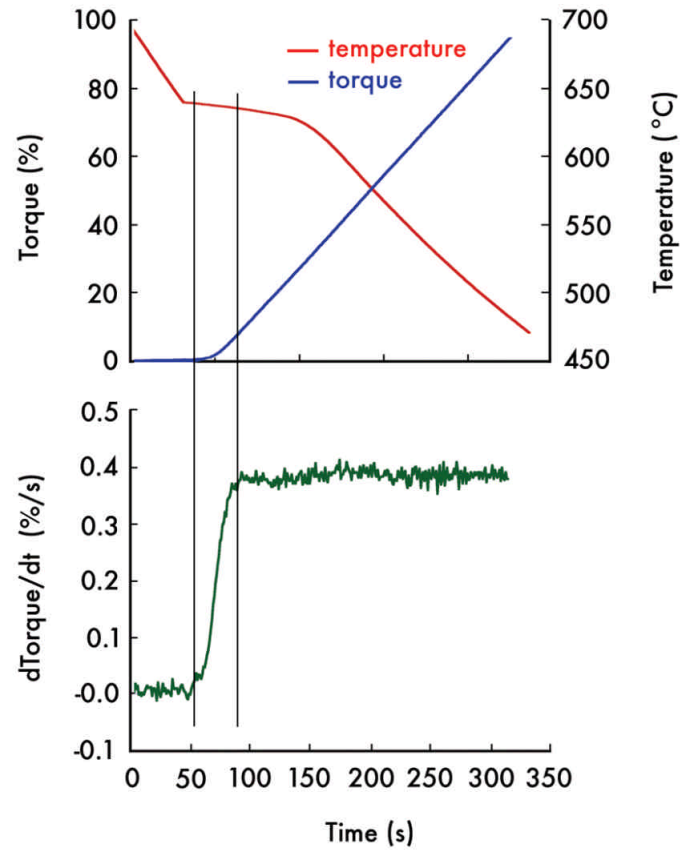


Figure 68 - Torque & dTor/dt vs. Time Data for AM20.

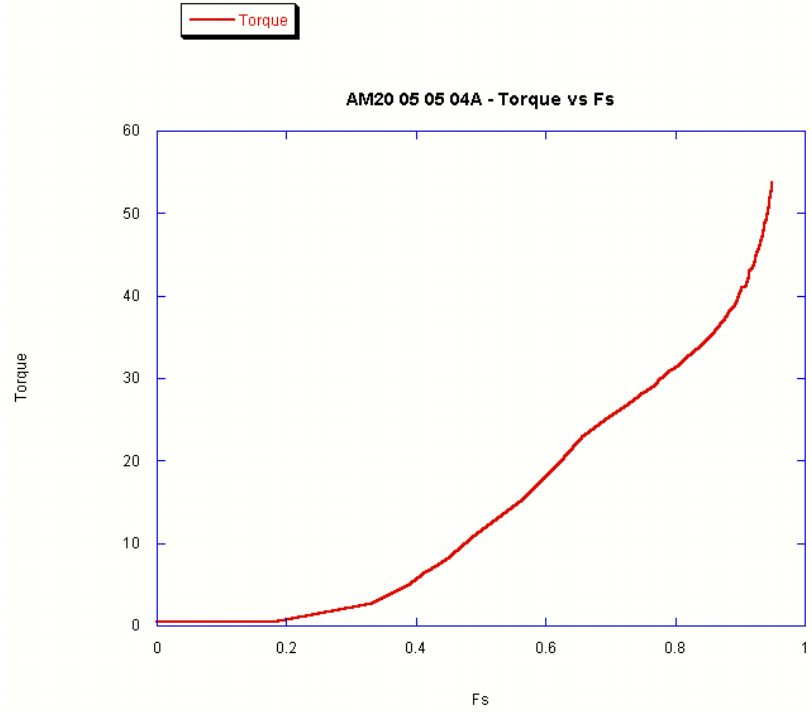


Figure 69 - Torque vs. Fraction Solid Curve for AM20.

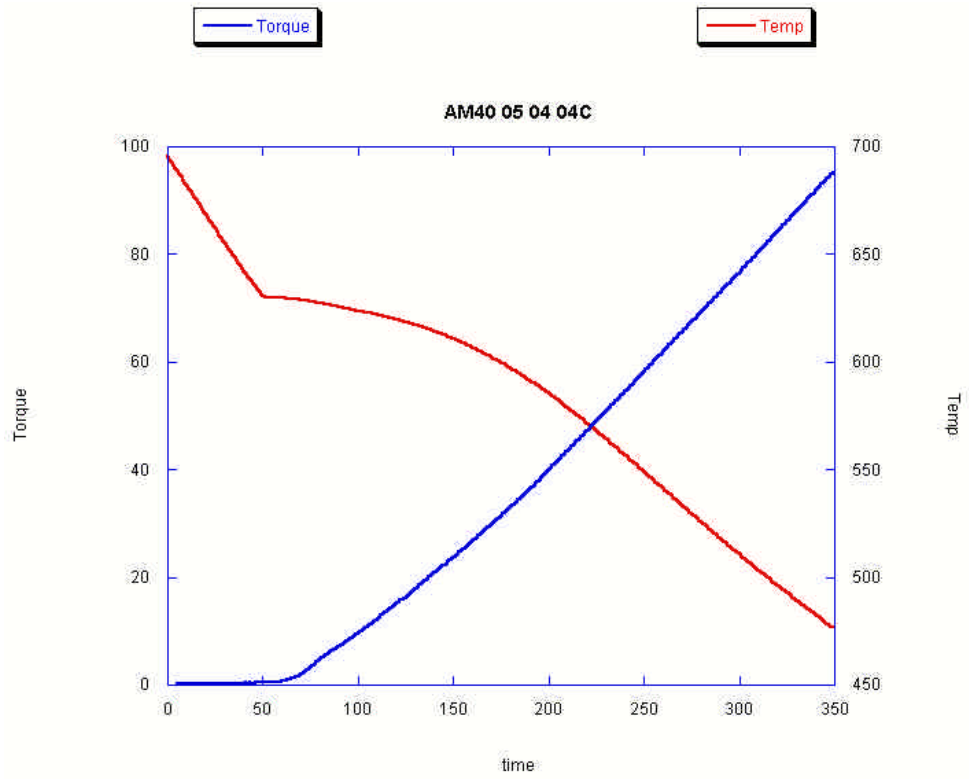


Figure 70 - Torque vs. Time Data for AM40.

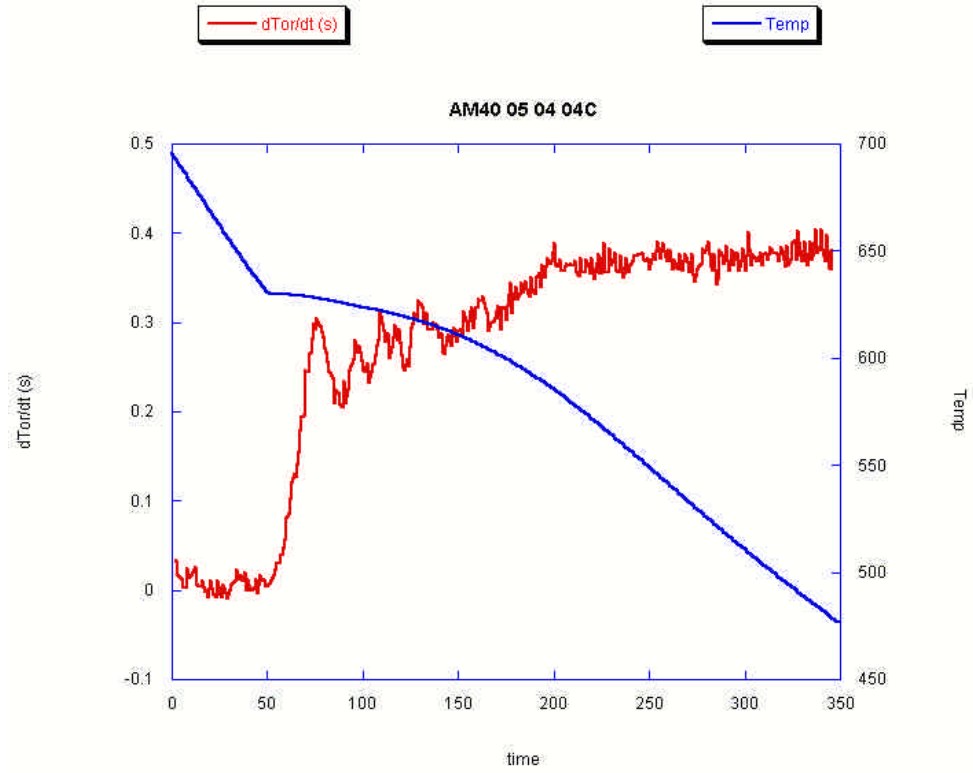


Figure 71 - Derivative of Torque vs. Time Data for AM40.

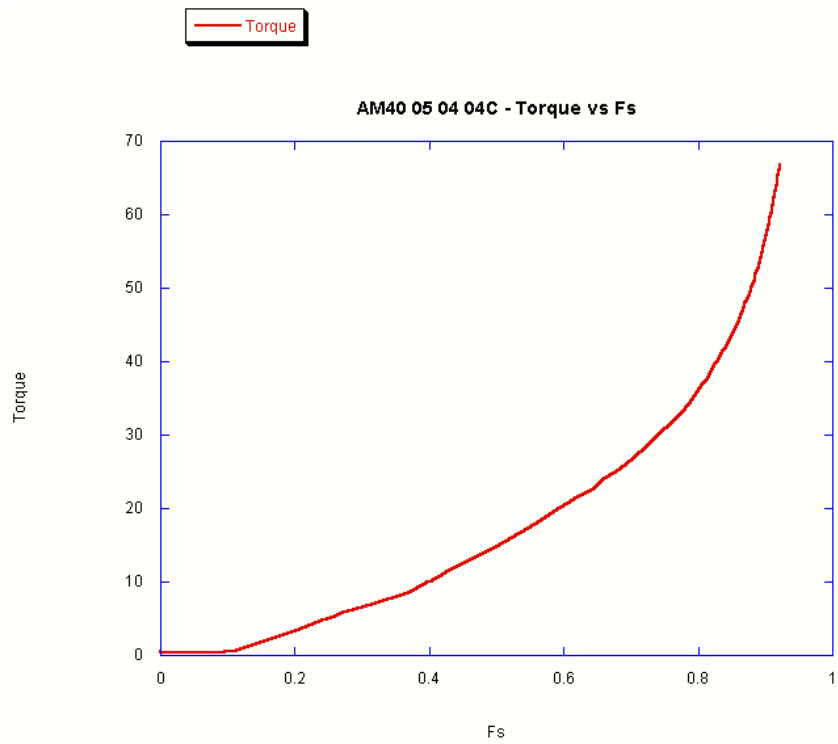


Figure 72 - Torque vs. Fraction Solid Data for AM40.

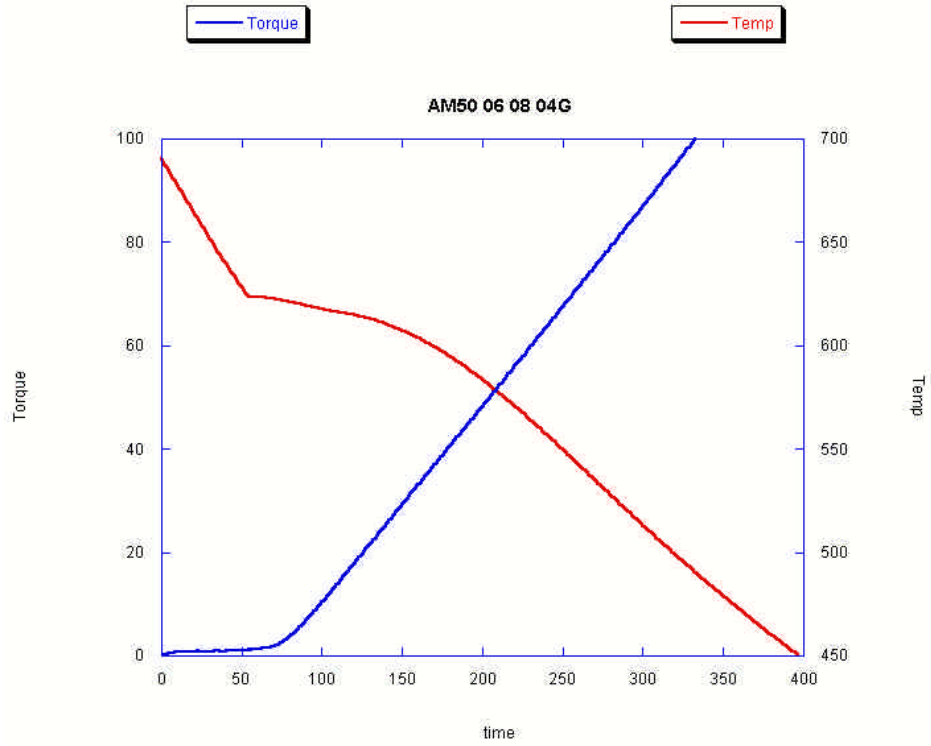


Figure 73 - Torque vs. Time Data for AM50.

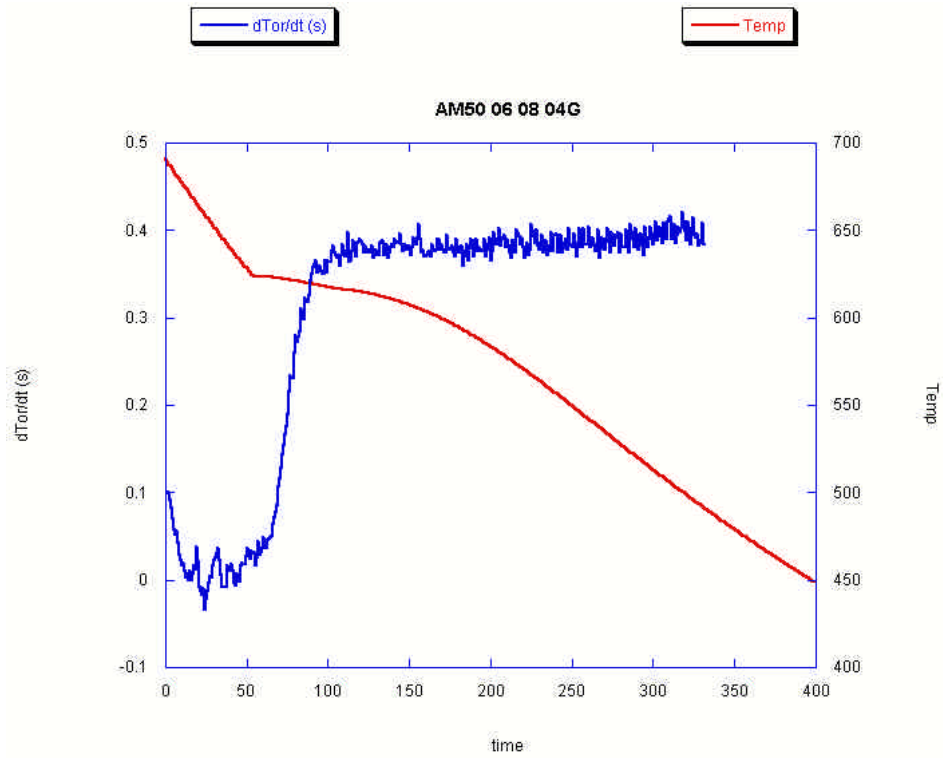


Figure 74 - Derivative of Torque vs. Time Data for AM50.

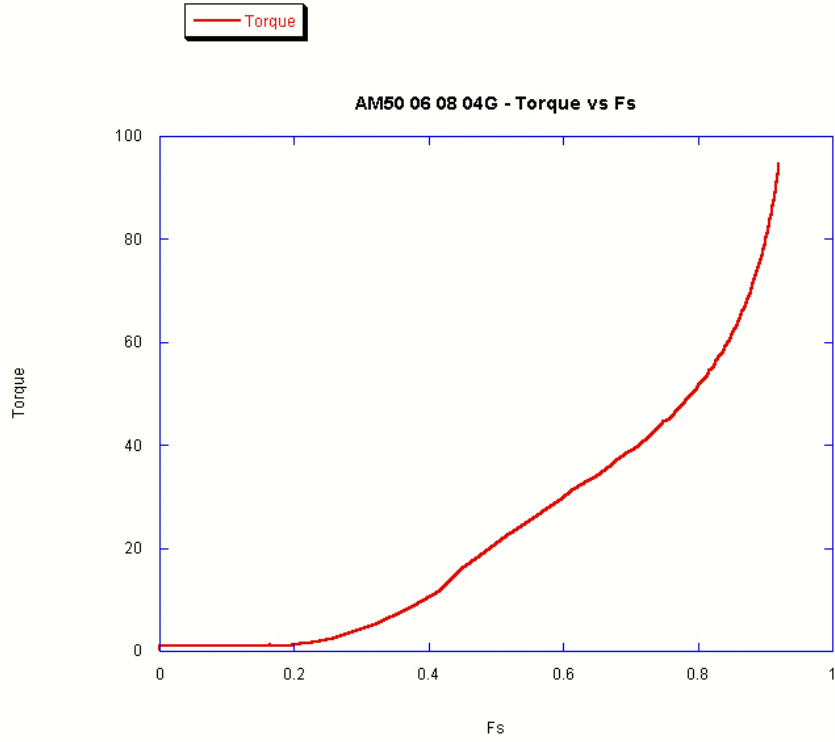


Figure 75 - Torque vs. Fraction Solid Data for AM50.

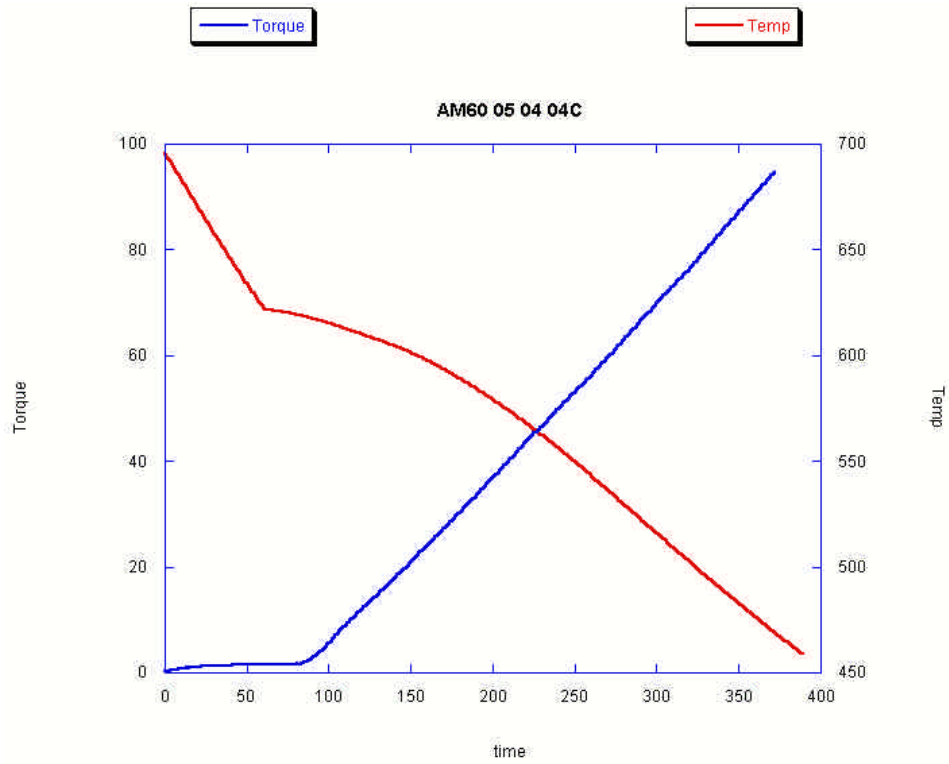


Figure 76 - Torque vs. Time Data for AM60.

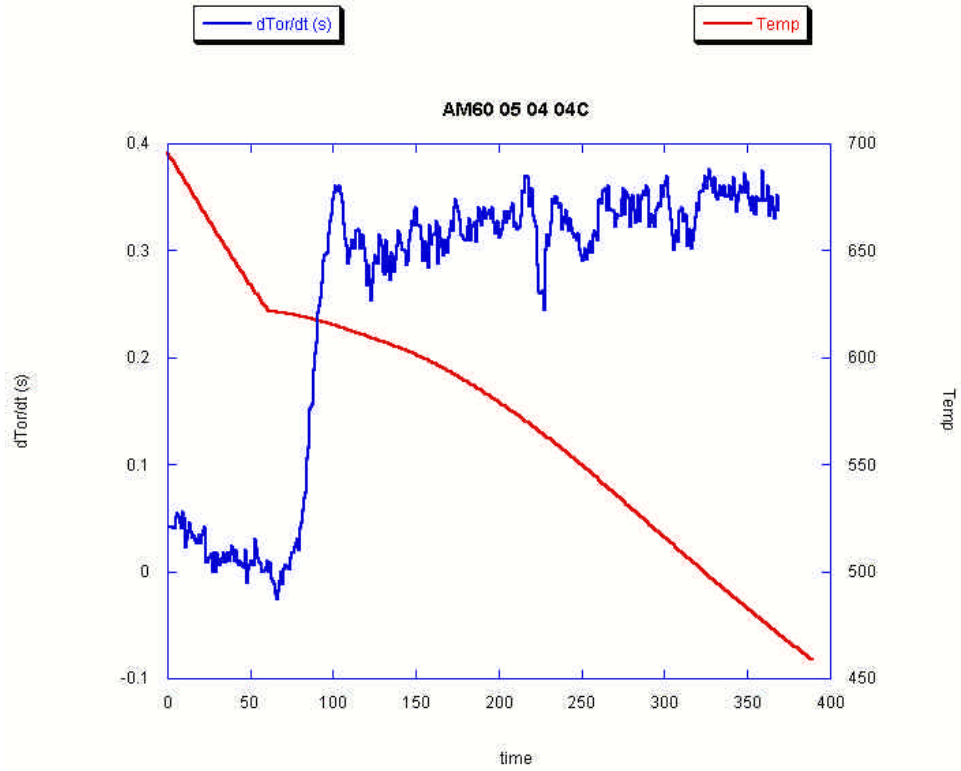


Figure 77 - Derivative of Torque Data for AM60.

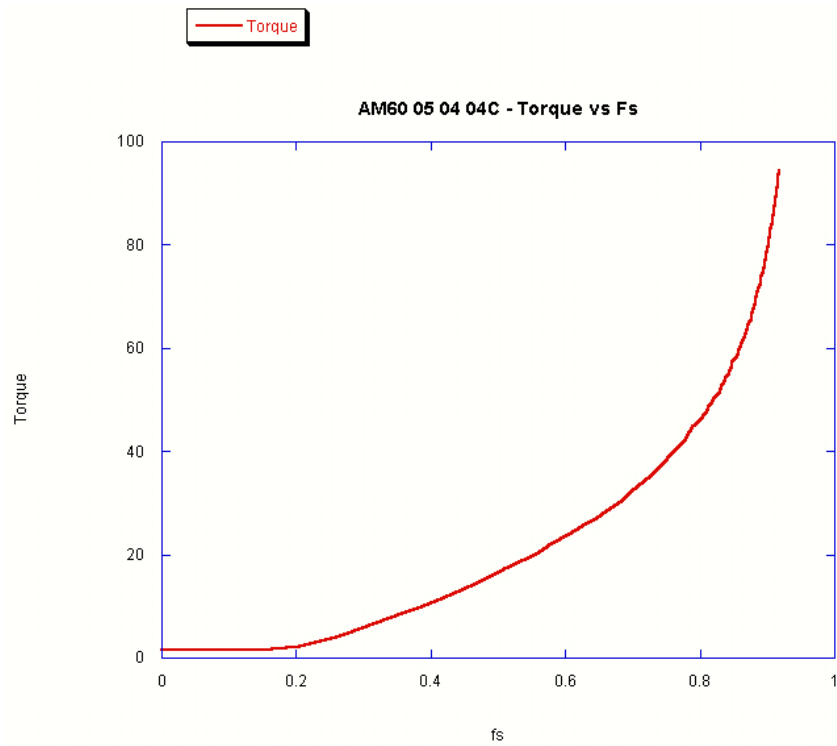


Figure 78 - Torque vs. Fraction Solid Data for AM60.

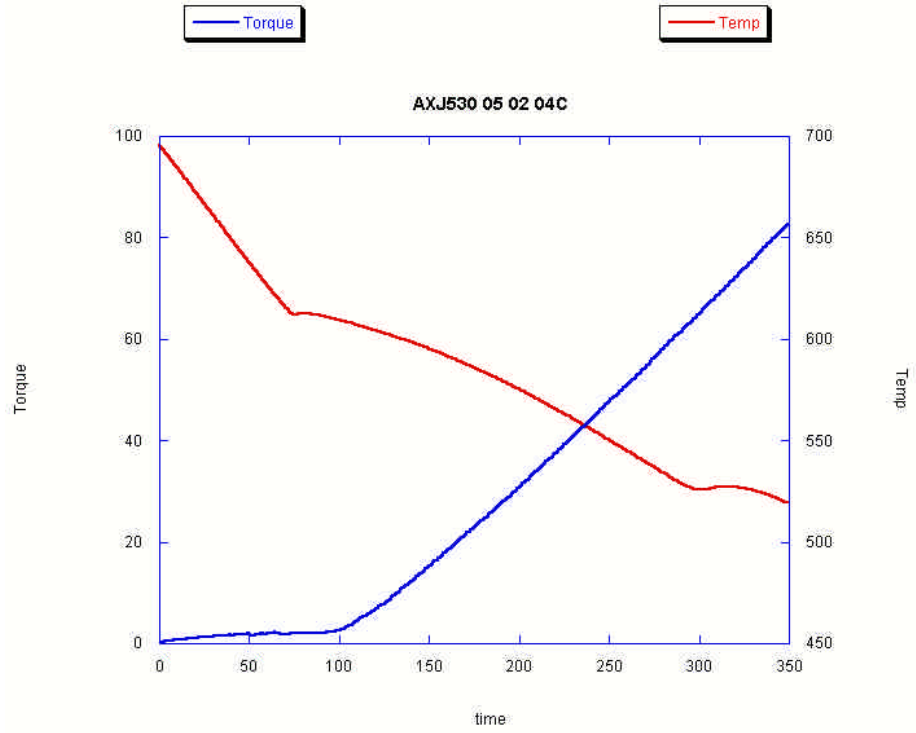


Figure 79 - Torque vs. Time Data for AXJ530.

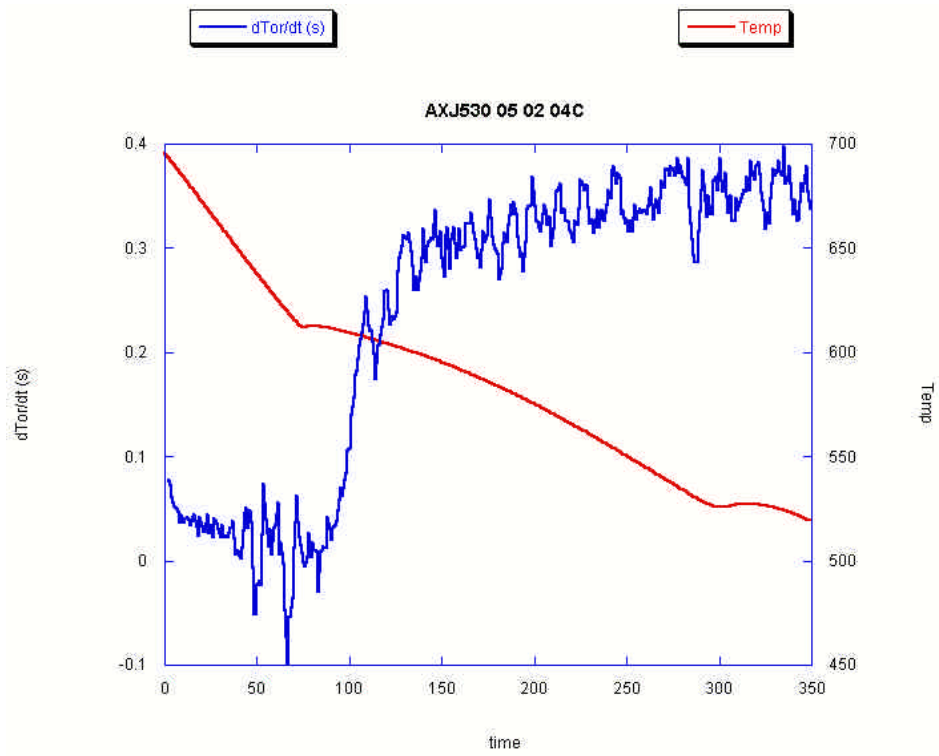


Figure 80 - Derivative of Torque vs. Time Data for AXJ530.

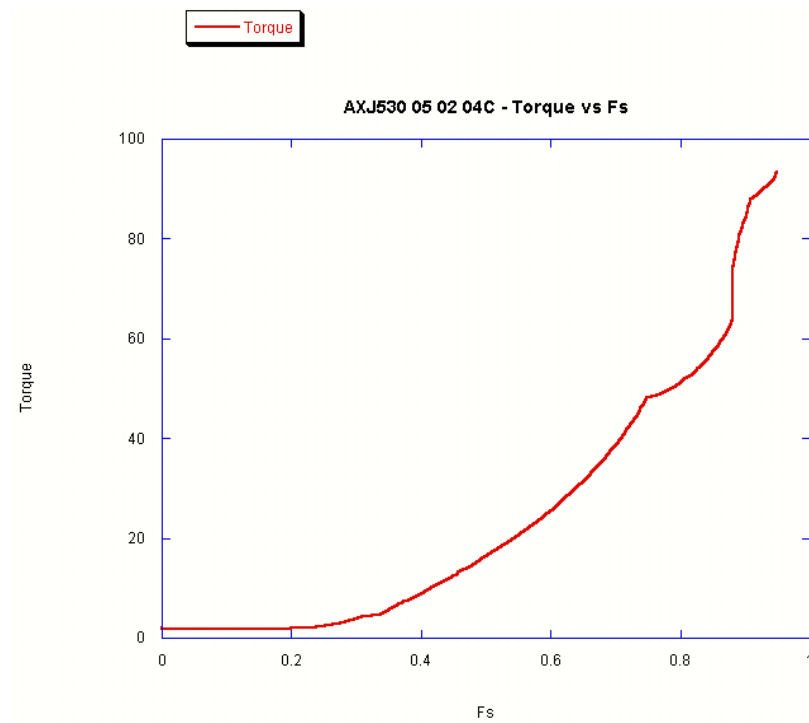


Figure 81 - Torque vs. Fraction Solid Data for AXJ530.

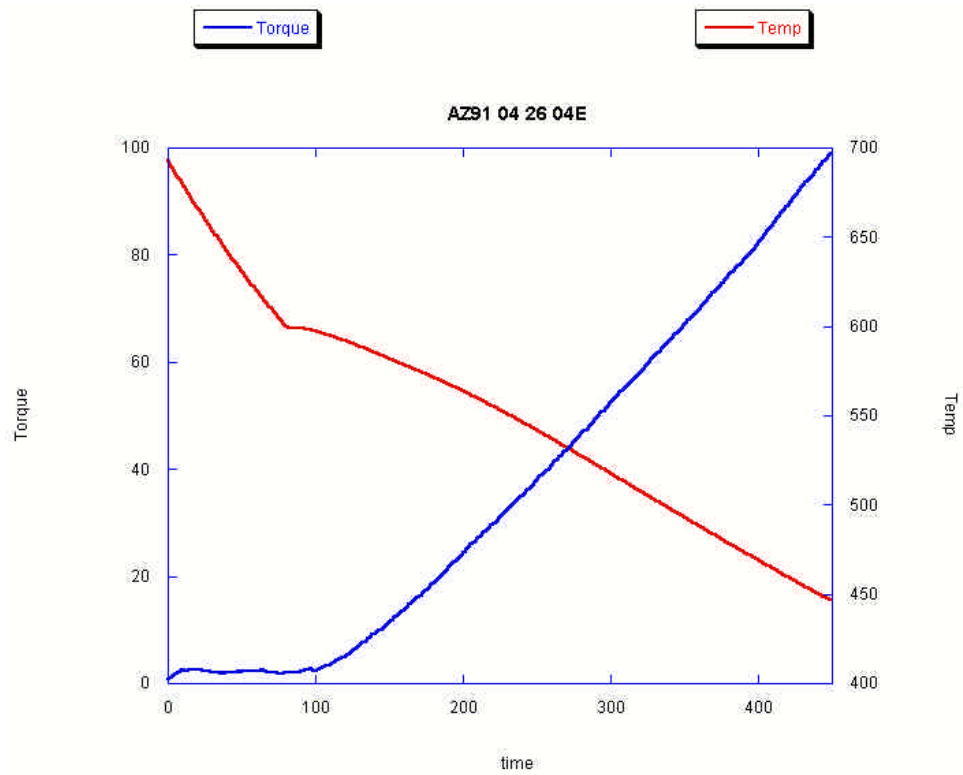


Figure 82 - Torque vs. Time Data for AZ91E.

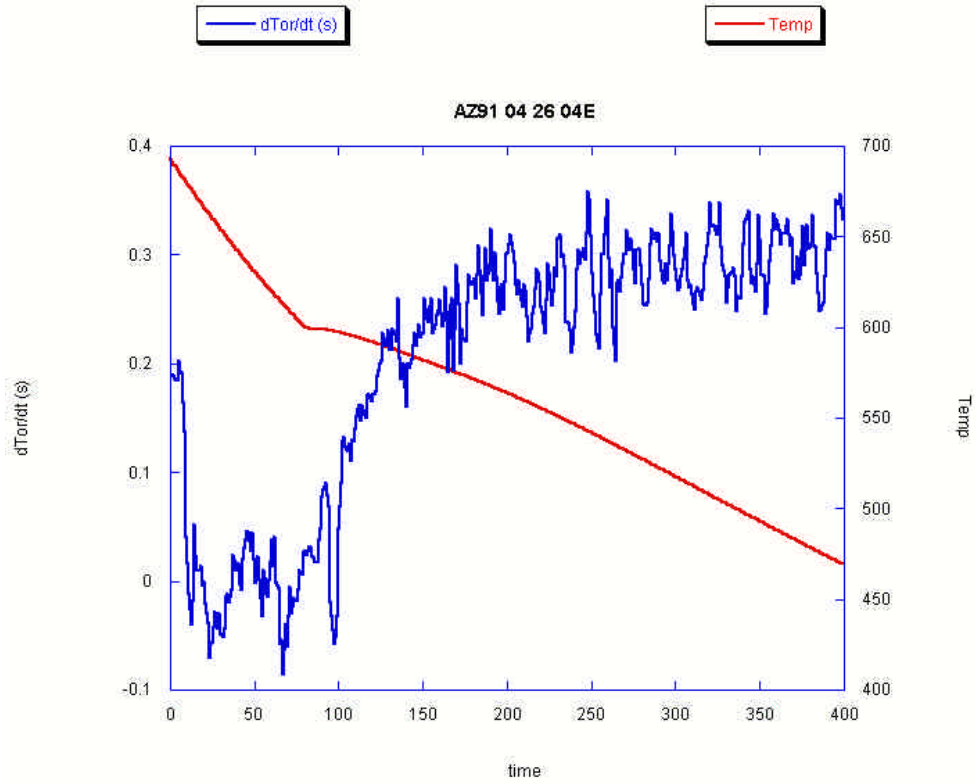


Figure 83 - Derivative of Torque vs. Time Data for AZ91E.

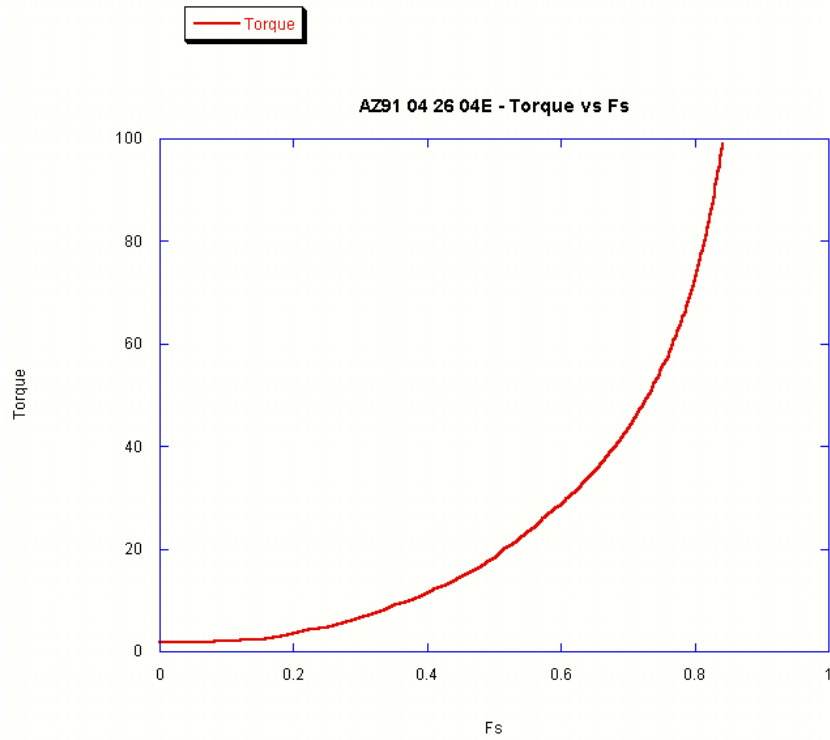


Figure 84 - Torque vs. Fraction Solid Data for AZ91E.

The coherency data does not appear to show any distinct trends with increasing aluminum content for these alloys. From our previous discussion, primary phase morphology is the primary factor in the coherency measurement. Since the primary phase morphology of most of these alloys is relatively constant, the coherency data should be relatively constant. The only alloy which significantly differs from the others is AXJ530; this alloy has been shown to have substantial differences in composition but only slight differences in microstructure.

5.4.1 Dendrite Coherency Discussion

As discussed earlier, the rigidity point has been found to be highly dependant on experimental procedure and conditions. The geometry of the vane used in this research differs dramatically from previous method, but was designed using rheological concepts, in order to reduce the possibility of measuring non-relevant metallurgical or instrumental phenomenon. One advantage of the vane method used in this research over the previous blade technique is the interaction of the vane or blade with the free surface of the melt. It is well known that a mass of melt solidifying in a crucible will form a solid oxide surface layer early in the solidification process, if not immediately. This oxide layer will present resistance to the rotating shaft of the apparatus. The torque-measuring device is connected to this rotating shaft. Therefore, the oxide layer presents a measurable torque that is incorporated into the dendrite coherency data. The current apparatus uses a fully submerged vane geometry over the previous partially submerged blade geometry. Furthermore, the cylindrical shaft connected to the submerged vane rotates in a well-defined hole through the surface oxide, not continually against it, as partially submerged

blade in the tests of Arnberg and Chai [24,25]. An additional comparison of the two experimental methods was performed using Al alloy A356.2, and the coherency data correlated very well, but no rigidity point was found. It is thought that the difference in geometry between the two testing methods is a source of experimental discrepancy.

The nature of Mg alloy solidification may also be the cause of the difference coherency behavior found. Under these casting conditions Al alloys are typically dendritic [23], this is not the case for Mg alloys. The Mg alloys have been shown to have a more globular or rosette like structure. In Al alloys the globular and rosette like structures were found to exhibit both a coherency point and a rigidity point just at a higher fraction solid [33]. Although the coherency behavior of dendritic Mg alloys has not been investigated, it is apparent that globular Mg alloys have a gentler or more gradual change in the torque versus time or torque versus fraction solid curves. It is possible that Mg alloys solidifying in a globular nature have rigidity point that is undetectable using the current rheological setup. The torque versus fraction solid curves shown previously shows a trend which could be the rigidity point. For instance in Figure 78, there is a gradual change in the slope of the curve between fraction solid of 70-85%. Though it appears proof of this theory may require the use of the third method of determining coherency and rigidity points, the direct shear cell method. Although these experiments were not performed in this research, it is possible that experiments using the direct shear cell method will answer many of the questions posed by this work.

6.0 Conclusions

This work involved extensive research on the solidification behavior and resultant microstructures of aluminum based magnesium alloys. Salient features of the complex problem of alloy solidification have been observed, through non-equilibrium thermal analysis and continuous torque dendrite coherency measurements. Microstructural characterization and phase analysis was used to fully describe the general microstructural trends of these alloys.

The thermal analysis equipment proved to be a rapid, sensitive, and affordable method of determining a wide range of solidification features. Time and temperature associated with the beginning and end of solidification, and the beginning of eutectic formations are clearly visible. The two thermocouple thermal analysis setup, allowed for detection of minor precipitation events. One such precipitation event occurred in both AXJ530 and AZ91E, and after the subsequent microscopy, the event is known to be the precipitation of the Al-Mn phase. Not every precipitation event that occurred was seen with this method, no precipitation events were found in the AM-type alloys although they are known to form similar Al-Mn phases.

The two thermocouple technique also held promise of a simple method of determining the coherency point of the material, although, the results of the experimentation for the coherency points suggested by the thermal analysis technique and the continuous torque measurement technique differ greatly. The continuous torque measurement system was developed under the same principles of previous work, but included some improvements based on rheological fundamentals. The blade spindle

previously used was replaced with a vane spindle. The vane spindle is used to simulate the concentric cylinder experiment, which is a standard rheological test. The vane was also designed to eliminate the effects of the crucible walls. Even though great lengths were taken in designing a theoretically more accurate experiment, the results were not perfect. While the results for the coherency point were precise and repeatable, a rigidity point was not readily apparent. Neither the torque versus time nor the torque versus fraction solid curves showed a definitive rigidity point, although the torque versus fraction solid curves appeared to show a trend similar to the rigidity point. The coherency behavior was also slightly different than previous work with Al alloys. The torque versus time curves showed two straight lines connected via a transition directly after the coherency point. This behavior was analyzed further through the use of the derivative of torque with respect to time. This short range of transition was reported in this work as the coherency range. While the lesser value of this range is the coherency point defined as the initial development of strength. This work questions the current understanding of coherency; our research shows a critical range of transient behavior that is currently not well understood.

This work on coherency measurements has posed a lot of questions. The answers to those questions could be evaluated by measuring the coherency and rigidity points with another rheometer or by the direct shear cell technique. It is possible that the commercially available rheometer used in this experiment had insufficient resolution to accurately measure the appearance of the rigidity point. It is also possible that the nature of Mg alloy solidification under these casting conditions, leads to development of coherency over a critical range, and that the rigidity point is developed over a larger range than it

was not apparent using these experimental methods. It is however, apparent that more research is needed for complete understanding of coherency behavior.

The microstructural analysis results are very similar to the results predicted by solidification simulations. All six alloys formed the same basic phases, with slightly different compositions. Phases found in each alloy were primary Mg in cellular morphology, Al-Mn containing phases of several geometries, and the β -Mg₁₇Al₁₂. The eutectic formations of each alloy were found to be discontinuously precipitated or fully divorced eutectics. Although the exact compositions of the phases were not determined during this work, a greater understand of the nature of Mg alloy microstructures has been determined. One example is Mn containing phases act as scavengers for impurities such as Fe and Ni.

This work has accomplished the objectives set forth by the research team and the focus group of the ACRC. Understanding of Mg alloy solidification is an on going progress, and these results should prove to be a vital stepping stone for further research in Mg alloy development or optimizing the casting procedure for Mg-Al alloys.

7.0 References

- [1] Alan A. Luo. "Materials Comparison and Potential Applications of Magnesium in Automobiles." *Magnesium Technology 2000*, TMS, pp. 89-98.
- [2] Y.W. Riddle and M.M. Makhlof, "Characterizing Solidification by Non-Equilibrium Thermal Analysis", *Magnesium Technology 2003*, TMS, pp. 101-106.
- [3] M.M. Avedesian, H. Baker, Eds., Magnesium & Magnesium Alloys, ASM International, 1999.
- [4] I. J. Polmear, "Magnesium Alloys and Applications", *Materials Science and Technology*, Jan 1994, vol. 10, pp. 1-16.
- [5] United States Council for Automotive Research. "USCAR Consortium Begins Work on Magnesium Project Structural Cast Magnesium Research Could Lead to Reduced CO2 Emissions", May 2001.
- [6] Norman Woldman, "Magnesium Casting." Magnesium, ASM International, 1946.
- [7] D.H. StJohn, A.K. Dahle, T. Abbott, M.D. Nave, and Ma Qian, "Solidification of Cast Magnesium Alloys", *Magnesium Technology 2003*, TMS, pp. 95-100.
- [8] C. Sheldon Roberts, Magnesium and its Alloys. New York: John Wiley & Sons, 1960.
- [9] A.K. Dahle, Y.C. Lee, M.D. Nave, P.L. Schaffer, and D.H. StJohn, "Development of the As-Cast Microstructure in Magnesium-Aluminum Alloys", *Journal of Light Metals*, 2001, pp. 61-72.
- [10] ASM Handbook Committee, Alloy Phase Diagrams, ASM International, 1992.
- [11] G.V. Raynor. The Physical Metallurgy of Magnesium and its Alloys. New York: Pergamon Press, 1959.
- [12] Y.C. Lee, A.K. Dahle, and D.H. StJohn, "Grain Refinement of Magnesium", *Magnesium Technology 2000*, TMS, pp. 211-218.
- [13] Y.C. Lee, A.K. Dahle, and D.H. StJohn, "The Role of Solute in Grain Refinement of Magnesium", *Metallurgical Transactions*, 31A, 2000, pp. 2895-2906.
- [14] M.D. Nave, A.K. Dahle, and D.H. StJohn, "Eutectic Growth Morphologies in Magnesium-Aluminum Alloys", *Magnesium Technology 2000*, TMS, pp 233-242.
- [15] M.D. Nave, A.K. Dahle, and D.H. StJohn, "The Role of Zinc in the Eutectic Solidification of Magnesium-Aluminum-Zinc Alloys", *Magnesium Technology 2000*, TMS, pp. 243-250.
- [16] Robert F. Speyer, Thermal Analysis of Materials, New York: Marcel Dekker, Inc. 1994.
- [17] Bernhard Wunderlich, Thermal Analysis, New York: Academic Press, Inc. 1990.
- [18] Jarmo Tamminen, "Thermal Analysis for Investigation of Solidification Mechanisms in Metals and Alloys", Ph.D. Thesis, U. of Stockholm, Sweden, 1988.
- [19] H. Morrogh and W.J. Williams, "Undercooled graphite in cast irons and related alloys", *Journal of Iron and Steel Institute*, 1954, pp. 375-378.

-
- [20] A. Hultgran, Y. Lindblom, and E. Rudberg, "Eutectic Solidification in grey, white, and mottled hypoeutectic cast irons", *Journal of Iron and Steel Institute*, 1954, pp. 365-374.
- [21] L. Bäckerud and B. Chalmers, "Some Aspects of Dendritic Growth in Binary Alloys: Study of the Aluminum-Copper System", *Transactions of the Metallurgical Society of AIME*, Vol. 245, 1969, pp. 309-318.
- [22] L. Bäckerud, E. Król, and Jarmo Tamminen, Solidification Characteristics of Aluminum Alloys: Volume 1 Wrought Alloys, Sweden: SkanAluminum, 1986.
- [23] L. Bäckerud, G. Chai, and Jarmo Tamminen, Solidification Characteristics of Aluminum Alloys: Volume 2 Foundry Alloys, Sweden: AFS/SkanAluminum, 1990.
- [24] L. Arnberg, L. Bäckerud, and G. Chai, Solidification Characteristics of Aluminum Alloys: Volume 3 Dendrite Coherency, Illinois: AFS, 1996.
- [25] Guocai Chai, "Dendrite Coherency During Equiaxed Solidification in Aluminum Alloys", Ph.D Thesis, U. of Stockholm, Sweden, 1994.
- [26] M.C. Flemings, "Behavior of Metal Alloys in the Semi-Solid State", *Metallurgical Transactions*, Vol. 22A, 1991, pp. 957-981.
- [27] J. Verö, *Mitt. Berg- u. Huttenmänn. Abt. Kgl. Ung. Palatin-Joseph-Univ. techn. u. Wirtschaftwiss. Fak Berg-, Hutten- u. Forstwissn Sorpron*, 1935, translation: *Metal Ind.*, London, 1936, pp 431-491.
- [28] A.R.E. Singer and S.A. Cottrell, *Journal of Industrial Metals*, Vol. 73, 1947, pp. 33-54.
- [29] S.A. Metz and M.C. Flemings, *Transactions of the American Foundrymen's Society*, Vol. 77, 1969, pp. 329-334.
- [30] S.A. Metz and M.C. Flemings, *Transactions of the American Foundrymen's Society*, Vol. 78, 1970, pp. 453-460.
- [31] D.A. Spencer, R. Mehrabian, and M.C. Flemings, "Rheological Behavior of Sn-15 Pct Pb in the Crystallization Range", *Metallurgical Transactions*, Vol. 3, 1972, pp. 1925-1932.
- [32] R.J. Claxton, *Journal of Metals*, Feb, 1975, pp. 14-16.
- [33] N.L.M. Veldman, A.K. Dahle, D.H. StJohn, and L. Arnberg, "Dendrite Coherency of Al-Si-Cu Alloys", *Metallurgical and Materials Transactions*, Vol. 32A, 2001, pp. 147-155.
- [34] S.M. Nabulsi, "The Behavior of Semi Solid Aluminum-Silicon Alloys in a Direct Shear Cell", Ph.D. Thesis, U. of Queensland, Australia, 1998.
- [35] A.K. Dahle and D.H. StJohn, "Rheological Behavior of the Mushy Zone and Its Effects on the Formation of Casting Defects During Solidification", *Acta Metallurgica*, Vol. 47, 1999, pp. 31-41.
- [36] T. Sumitomo, D.H. StJohn, and T. Steinberg, "The Shear Behavior of Partially Solidified Al-Si-Cu Alloys", *Materials Science and Engineering*, 2000, pp. 18-29.
- [37] A.K. Dahle, S. Instone, and T. Sumitomo, "Relationship between Tensile and Shear Strengths of the Mushy Zone in Solidifying Aluminum Alloys", *Metallurgical Transactions*, Vol. 34A, 2003, pp. 105-113.

[38] Y.W. Riddle, L.P. Barber, and M.M. Makhlof, "Characterization of Mg Alloy Solidification and As-Cast Microstructures", Magnesium Technology 2004, TMS, pp. 203-208.

[39] George Vander Voort, "Metallography of Magnesium and its Alloys", Buehler, Inc. Tech Notes, Volume 4, Issue 2.

[40] N. Tonmukayakul, Personal Interaction, 2003.